Ph.D. Dissertation

Design of Low Power Analog Front-End of Touch-Screen Controller With Adiabatic Signal Generation and Optimized Sensor Modes

단열구동과 센서회로 최적화를 통한 저전력

터치스크린 컨트롤러 아날로그 전단회로 설계

by

Jiheon Park

August, 2019

School of Electrical Engineering and Computer Science
College of Engineering
Seoul National University

Design of Low Power Analog Front-End of Touch-Screen Controller With Adiabatic Signal Generation and Optimized Sensor Modes

by

Jiheon Park

A Dissertation Submitted to the Department of
Electrical Engineering and Computer Science
in Partial Fulfillment of the Requirements for the Degree of
Doctor of Philosophy
at
SEOUL NATIONAL UNIVERSITY
May, 2019

Committee in Charge:

Professor Hyuk-Jae Lee, Chairman

Professor Deog-Kyoon Jeong, Vice-Chairman

Professor Jaeha Kim, Member

Professor Minjae Lee, Member

Professor Dongsuk Jeon, Member

Abstract

In this thesis, a touch sensing analog front-end (AFE) for capacitive touch-screen panel (TSP) is presented. Reduced distance between the touch-screen and display causes large capacitive coupling, resulting in increased parasitic capacitance and reduced touch sensitivity. Display noise interference is worse due to the large coupling capacitance. Therefore, it is a challenge to design an AFE capable of accurate and energy-efficient sensing of a touch input in the integrated TSP. To provide power efficient stimulation on the TSP, an adiabatic signal generation based on charge recycling is newly proposed as an AC-signal generator. Furthermore, in order to cancel out the display noise interference through the large parasitic capacitance, a fully differential touch sensing module is incorporated in the AFE. A correlated noise sampling is employed in the decoder stage for the multi-driving demodulation process. To further improve power efficiency, the sensing module is multiplexed in 4 ways while achieving an optimal conversion time per sample. The proposed AFE was implemented in a 180-nm CMOS process. The fabricated AFE shows 57.0-dB SNR at 120 fps while consuming 17.8 mW. Compared with power consumption of 19.9 mW expected with a conventional signal generation, the proposed adiabatic signal generator dissipates only 7.1 mW, exhibiting a power reduction of 64 % owing to the adiabatic driving method.

In addition, the self-capacitance sensing mode is also implemented as low power, coarse touch detection mode. The newly proposed current mirroring voltage-level regulation (CM-VLR) circuit senses the transition of self-capacitance of the TSP and

detects motions of the touch-object. While keeping a voltage level, a certain amount of electric charge is additionally required when a capacitance is newly added at the sensing channel, and the amount of charge is used for the detection. Only one CM-VLR cell is used to scan the entire TSP, and the touch-screen channels are multiplexed and selected in order, and the AFE does not require the offset-calibration step from the additional coverage capacitance attached to either channel. The AFE was fabricated in a 180-nm CMOS process, and the CM-VLR cell occupies 0.12 mm^2. In 120-Hz report rate, the AFE detects touch-object in 32-dB SNR while dissipating 2.1-mW of power.

Keywords: Adiabatic driving, analog front-end (AFE), capacitive sensor, charge recycling, mutual-capacitance, self-capacitance, touch-screen controller (TSC).

Student Number : 2013-20975

Contents

List of Figures

List of Tables

Chapter 1

Introduction

1.1 Motivation

Touch-screen is widely adopted for the recent mobile devices as their primary input device. Touch sensing interface offers easy and intuitive interact. A touch sensor detects a touch input by measuring electrical characteristic parameter of the touch-screen panel (TSP) located on top of the display, with no extra device required for touch detection. Various mobile phones with the touch-screen are developed in the past decade, and much improved form-factor with minimum amount of physical button and wide display for mobile device is achieved.

Recently, the display panel gets thinner to reduce overall thickness of device and to secure enough battery space inside of the device [1.1][1.2]. As a way of reducing thickness of the display, thinner organic light-emitting diode (OLED) cell encapsulation layer is developed, and several layers such as air gap and adhesive layers are removed among the stack-up structure of display. The TSP layer which was mounted on top of the display becomes integrated and located inside the display panel. The electrodes of touch-screen are located right on the encapsulation layers

for the display cells.

Due to the increased capacitive coupling at the touch-screen, the interference from the display became more severe than that of the add-on type TSP which is mounted on top of the display. As a result, the touch-screen channels suffer from significant capacitive coupling from the display panel due to the thin stack-up structure despite the touch-integrated display module enables the ultra-thin form factor in the mobile devices. While the touch-input is detected by sensing capacitance parameters of TSP, the OLED driving signals interfere the touch sensing signal through the large coupling capacitance. The touch sensing signal and the display interference are hard to separate because the signal transmissions occur based on the same principle. Therefore, it is hard to achieve noise-insensitivity of touch sensing AFE, and the signal-to-noise ratio (SNR) can be degraded.

Moreover, a protecting layer, which is required for improved durability in the user side of the panel, separates the touch-screen and the touch objects relatively farther, causing reduced touch sensitivity. To overcome the reduced touch sensitivity, the increased mutual-capacitance stimuli is often adopted. However, due to the increased capacitive coupling between the TSP and display layers, generation of the increased stimuli power would impose huge power dissipation which is not appropriate for the battery-powered application.

In this thesis, the emerging problems associated with touch-screen integrated display panel are addressed. For mutual-capacitance readout, an adiabatic generation of stimuli is proposed to reduce power dissipation on generating the capacitance stimulation signal and to achieve improved energy-efficiency on touch detection espe-

cially in the presence of large coupling capacitance. An analysis of the switched-capacitor based signal generating method is described. Techniques to reduce peripheral components are suggested to enhance usability in small form-factor applications. Moreover, cascaded fully-differential noise filter stages are adopted which reduces the interference from various sources for noise-insensitivity. With the optimization on circuit configuration, the enhancement on the energy-efficiency of mutual-capacitance sensing is achieved.

Moreover, by detecting the existence of touch-input, further energy reduction can be achieved, and the proposed design can also be configured to the coarse detection mode by sensing the self-capacitance of the TSP. As an assistant operation mode of the touch sensing, a self-capacitance readout method is newly proposed for low power touch detection.

1.2 Thesis Organization

This thesis is organized as follows. In Chapter 2, the overview of the touch-screen sensor system is presented. Basic structure and operation principle of a touch sensor are described, and an electrical model of the noise interference and the TSP is expressed. Sensing schemes and readout methods for touch sensing AFE are compared, and the motivation on the proposed AFE is described.

In Chapter 3, the low-power mutual-capacitance readout sensor is presented. To reduce power dissipation on generating the mutual-capacitance stimulation signal,

an adiabatic signal generation method is proposed. Energy reduction and the generated signal amplitude are analyzed considering the R-C parasitic components of the TSP. Then, system architecture and implementation details of the stimuli generator and the signal sensing module are shown. Design considerations to achieve high energy efficiency in touch signal detection are described. Measurement result cover overall performance of the readout method verifying the analysis on the proposed signal generation method.

In Chapter 4, the low-power self-capacitance readout sensor is presented for an assistant operating mode for overall energy efficiency. A low power self-capacitance readout method is newly proposed, and its calibration-free operation is described. Measurement results with the overall operation and coarse detection of touch-input are exhibited. The touch sensing analog front-end is summarized with conclusion of this thesis.

Chapter 2

Touch Sensor System Overview

2.1 Touch-Screen Panel

Instead of resistive touch sensors, capacitive touch sensors are mostly used today because of the multi-touch detecting capability. Enhanced durability is also achieved with capacitive touch sensors since the capacitive sensors are located beneath the protecting glass while the resistive touch sensors are directly pushed by users and can be damaged. Fig. 2.1 illustrates basic operation principle of capacitive touch sensors. As a touch-object such as a finger approaches to the surface of the touch surface, the electrical field formed at the touch sensor is altered. Therefore, the mutual-capacitance between TX and RX channels of touch sensor is decreased as the object blocks the capacitive coupling as shown in Fig. 2.1(a), and additional coupling from the object increase overall self-capacitance of the channel as shown in Fig. 2.1(b).

According to the disposition of touch sensing channels, capacitive TSPs are also classified as shown in Fig. 2.2. The dot-type TSP is consisted with the distributed

touch sensing channels. Using the dot-type TSP, the multi-touch detection is achieved by sensing self-capacitance at each location, but too many routing corridors are required to access the channel. On the other hand, the bar-type TSP is consisted with long touch sensing channels, and the multi-touch detection is fully achieved by sensing the mutual-capacitance between the TX and RX channels. The bar-type TSP is usually adopted for touch sensing systems display screen with narrow bezel owing to less routing path required. Area of contact between channels and electrical coupling is increased as the touch sensing channels are formed in diamond shape as illustrated in Fig. 2.2.

(a)   (b)
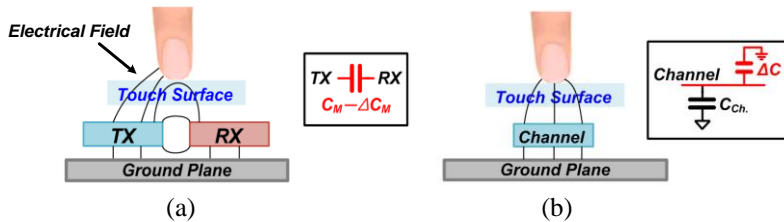
Fig. 2.1 Types of capacitive touch sensors:

(a) mutual-capacitance and (b) self-capacitance.
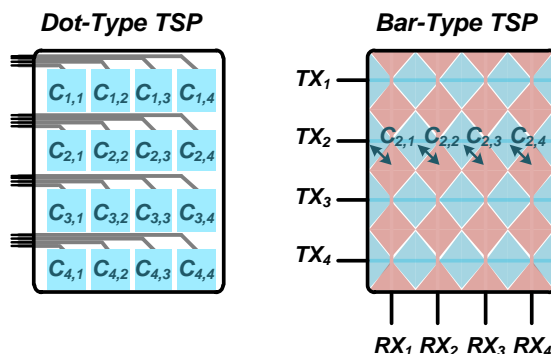
Fig. 2.2 Classification of capacitive TSPs by disposition.

2.2 Touch-Screen Controller

2.2.1 Requirements

The TSC detects presence and location of a touch-object such as fingertips and electric pens. Fig. 2.3 illustrates a typical operation of the TSC. The touch-object affects electrical characteristic of the TSP, and the AFE of the TSC detects transition of the characteristic components. The AFE converts the detected characteristic component transition to digital signal through an analog to digit converter (ADC). As a result, the AFE generates a map of the measurement results on the electrical characteristic of the TSP.
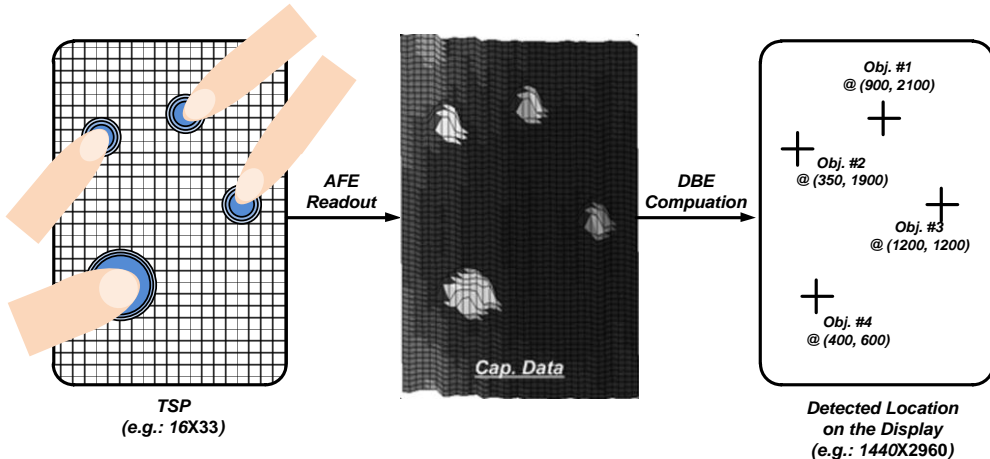
Fig. 2.3 Conceptual diagram of signal process in TSC.

Afterward, the location of the touch-object is found from the map through the back-end computations in digital domain. The representative requirements of TSC is shown in Table 2.1. Typically, the digital back-end (DBE) computation including the offset calibration is performed to extract only the signal difference due to the touch-input, and extra noise filtering in the digital domain for further reduce external interferences [2.3][2.4]. On top of that, a computation task called labelling [2.5] is performed to identify and separate touch-objects. The location of each touch-object is estimated from the separated capacitance data [2.9].

Table 2.1 TSC requirements (in Windows 10 Guidelines [2.1]).
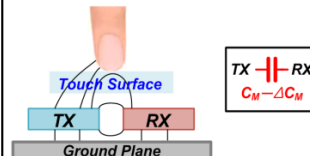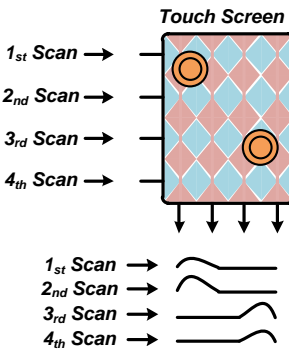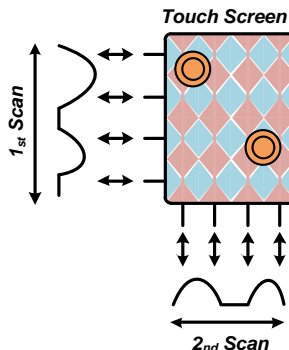
Attribute	Requirements
Accuracy	$< \pm 1$ mm ($< \pm 2$ mm @ edges)
Stationary Jitter	< 0.5 mm
Linearity (Moving Jitter)	$< \pm 1$ mm (± 2 mm @ edges)
Finger Separation	< 8 mm (edge to edge)
Simultaneous Contacts	$>= 5$
Move Latency	< 35 ms
Report Rate	$>=$ Display Refresh Rate (Typ: 60 Hz) $<= 250$ Hz
Resolution	$>=$ Native Display Resolution

2.2.2 Analog Front-End of Touch-Screen Controller

Every back-end computation described previously is based on the readout results of the AFE. Therefore, the sensing accuracy of the TSC is mainly determined by performance of the AFE. There are several types of touch sensing AFE as briefly

mentioned previously; the capacitance readout methods in general are compared in Table. 2.2 using the bar-type TSP. To sense the mutual-capacitance of the TSP, the stimulation signal is transmitted to the dedicated channel to scan the mutual-capacitance between the selected channel and RX channels. Only the TX frequency component of the received signal is recovered through the noise filter stages, and as a result, the mutual-capacitance readout method achieves better readout resolution and noise immunity [2.11]. On the other hand, the self-capacitance readout can cover a wider part of TSP at once. Therefore, the self-capacitance readout method requires fewer steps to scan the entire touch-screen.

Table 2.2 Comparison between the mutual-capacitance readout method and the self-capacitance readout.

2.2.3 Performance Metric of Analog Front-End

The TSC should detect the touch-object fast and accurately. Fig. 2.4 highlights the importance of both frequent sensing and accuracy, and the motion of the touch-object could be distorted with low frame rate detection. Fast detection of touch-object requires frequent report rate of the capacitance map from the AFE. With imprecise sensing at AFE, the motion of the touch-object could be interpreted ambiguously. Usually, the precision of the AFE is measured with the signal-to-noise ratio (SNR). Many works on the designs of AFE for TSC used the following SNR definition which is illustrated in Fig. 2.4, the definition of the SNR [2.11] can be represented as follows:

$$SNR[dB] = 20\log\left[\frac{|\bar{S}_{UT} - \bar{S}_T|}{\sigma_T}\right], (2.1)$$

(a)

(b)
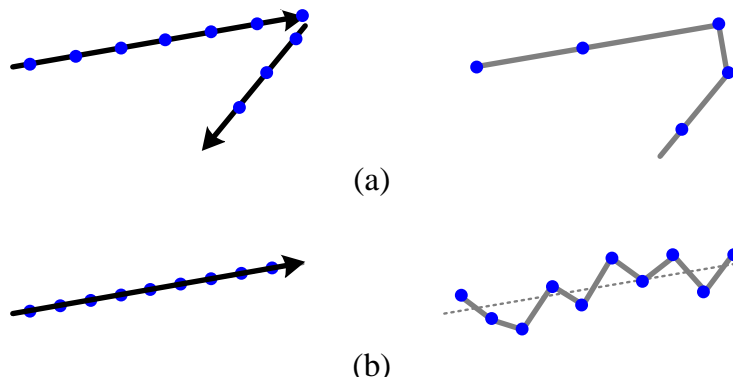
Fig. 2.4 Importance of sensing with (a) high report rate and (b) high precision.
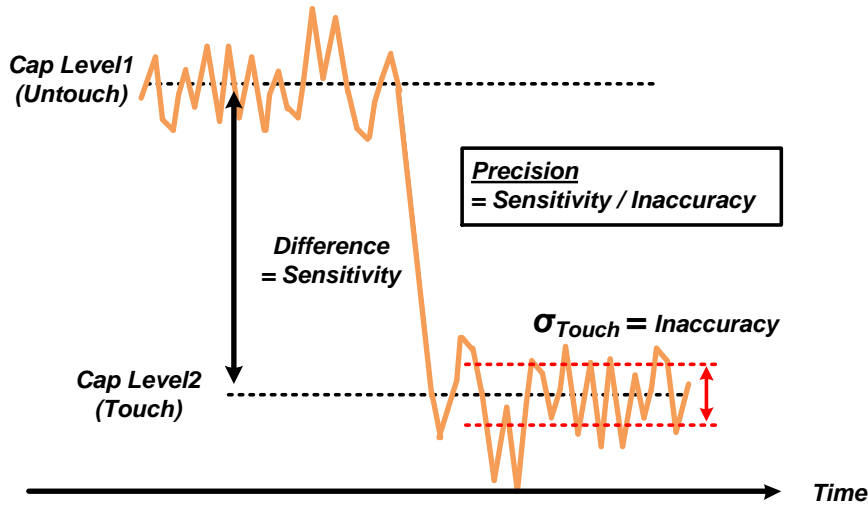
Fig. 2.5 Output of touch sensing AFE.

where $\overline{S_{UT}}$ and $\overline{S_T}$ are defined by the mean signal value without the touch-object and with the object respectively, and the inaccuracy σ_{Touch} is through the root-mean-square (RMS) value when the touch is applied. Usually, the RMS value is counted through 100 samples of TSC data [2.11][2.14], hence the mean signal values are also measured through 100 samples as (2.2) and (2.3) where di indicates each sample data.

$$\overline{S}_{UT_{or}T} = \frac{\sum\limits_{i=1}^{100} d_{i,UT_{or}T}}{100} \, , \, (2.2)$$

$$\sigma_{T,RMS} = \sqrt{\frac{\sum\limits_{i=1}^{100}(\overline{S}_T - d_{i,T})^2}{100}} \, . \, (2.3)$$

The touch sensitivity and noise interference are all included in the SNR, hence the SNR well represents the performance of the AFE in the real environments.

Low power consumption of the touch sensing AFE is also important especially since the TSC are widely adopted at the battery-powered mobile devices. In general, sensing circuits are placed for the dedicated touch-screen channels, and as the area that the AFE should cover increases, the number of channel increases and the more circuits needs to be utilized. Therefore, as the energy-efficiency figure-of-merit (FoM) of touch sensing AFE defined in [2.11] which well evaluates not only sensing efficiency but also the sensing coverage because the number of nodes is included in the FoM. The FoM is expressed as follows:

$$FoM = \frac{P_{AFE}}{SNR \cdot FR \cdot \#Nodes} . (2.4)$$

2.3 Design Issue by Tightly Coupled Display Driving

2.3.1 Touch-Screen – Integrated Display Panels

Display panels especially for mobile devices are continuously becoming thinner for better form factor and larger battery capacity. To make a thinner OLED panel, thinner display cell-encapsulation layer is developed, and the air gap at the top of the panel is removed. As a result, the TSP which had been attached on the display module becomes integrated in the panel, and these display modules are called on-cell TSP as the touch sensing channels are placed right on top of the display cell. The structure of recent ultra-thin display panels is illustrated in Fig. 2.6 and previous add-on type TSP is compared. An encapsulation layer is formed to prevent oxidation of organic cells on the display cells which are represented as RGB pixels. Although the touch-integrated display module enables an ultra-thin form factor in the mobile devices, the touch-screen channel suffers from significant capacitive coupling from the display panel due to the thin stack-up structure. Therefore, the display driving signal transmitted is tightly coupled to the touch-screen channels and interrupts the touch sensing. Moreover, a protecting layer, which is required for improved durability in the user side of the panel, separates the touch-screen and the touch objects farther, causing reduced touch sensitivity. Therefore, a precise and noise insensitive

touch sensing AFE becomes more importantly required.

The electrical model of a bar-type TSP is shown in Fig. 2.7. Because the resistance of metal-mesh touch-screen channels (R_M) is small and negligible compared to the routing path resistance (R_P), each tile of the section can be represented as shown in Fig. 2.8. The capacitances at each channel (C_C and C_S) are much enlarged as the touch-screen is integrated in the display panel, but not the sensitivity of the mutual capacitance (C_M).
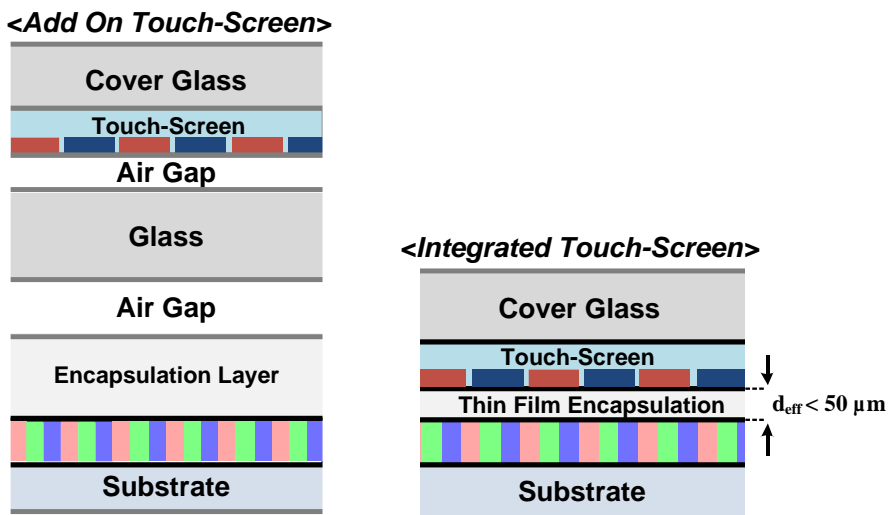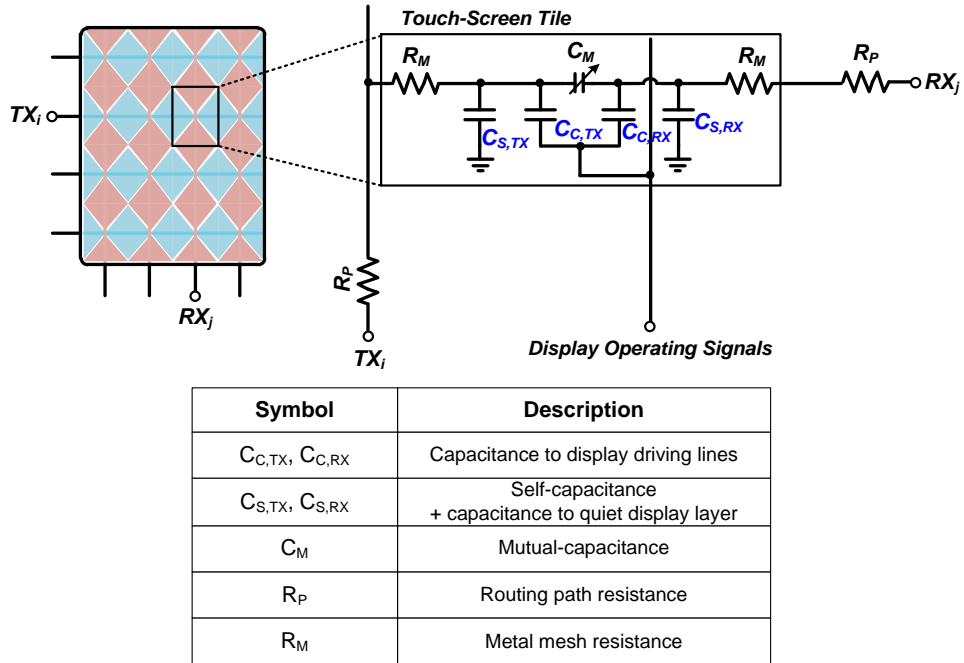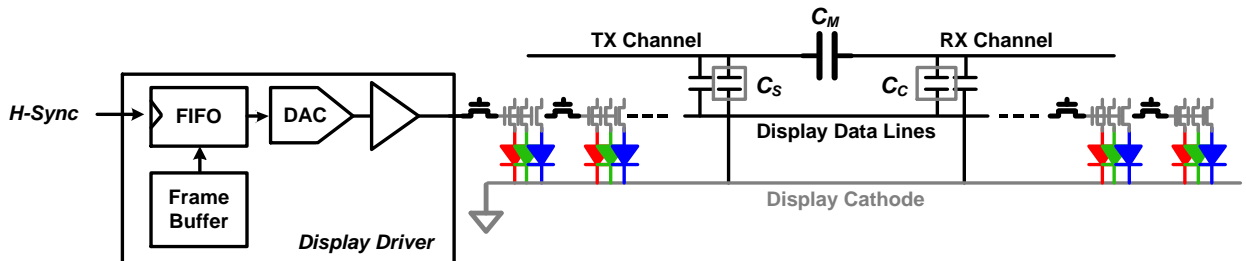
Fig. 2.6 Conceptual diagram of display panel stack structure.

Symbol	Description
$C_{C,TX}$, $C_{C,RX}$	Capacitance to display driving lines
$C_{S,TX}$, $C_{S,RX}$	Self-capacitance + capacitance to quiet display layer
C_M	Mutual-capacitance
R_P	Routing path resistance
R_M	Metal mesh resistance

Fig. 2.7 Electrical model of bar-type TSP.

Fig. 2.8 Block diagram of display driver IC and OLED panel.

2.3.2 Display Interference

Due to the increased capacitive coupling at the touch-screen, the interference from the display became more severe. As the effective distance between the touch-screen channel and the display layers (d_{eff} in Fig. 2.6) is decreased, the coupling capacitance (C_C in Fig. 2.7) display increased and became the largest capacitance component in the electrical model. The display driving operation is illustrated with the block diagram of a typical display driver IC as shown in Fig. 2.8. The display driver IC deliver the image data line-by-line, and the display driving operation heavily affects the TSP [2.12][2.13].

Based on an electrical model of the touch-screen channel is shown in Fig. 2.7, the signal transfer ratio is introduced to emphasize problems that becoming worse as display panels get thinner. The sensing channel of touch-screen is usually connected to charge amplifier (CA) circuit which structure is shown in Fig. 2.9. The display interference which passes through the C_C is much more amplified by the charge amplifier. For the touch detection, the TX signal (V_{TX}) is delivered through the mutual capacitance, and less signal power passes through the TSP due to the increased overall capacitance of touch-screen (C_L in Fig. 2.7) blocks signal transmission with the parasitic resistance (R_P in Fig. 2.7). Moreover, the display interference affects the RX channels through the significantly increased C_C. Therefore, the feedback capacitor at the CA (C_{FB} in Fig. 2.9) needs to be scaled according to Cc to prevent voltage saturation. In sum, the noise transfer function of display interference (*NTF*) and touch signal transfer function (*STF*) are expressed as follows:

$$NTF(d_{eff}) = \frac{C_{L,0} \cdot d_{eff,0}}{C_{FB} \cdot d_{eff}} \cdot \frac{1 + f/f_{CA}}{1 + f/f_{BW}} \qquad (2.5)$$

$$STF(d_{eff}) = \frac{C_M \cdot d_{eff,0}}{C_{L,0} \cdot d_{eff}} \cdot \frac{C_M}{C_{FB}} \cdot \frac{1 + f/f_{CA}}{(1 + f/f_{BW})^2} \qquad (2.6)$$

where $C_{L,0},\ C_{S,0}$ is reference load-capacitance and self-capacitance, f_{BW} is the band-width of the touch-screen, and $d_{eff,0}$ is the reference effective distance of a touch-screen. Relatively, the mutual capacitance C_M and R_P do not scale as d_{eff} varies. Based on the circuit configuration shown in Fig. 2.9, the signal transfer ratio plotted is estimated as shown in Fig. 2.10 from an electrical model of touch-screen and the CA stage which has zero at 10 kHz so that the signal from V_{TX} well passes through the stage.
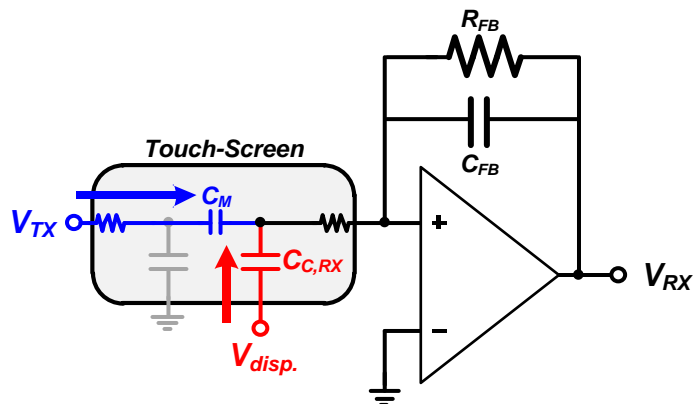
Fig. 2.9 Schematic diagram of touch-screen model and CA.
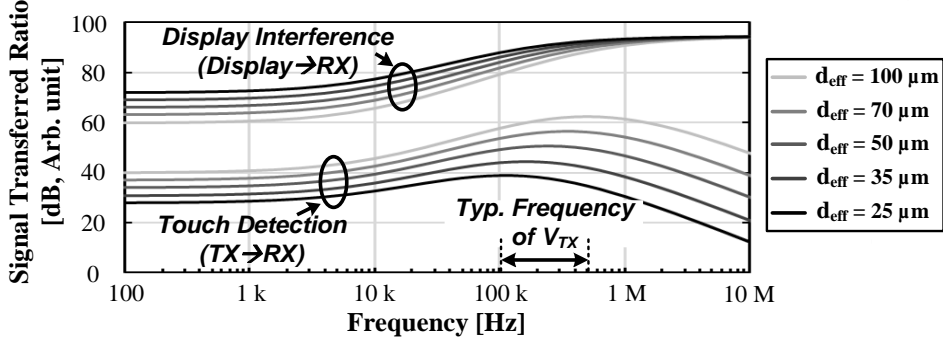
Fig. 2.10 Calculated signal transfer ratio of

touch detecting signal and display interference.

The worst-case display interference is occurred when displaying a stripe-pattern image altering display driving signals. Display lines are driven row-by-row, and the maximum amount of signal transition in data line occurs at the highest frequency while displaying the stripe-pattern image as illustrated in Fig. 2.11. Usually, the display scan time is 60 Hz, thus the frequency of H-sync signal is determined by the overall resolution. As an example, the WQHD+ (1440×2960) OLED the frequency of the H-sync signal needs to be at 180 kHz (~ 60×2960 Hz) to scan the entire display in time. While displaying the stripe-pattern image, maximum amount of signal transition in data line occurs at the highest frequency while displaying the stripe-pattern image. Therefore, the display interference occurs near 90 kHz and its harmonic frequencies. While displaying the stripe-pattern image, signal interference is generated not only with the highest amplitude of interference, but also with the highest frequency. The TSC typically utilizes 100-500 kHz frequency band for mutual-capacitance readout, thus the interference became a critical design issue.
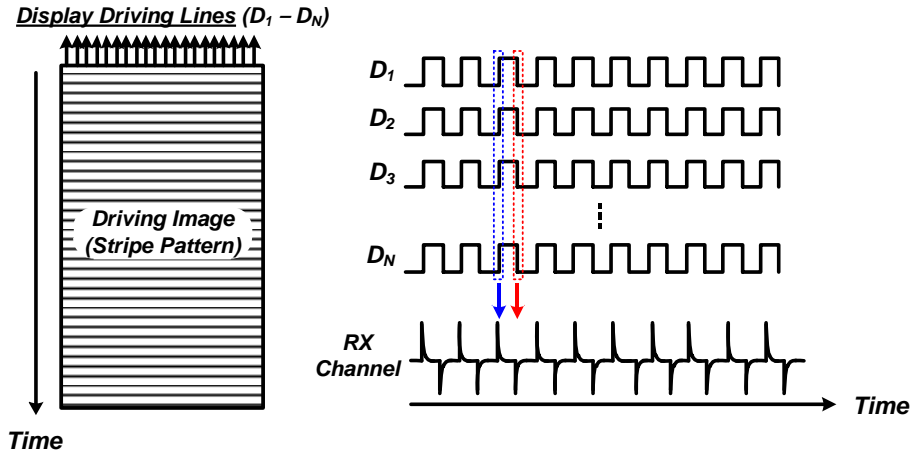
Fig. 2.11 The worst display interference generation.

2.3.3 Lock-in Sensing Structure

In order to mitigate the effect from the display operation and various other inter-ferences such as environmental noise, ramp noise, and charger noise, signals in fre-quency band other than the mutual-capacitance stimuli frequency need to be blocked. In order to substantially attenuate the out-of-band noise, a high order band-pass filter (BPF) needed to be implemented. However, implementation of a high or-der BPF requires large IC area and power dissipation. Moreover, precise location on center frequency of the high-order BPF is necessary, but it requires precise calibra-tion on the BPF.
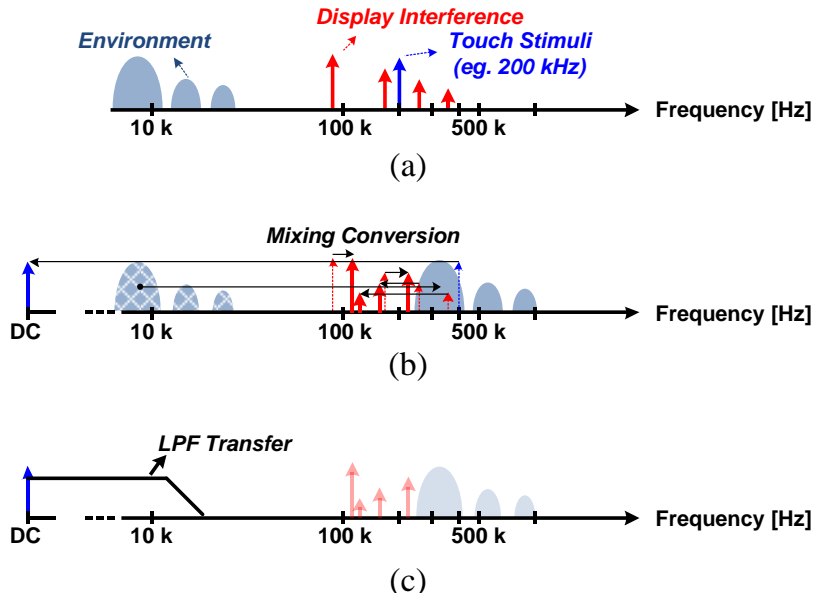
Fig. 2.12 Frequency-band representation of signal and noise. (a) Signal and noise environment, (b) after applying frequency mixing and (c) low-pass filter.

Instead, the lock-in structure has been proposed [2.11] to efficiently implement high order band-pass filtering. Fig. 2.12 describes the lock-in sensing structure with frequency-band representation of signal and noise. A mixer is utilized to down-convert the signal, and a low-pass filter (LPF) attenuates the down-converted signal. Because the signal is mixed with the same frequency of touch stimuli, only the touch signal locates at DC after the down-conversion. Therefore, the LPF with sufficiently low cut-off frequency can block every frequency component other than the stimuli signal, and the cut-off frequency need not be accurate. Moreover, the LPF in low bandwidth can be implemented area- and power-efficiently.

2.3.4 Multi-Channel Driving

Display interference worsen due to closely placed touch-screen and display-related layers, and moreover, less transition of mutual-capacitance occurs as the relative distance between the touch-screen and the object becomes farther due to inevitable protection layer on top of the display panel. Therefore, an accurate sensing of the touch-screen capacitance becomes harder.

As expressed in (2.1), the accuracy of touch sensing AFE is measured by the SNR of the capacitance data at each node. The SNR is improved with an increased stimuli signal power, and an apparent way to enhance touch detect resolution is to increase the signal amplitude of the stimulation signal. With the stimuli signal with n-times higher amplitude, n-times higher SNR is obtained. However, the generation of increased stimulation amplitude requires a high-voltage power supply. Usually, the voltage level higher than 5 V is not provided in the mobile devices, thus a charge pump or boost converter circuit is used which requires extra peripheral components such as capacitors and inductors.

Another way is using a multi-channel drive the TSP with an orthogonal sequence [2.15]. Since the multi-channel driving scheme does not require a high-voltage operation, it is compatible with the general CMOS process. As an example for 4×4 touch-screen channels, Fig. 2.13 compares the time-interleaved single channel driving and the orthogonal multi-channel driving. Signal polarity at each channel is code-modulated, and the modulation can be expressed with a 4×4 matrix, which can be expressed as follows:

$$H_{4\times4} = \begin{bmatrix} 1 & 1 & 1 & 1 \\ 1 & 1 & -1 & -1 \\ 1 & -1 & 1 & -1 \\ 1 & -1 & -1 & -1 \end{bmatrix}. \quad (2.7)$$
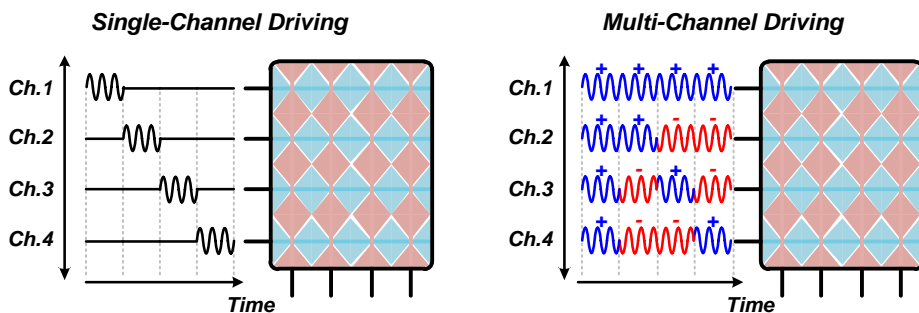
Fig. 2.13 Comparison between single-channel driving and multi-channel driving.
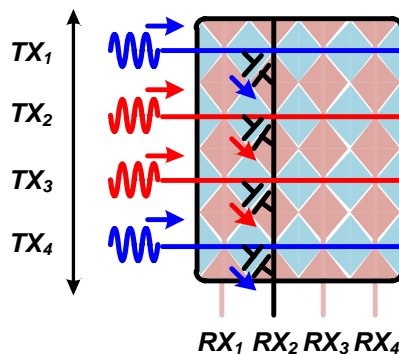
Fig. 2.14 Charge summation on multi-channel driving.

Each column of the $H_{4 \times 4}$ indicates the signal generating sequence, and the row indicates the channel. Likewise, the mutual-capacitance can be expressed in a matrix *C*. According to the modulation matrix, stimuli signal is applied to the TX lines of the touch-screen, and the mutual-capacitance is modulated. When i[th] column of is being generated, signal applied according to the column at the TX lines stimulates the mutual capacitance, and the signal passed through the mutual-capacitances are accumulated along the other side of the touch-screen as shown in Fig. 2.14. The signal accumulation at y^{th} RX line is expressed as (2.8) and can be expressed as a multiplication of *C* and *H* as (2.9). In general, (2.9) holds regardless the size of number of touch-screen channels. Those modulation code which is orthogonal and only consisted with +1 and -1 are called Hadamard matrix (HM).

$$RX_{y,i} = V_{STM} \cdot \sum_{i=1}^{N_{TX}} H_{i,y} \cdot C_{i,y}$$

(2.8)

$$RX = V_{STM} \cdot H^T \times C$$

(2.9)

Signal at the RX channels passes the sensing module. Afterward, the demodulation of the sensing data, *i.e.*, the recovery of mutual-capacitance matrix is performed by multiplying the inverse matrix of H^T. With an orthogonal matrix being used as the modulation code, the mutual capacitance can be easily recovered since $(H^T)^{-1}$ becomes $(H^T)^T = H$. In elementwise, signal transfer in the sensing module is represented as (2.10) and the demodulation is expressed as (2.11), where *A* stands for the overall transfer function of the sensing module and $n_{y,i}$ is the noise residue at the sample.

$$S_{y,i} = A \cdot RX_{y,i} + n_{y,i} \quad (2.10)$$

$$D_{i,j} = \sum_{k=1}^{N_{TX}} H_{i,k} \times S_{k,j} = V_{STM} \cdot A \cdot N_{TX} \cdot C_{i,j} + \sum_{k=1}^{N_{TX}} H_{i,k} \cdot n_{k,j} \quad (2.11)$$

As a result of the demodulation process, the signal term $A \cdot C_{i,j}$ is boosted with N_{TX} while the noise term is added N_{TX} times. The N_{TX} times accumulated noise results $\sqrt{N_{TX}}$ times increased in its RMS, thus, the SNR is improved by $\sqrt{N_{TX}}$.

2.4 Design Issue by Heavy Load

on Signal Generation

2.4.1 Power Budget

An AC signal is applied to the side for mutual-capacitance readout, and as the capacitive coupling became severe, the AFE needs to generate large stimuli for the precise mutual capacitance readout. To enlarge the stimuli, the usage of higher supply voltage for the stimuli generator and/or code divisional multi-channel driving modulation with the limited amplitude of the stimuli are usually considered. For the SNR perspective, the TSC can achieve $\sqrt{N}$-times more SNR with the $\sqrt{N}$-times higher supply voltage and with N-channel multi-driving, which both result in N-times more power dissipation of the driver. However, due to the huge capacitance of the integrated touch-screen structure, the stimulating signal generator is the largest energy dissipating source. The signal generator drives the touch-screen with large parasitic capacitance, and it reaches up to 50 pF/Tile and 1 nF/Channel. Therefore, whichever driving methods is used, the stimulating signal generator would dissipate several tens of mW of power and becomes the largest energy dissipating source.

The FOM of the touch sensing AFE expressed as (2.4) with the power usage in

each module. At least, the mutual-capacitance detecting AFE consists with the stim-
uli generator and the signal sensor, and the power dissipation is expressed as P_{TX} and
P_{RX} respectively. Considering the power-SNR tradeoff described above, the power
consumption of signal generator P_{TX} and resulting SNR can be expressed with its
base value $P_{TX,0}$ and SNR_0, and the trade-off factor N.

$$FoM = \frac{P_{TX} + P_{RX}}{SNR \cdot FR \cdot \#Nodes} = \frac{N \times P_{TX,0} + P_{RX}}{(\sqrt{N} \times SNR_0) \cdot FR \cdot \#Nodes} \quad (2.12)$$

For lower FoM (which is better), the stimuli amplifying factor N can be chosen so
that (2.13) holds.

$$N \cdot P_{TX,0} = P_{RX} \quad (2.13)$$

Specifically, when the power dissipation of signal generator matches the power
dissipation of signal sensing module, the FOM is optimized. However, due to the
heavily coupled touch-screen, the optimal is hard to accomplished: A touch sensing
AFE design with that much power is dissipating on both at the stimuli generation
and the signal sensing module would not be well adopted in mobile applications, and
the AFE that generates small stimuli signal which dissipates power similar to the
sensing module would be overwhelmed by various interferences and not detect the
touch object precisely.

2.4.2 Design Motivation

TSC in mobile devices is required to have precise resolution in touch detection

while dissipating low power. First, P_{TX} can be significantly reduced by driving only when the touch-input is detected. With the coarse detection capability, the fine detection of the touch-input can be done when necessary. Similarly, the technique based on correlated noise sampling can reduce P_{TX}, since the AFE does not generate the stimuli signal during the noise sampling period. Moreover, since the interference from the display operation are relatively constant, the display interference can be reduced significantly. On top of that, a novel adiabatic signal generation method is introduced which can further reduce P_{TX}. Second, an optimally designed signal sensing module of TSC is considered. Based on the requirements of the sensing module such as sample rate, dynamic range, SNR, *etc.*, the optimized sensing module is implemented.

Chapter 3

Low Power Mutual-Capacitance Readout With Adiabatically Generated Stimuli

3.1 Overview

Display panels for mobile devices have continuously become thinner for a better form factor using advanced technologies such as thin-film fabrication of the OLEDs. Thinner encapsulation layer is developed and touch-screens have been integrated into the display to reduce thickness of the entire display module, and the meshed metal touch-screen is located right on the encapsulation layers for the display cells. The touch-integrated display module enables an ultra-thin form factor in the mobile devices, but driving and sensing channels of the touch-screen suffer from significant capacitive coupling from the display panel due to the thin stack-up structure. Moreover, the protecting layer separates the touch-screen and the touch objects farther, causing reduced touch sensitivity. Thus, the touch sensing AFE should be able to sense the mutual capacitance variation in less than a femto-farad level.

Moreover, the worst-case interference exhibits voltage ripple similar to the mutual-capacitance stimuli signal. Electrical model of TSP and the measured display interference are shown in Fig. 3.1. The display scan time is usually 60 Hz, and image is driven row-by-row. Thus, the frequency of H-sync signal for the WQHD+ (1440×2960) OLED is around 180 kHz ($\sim 60 \times 2960$ Hz).

Noise-insensitivity is another requirement of the touch sensing module to detect the diminished mutual capacitance. As mentioned in the previous chapter, interference from display driving operation is mainly concerned for the touch-integrated display panel. Display interference affects the touch-screen channels widely and is treated as commonly coupled noise. Therefore, the AFE usually employs a differential sensing scheme [3.1] to cancel out the interference. However, parasitic resistance offset occurs due to different location of touch channels, and the input common-mode rejection capability of the fully-differential sensing scheme is limited due to the offset. Moreover, considering the location of the display noise tone around 180 kHz and its harmonic components, the filtering stages cannot attenuate the in-band residual interference sufficiently. Since the interference from the display exhibits a much higher level than the touch signal itself, the interference is difficult to cancel out with the fully-differential sensing scheme only. Offsets in fully-differential circuit cause noise residue, and to reduce the effect of the residual interference, noise filtering stages are adopted [3.2].

(a)

(b)

(c)
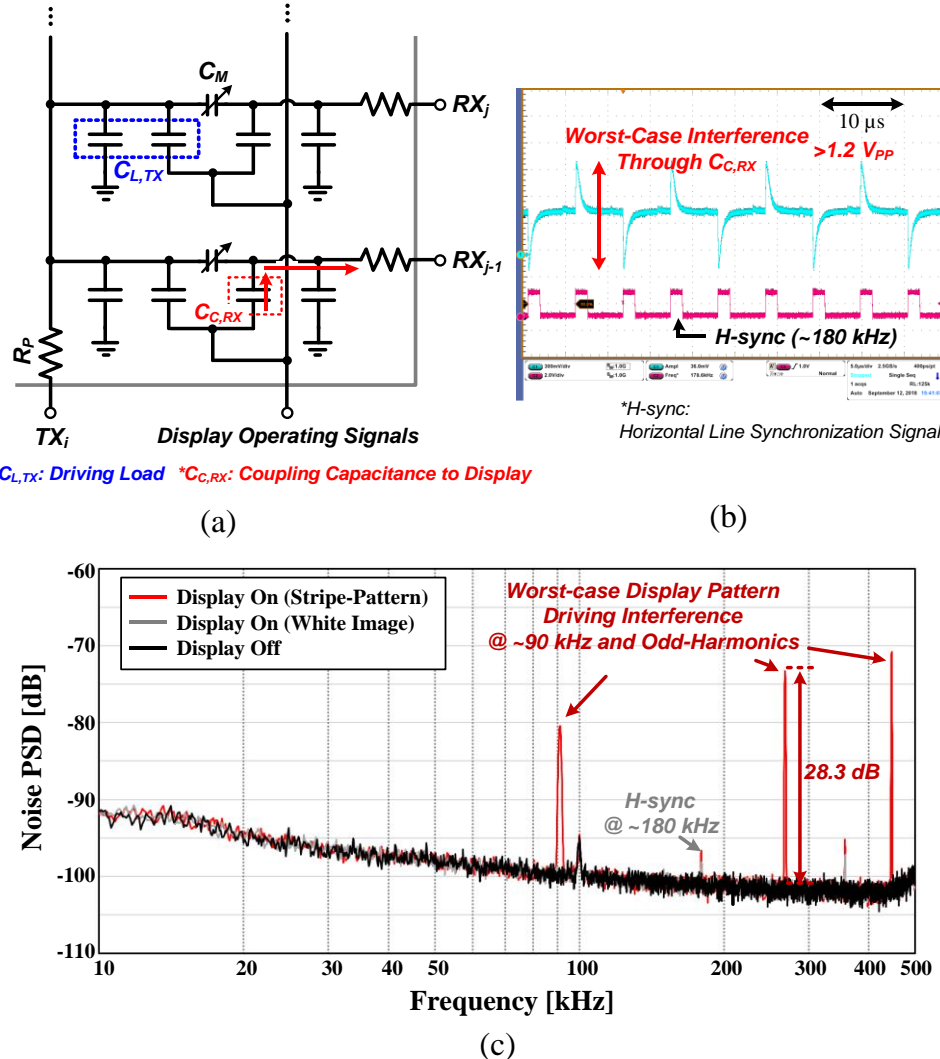
Fig. 3.1 (a) Electrical model of touch-screen, (b) measured worst-case display noise

interference, and (c) power spectral density (PSD) of the noise interference.

In this chapter, a mutual-capacitance sensing touch controller AFE that over-comes the emerging problems associated with touch-screen integrated display panels is presented. An adiabatic stimuli generator combined with multi-channel driving method is proposed. As a result, improvement on the stimuli generation energy-efficiency is achieved especially in the presence of large coupling capacitance. With the energy-efficient touch stimuli generation from the proposed driving scheme, the AFE adopts code divisional multi-channel driving modulation to increase the SNR. Based on an analysis of the switched-capacitor based signal generating method, techniques to reduce peripheral components are suggested to enhance usability in small form-factor applications. A cascaded fully-differential noise filter stages is incorporated for the touch signal sensing module and reduces the interference from various sources. A 4-way multiplexing is applied to the touch sensing module to reduce the number of sensing channels, and a noise-shaping SAR-ADC is used. Against remaining interferences, a system-level nullifying method based on the correlated sampling is applied to further reduce the display interference and flicker noise.

The overall system architecture of the proposed AFE is shown in Fig. 3.2. The touch-screen panel is adiabatically driven by the stepwise charging driver. The multi-channel driving is applied to increase stimulation signal power, and signs of the stimulating signals are generated at the operation controller. The modulation code is used for both code-divided modulation of the touch stimulating signal and demodulation of the sensing data. The mutual capacitance signals of the touch-screen panel are transferred to the touch sensing module. The lock-in structure is

adopted to sense the capacitance signal accurately. In order to mitigate low-frequency noise interference after the lock-in sensing, a correlated sampling-based method is applied by embedding sampling periods among the multi-driving steps. A noise-shaping SAR ADC [3.3]-[3.7] is employed which can provide the reduction of in-band quantization noise.
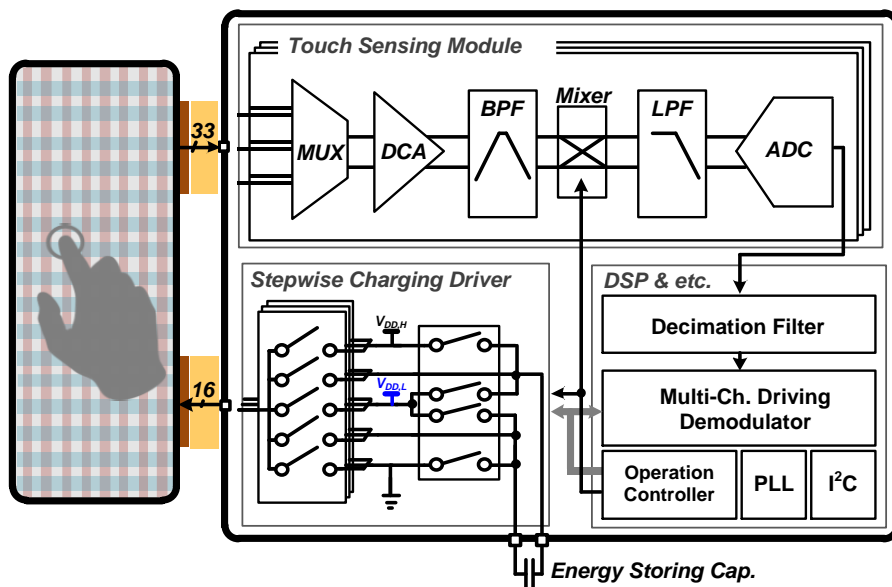
Fig. 3.2 Block diagram of touch sensing AFE

with mutual capacitance sensing capability.

3.2 Adiabatic Charging and Discharging

of a Capacitance Load

3.2.1 History of Adiabatic Driving Scheme

and Motivation for the Proposed Signal Generator

Concept of the adiabatic charging and discharging first came from digital logic designs. CMOS Logic circuits do not dissipate the static power, and the dynamic power which is required to charge and discharge capacitances in the circuit is mainly concerned. Each time a capacitance is charged from 0 to V_{DD}, the power supply provides a quantity of charge CV_{DD} at supply level V_{DD}, hence energy CV_{DD}^2. It is well known that half of energy is dissipated because of the unavoidable parasitic resistance located between the power supply and a capacitance load which makes voltage difference while charging the load. Other than supply voltage scaling for reduced power consumption on charging and discharging a capacitance, the adiabatic charging method had been proposed to reduce power consumption.

As shown in Fig. 3.3, the voltage difference across the parasitic resistance can be reduced as the capacitance is connected to the power supply and the supply is slowly ramped up over a long time (T). While charging the capacitance load from 0 to V_{DD},

the charge transferred will still be CV_{DD}. However, the average current passed through the resistance will be small: CV_{DD}/T, hence the dissipated energy through the process will be $I^2RT = (CV_{DD}/T)^2RT = (RC/T) \times (CV_{DD}^2)$, which is (RC/T)–times less energy dissipation compared to CV_{DD}^2. By charging the capacitance load slowly, the dissipated energy at the resistance can be reduced significantly. The "adiabatic" charging and discharging process is defined by a procedure with no heat flows to any part of a system, and in general, with less energy dissipation than fast ones owing to the low rates of change. The energy dissipation asymptotically approaches to zero with the long-enough T, hence ideal adiabatic operation is achieved.

Several low power designs had been proposed adiabatic charging and discharging scheme with switches which are accurately controlled. Earlier works adopted an
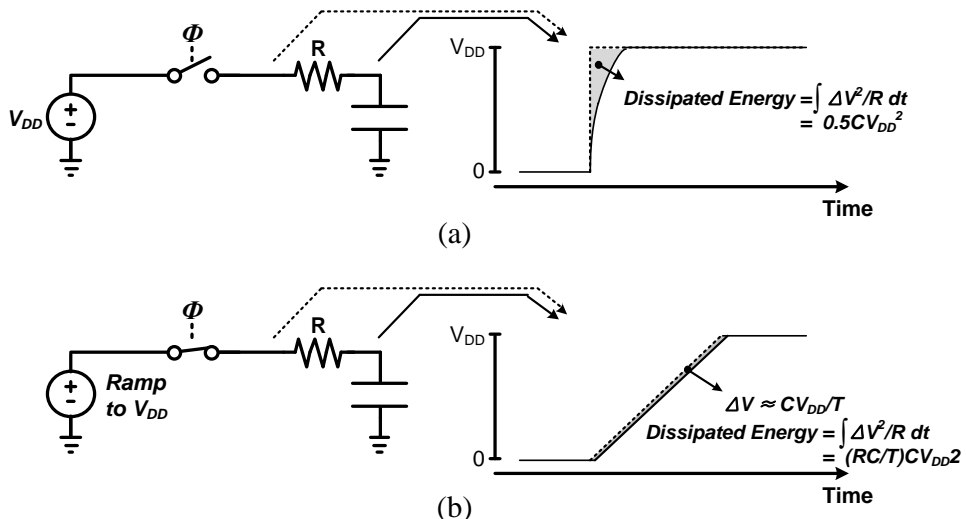
Fig. 3.3 Comparison between (a) conventional and
(b) adiabatic charging scheme with slow voltage ramp.

inductor to generate a voltage ramp on the supply exploiting the resonance phenomenon [3.8][3.9]. This scheme can reduce overall power dissipation significantly, and still be widely adopted in recent low power designs [3.10][3.11] as inductors can be integrated in modern general-purpose CMOS technologies. The resulting the sine wave from the resonance should work as the touch stimulation signal. However, the self-capacitance of the touch-screen increases as a touch object approaches, therefore the resonance frequency will be shifted accordingly. The frequency shift will degrade signal sensitivity and is hard to detect until a touch-event occurs.

Without an inductor, by charging the capacitance load step-wisely forming a stair-case waveform as first reported in [3.13], the amount of energy spent on charging a capacitance load can be reduced significantly. In Fig. 3.4, conventional charging and the stepwise charging are compared. As an example, a 4-step charging and discharging is represented in Fig. 3.4(b). The stair-case waveform replaces the voltage ramp; hence the voltage difference across the resistance is reduced. Dissipated and recycled energy is animated in Fig. 3.5. The stair-case waveform generation is usually performed by a switched-capacitor based voltage converters, and similar to the adiabatic charging scheme using resonance, the stepwise charging scheme is widely adopted in various design fields with the higher capacitance can be utilized as the fine metal pitches can be drawn for the switched-capacitor voltage converters using recent CMOS technologies [3.18] - [3.22]. Unlike those adiabatic charging and discharging schemes for representing digital logic states and clock signal, the proposed signal generation scheme is intended to generate AC signal for the touch detection.
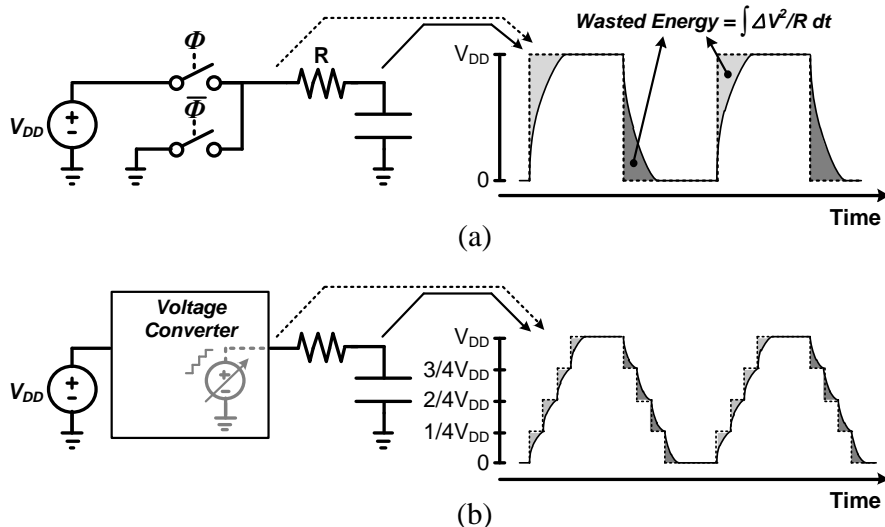
Fig. 3.4 Comparison between (a) conventional and (b) stepwise charging.
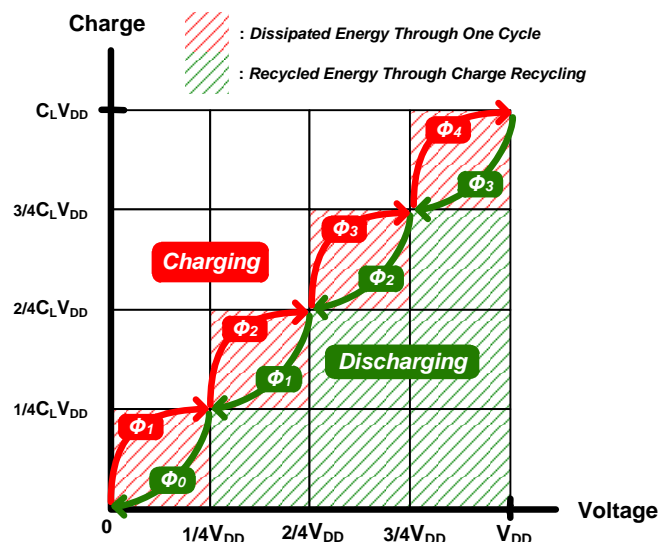
Fig. 3.5 Energy diagram of stepwise charging and discharging in 5-step.

The generated frequency of AC stimuli signal need to be freely located where less environmental noise is detected over the targeted TSP. Therefore, stepwise charging and discharging scheme is mainly considered for the signal generator as the resonance heavily relies on the inductance and capacitance. Moreover, the capacitance of load: self-capacitance of TSP varies as the touch object engages, thus it can alter the energy-saving performance of the resonance-based signal generator.

Waveform of the generated signal is also important as the signal sensing module receives the mutual capacitance data from the generated stair-case signal. Mutual capacitances are modulated with frequency components of the stimulation signal that are determined as coefficients of Fourier series. Among frequency components, the first harmonic component of the signal is recovered in the touch sensing module, thus the signal level of stimulation signal is expressed by the fundamental frequency component of the waveform. Fig. 3.6 visualizes the amount of fundamental frequency component of the signal. The stair-case waveform is plotted along with its fundamental frequency-wave. By definition of the Fourier series expansion, the fundamental frequency component is determined by the integration of inner product of those two waveforms, hence a stair-case waveform with the narrower step occupies the larger amount of frequency component. Narrow steps will result the lack of the energy-saving performance. However, as the energy-efficiency is mostly important for the touch detection at mobile applications, therefore the operating point at the middle of energy-saving performance and the amount of frequency component tradeoff is explored. The stepwise charging and discharging scheme also gives more controllability than the resonance based scheme, hence the tradeoff is examined analytically and experimentally later in this chapter.
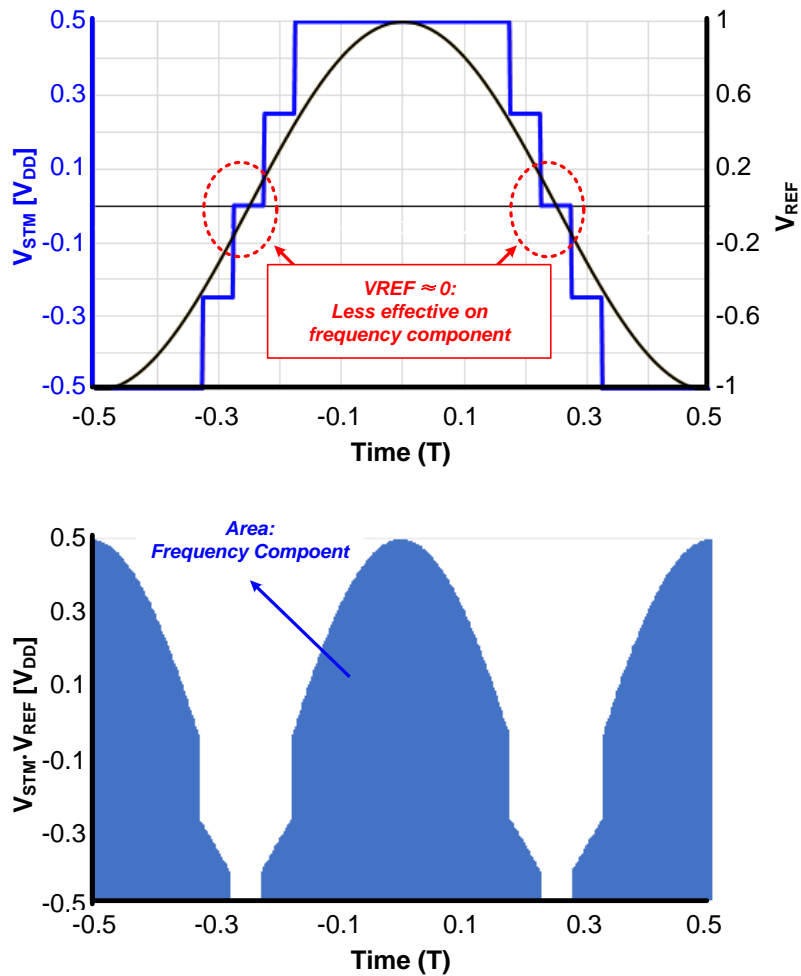
Fig. 3.6 Generated stair-case waveform and a representation on the

frequency component of the waveform.

3.2.2 Ideal Operation

As an example, a stair-case signal generator is shown in Fig. 3.7. During the charging procedure, the conventional pulse-wave generator results in the full-scale voltage difference at the parasitic resistance while the stepwise generator produces less voltage difference using smaller multi-step voltages. In this example, four voltage levels are used for the reduced voltage difference during the charging procedure. As a result, only one-quarter of energy is dissipated while charging the load compared with the conventional scheme. Similarly, less energy is dissipated during the discharging procedure because the stepwise discharging makes smaller voltage
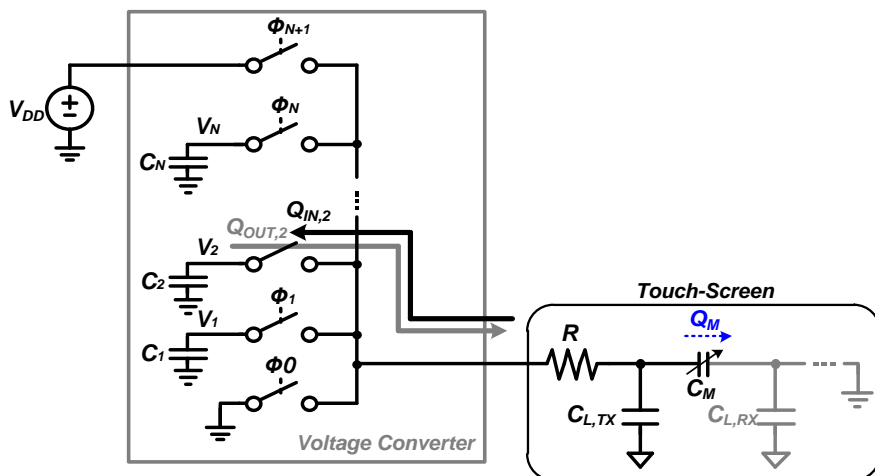
Fig. 3.7 Stepwise charging and discharging scheme with a switched capacitor based voltage converter.

difference across the resistance. At this time, the charge in the load capacitor is re-used while discharging the load in a stepwise manner because the previously driven charge returns back to the voltage converter.

To realize the scheme, switched-capacitors which are laterally placed are used to produce the voltage levels as shown in Fig. 3.7. Switches (Φ_1, Φ_2, …, Φ_{N+1}) are turned on orderly both when charging the load and discharging, and the tank capacitors (C_1, C_2, …, C_N) provides huge capacitive nodes which act as voltage converters keeping the voltage levels during cycles of signal generation. Voltage levels (V_1, V_2, …, V_N) at each capacitive node are generated according to the reused charge when discharging the load. The ith tank capacitor (C_i) provides a quantity of charge to pull-up the load from V_{i-1}-level to V_i-level and absorbs the charge as pull-down the load from V_{i+1}-level to V_i-level in the discharging procedure. Assuming large-enough tank capacitors so that the V_i-level does not vary for one-time pull-up and down. Since each capacitor is only connected to the touch-screen, thus for the following Kirchhoff's current law (KCL) is satisfied for the C_i:

$$(V_{i+1} - V_i) \times C_L = (V_i - V_{i-1}) \times C_L . \quad (3.1)$$

Consequently, KCL for each tank capacitor can be expressed as (3.2), and it results $V_i = \frac{i}{N+1} \times V_{DD}$ in the ideal case of signal generation according to the KCL. Voltage steps are reduced to $\Delta V = \frac{1}{N+1} \times V_{DD}$, therefore the energy dissipated in each charging step is given as $C_L \times (\Delta V)^2 = C_L \times (\frac{1}{N+1} \times V_{DD})^2$ which is repeated N+1 times, hence energy is $E = \frac{1}{N+1} \times C_L V_{DD}^2$ dissipated while charging the load.

$$
\begin{pmatrix}
2 & -1 & 0 & \cdots & 0 & 0 \\
-1 & 2 & -1 & \cdots & 0 & 0 \\
0 & -1 & 2 & \cdots & 0 & 0 \\
0 & 0 & -1 & \cdots & 0 & 0 \\
0 & 0 & 0 & \cdots & 2 & -1 \\
0 & 0 & 0 & \cdots & -1 & 2
\end{pmatrix}
\times
\begin{pmatrix}
V_1 \\
V_2 \\
V_3 \\
\vdots \\
V_{N-1} \\
V_N
\end{pmatrix}
=
\begin{pmatrix}
0 \\
0 \\
0 \\
\vdots \\
0 \\
V_{DD}
\end{pmatrix}
\tag{3.2}
$$

3.2.3 Attenuated Operation

As mentioned previously in Chapter 3.2.1, stair-case waveform with narrower steps will generate higher signal amplitude effectively, but with finite touch-screen bandwidth, the narrower step results in insufficient charge redistribution for the lateral switched-capacitor scheme which leads more energy dissipation. Because of that, a realistic model of stepwise charging and discharging including the R-C delay must be considered. Due to the finite bandwidth of touch-screen, each charging and discharging procedure is not fully finished within the switching time, and the next switching is applied on top of the previous step. The cumulative charging and discharging process in a signal period is analyzed here.

The signal generation requires a set of switching operations at each signal period, and it is repeated. As shown in Fig. 3.8, the switching control signals are generated in sequence and each Φ_i lasts γ_i of time. Symmetric pull-up and pull-down switching sequences are applied for the signal generation.

Each switching process is translated into a voltage-step response of an R-C load.

The intermediate voltages after Φ_i is applied are defined as $V_{r,i}$ and $V_{f,i}$ for charging and discharging sequences, respectively which is represented in Fig. 3.9. The intermediate voltage levels are generated by the V_i voltage levels from the charge redistribution which are expressed as (3.3). τ is the time constant of the touch-screen ($R_P \times C_{L,TX}$), and it is assumed that $V_0 = V_{f,0} = 0$ and $V_{N+1} = V_{r,N+1} = V_{DD}$ for the initial voltage levels for the recurrence relation of (3.3).
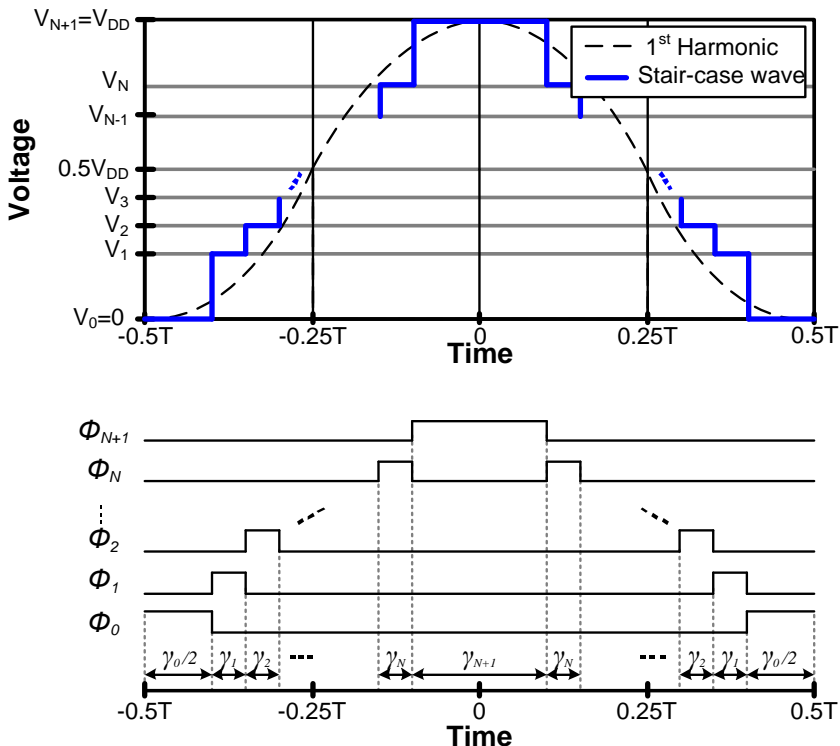
Fig. 3.8 Generated signal and its driving switch pattern.

$$V_{r,i} = V_i \times (1 - e^{-\gamma_i/\tau}) + V_{r,n-1} \times (e^{-\gamma_i/\tau})$$

$$V_{f,i} = V_i \times (1 - e^{-\gamma_i/\tau}) + V_{f,n+1} \times (e^{-\gamma_i/\tau}) \tag{3.3}$$

$(1 - e^{-\gamma_i/\tau}) = \alpha_i$ is the charge re-distribution factor, and the amount of charge inflow and outflow through a cycle is expressed as (3.4).

$$Q_{in,i} = C_L \times (V_i - V_{f,n+1}) \times \alpha_i$$

$$Q_{out,i} = C_L \times (V_i - V_{r,n-1}) \times \alpha_i \tag{3.4}$$

Consequently, the KCL with the attenuated charge re-distribution can be expressed as (3.5), and it results the voltage levels of V_i, $V_{r,i}$ and $V_{f,i}$ in the steady state.
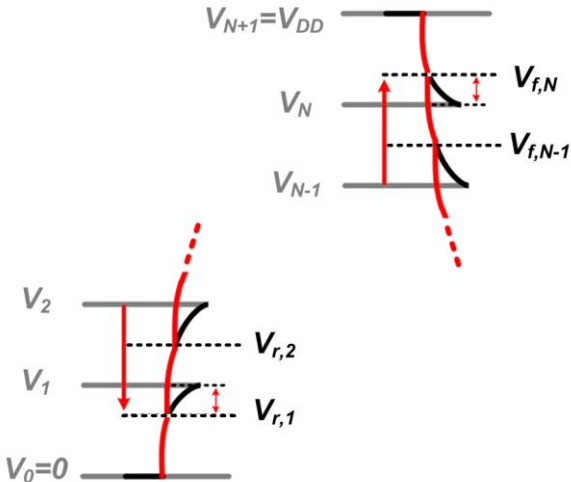
Fig. 3.9 Visualization of $V_{r,i}$, $V_{f,i}$, and V_i-levels.

$$\left(\begin{array}{cccccc} 2 & -\alpha_2 & -\alpha_2(1-\alpha_3) & \cdots & -\alpha_2\prod_{j=3}^{N-1}(1-\alpha_j) & -\alpha_2\prod_{j=3}^{N}(1-\alpha_j) \\ -\alpha_1 & 2 & -\alpha_3 & \cdots & -\alpha_3\prod_{j=4}^{N-1}(1-\alpha_j) & -\alpha_3\prod_{j=4}^{N}(1-\alpha_j) \\ -\alpha_2(1-\alpha_1) & -\alpha_2 & 2 & \cdots & -\alpha_4\prod_{j=5}^{N-1}(1-\alpha_j) & -\alpha_4\prod_{j=5}^{N}(1-\alpha_j) \\ \vdots & \vdots & \vdots & \ddots & \vdots & \vdots \\ -\alpha_{N-2}\prod_{j=3}^{N-1}(1-\alpha_{N-j}) & -\alpha_{N-2}\prod_{j=3}^{N-2}(1-\alpha_{N-j}) & -\alpha_{N-2}\prod_{j=3}^{N-3}(1-\alpha_{N-j}) & \cdots & 2 & -\alpha_N \\ -\alpha_{N-1}\prod_{j=2}^{N-1}(1-\alpha_{N-j}) & -\alpha_{N-1}\prod_{j=2}^{N-2}(1-\alpha_{N-j}) & -\alpha_{N-1}\prod_{j=2}^{N-3}(1-\alpha_{N-j}) & \cdots & -\alpha_{N-1} & 2 \end{array}\right)$$

$$\times \begin{pmatrix} V_1 \\ V_2 \\ V_3 \\ \vdots \\ V_{N-1} \\ V_N \end{pmatrix} = \begin{pmatrix} \prod_{j=1}^{N-1}(1-\alpha_{N-j})V_{DD} \\ \prod_{j=1}^{N-2}(1-\alpha_{N-j})V_{DD} \\ \prod_{j=1}^{N-3}(1-\alpha_{N-j})V_{DD} \\ \vdots \\ (1-\alpha_{N-1})V_{DD} \\ V_{DD} \end{pmatrix} \qquad (3.5)$$

The voltage-level relation matrix is degenerated due to α_is. Solving (3.5) is generally possible for any $\alpha_i s \in [0,1]$, but too much control variables make hard to analyze the operation. Therefore, the uniform step distance of the stair-case waveform is assumed, i.e. $\gamma^* = \gamma_1 = \gamma_2 = ... = \gamma_N$. Fig. 3.10 shows the resulting voltage levels with 8 energy-storing tank capacitors as a result of (3.5) as an example. Voltage levels on the capacitor would find balance at $\frac{i}{N+1}V_{DD}$ for Vi, but the levels are shifted toward to $1/2V_{DD}$ as each charge re-distribution is performed incompletely. The energy-saving performance of the signal generator is also degenerated due to the incomplete amount of charge transition. General solution to (3.5) with the uniform switching gives the same voltage difference among the intermediate levels as follows:

$$\left(V_{i+1} - V_i\right)\big|_{N=N_0} = \frac{1}{N_0 - 1 + \dfrac{2}{(1-\alpha^*)}} \times V_{DD}$$

(3.6)

As an example, the settled voltage level of attenuated charge recycling is shown in Fig. 3.10 for $N=8$. With small α, energy recycling is less occurred, hence less voltage level differences take place between levels. Consecutive charging and discharging leads voltage levels to be balanced from the $0.5V_{DD}$ level.
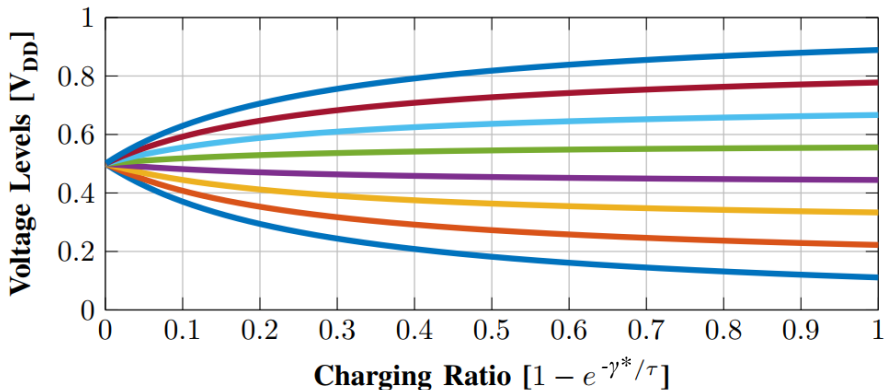
Fig. 3.10 Stored voltage levels at energy-storing tank capacitors.

3.2.4 Energy Efficiency of the Signal Generation

Even if the voltage settles incompletely, there is some recycled energy during the stepwise discharging because the capacitance load is charged up to $V_{r,N}$ without external energy supply connected. The supply dissipates energy while the driver draws electrical charges in order to pull up the load (C_L) lastly (to pull up V_{DD}-$V_{r,N}$ amount

of voltage) from the V_{DD}-level supply. Thus the energy dissipation level can be expressed as follows:

$$E_N = C_L \cdot (V_{DD} - V_{r,N}) \cdot V_{DD}. \quad (3.7)$$

As discussed in [3.13], the amount of dissipated energy to generate the switching signals for the driver itself can affect the overall performance of the signal generation and the optimum driver configuration. In the thesis, it has nonetheless chosen to approximate the energy dissipation of the driver excluding the energy on driving switches to obtain the intrinsic characteristics of the signal generation method.

Highest parasitic resistance appears while routing the touch-screen from an edge of the display panel. Parasitic resistance could reach 1 kΩ for the longest wire from the driver to the TX channel since the wire is very narrow and long since the touch-screen covers the entire area of the display. Despite of the resistance difference due to varied routing distances, the worst-case bandwidth of the channel must be taken into consideration since the AFE adopts multi-channel driving. Thus, analysis on the 200-kHz stepwise charging is applied on a 400-kHz bandwidth channel $\tau \approx 398$ ns in (3.3). In Fig. 3.11, the energy consumption of the driver is plotted as a function of the charging ratio of each step in various configurations of capacitors. Due to limited switching time and touch-screen bandwidth, range in the X-axis is limited, and as more capacitors are used, each switching time becomes shorter and results narrower feasible range. The infeasible range is plotted as the dotted line according to the number of capacitors. Consequently, range in the Y-axis is limited as well, and a limitation of energy reduction is expected at 70% despite used many capacitors.
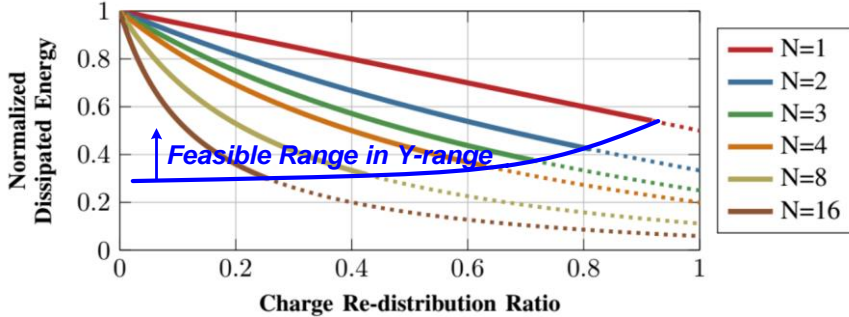
Fig. 3.11 Dissipated energy versus the charge re-distribution ratio.

The amplitude of the stimulation ($|V_{STM}|$) is expressed with the 1st coefficient of Fourier expansion which is expressed as (3.8).

$$|V_{STM}| = \sum_{i=0}^{N} \sin\left(\frac{\pi}{T}\left(\gamma_0 + 2\sum_{j=1}^{i}\gamma_i\right)\right) \times \frac{2}{\pi}\left(V_{i+1} - V_i\right)$$

(3.8)

If the charging/discharging processes occur more frequently with the smaller γ_is for $i \in [1,N]$, the larger signal power can be obtained.

In Fig. 3.12, the frequency component of the generated signal is plotted as a function of the driver's energy dissipation as the number of energy-storing capacitor is varied. The dotted line in the Fig. 3.12 shows the signal generating efficiency of the pulse-wave generator. While both drivers are generating the same signal amplitude, the proposed signal generator dissipates less energy, thus stimulation signal generating efficiency is improved. For example, when generating the signal frequency component of 0.85, the proposed driver dissipates 26% less energy for $N=2$, 28% less for $N=3$, and 34% less for $N=16$ than the pulse-wave generating case.

As explained before, energy efficiency of the signal generation and the touch sensing AFE is mainly considered. Therefore, the maximum efficient point is chosen

for the final design based on Fig. 3.13 which also contains the signal generating efficiency lines additionally drawn on top of the Fig. 3.12. Supplementary lines indicate the same $|V_{STM}|/E_N$-ratio in the graph. Improvement of signal generating efficiency saturated from $N=3$, and more overheads are concerned with higher N since it leads more energy-storing capacitors and more switches for each charging and discharging step. Therefore, the signal generator with three intermediate voltage levels (N=3) is chosen, and the operation point maximizing signal generating efficiency is founded.
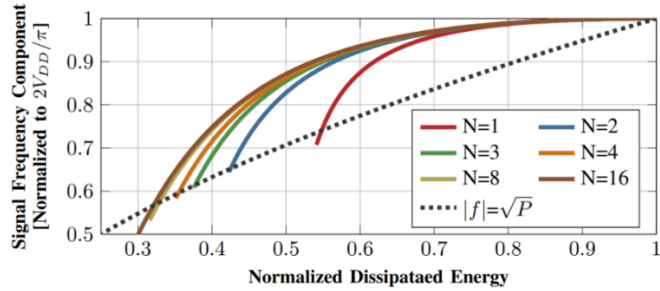
Fig. 3.12 Effective signal amplitude versus the energy dissipation.
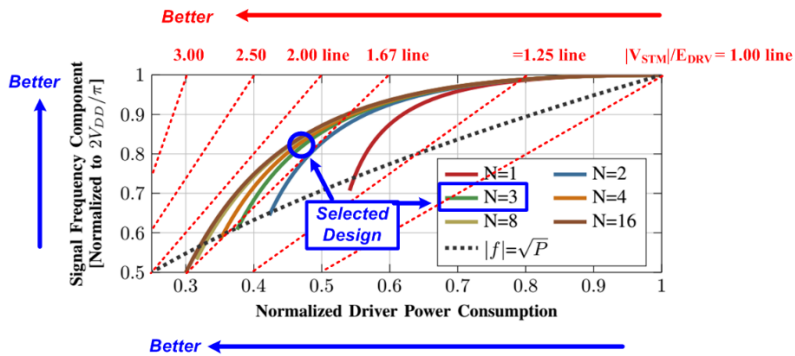
Fig. 3.13 Effective signal amplitude versus the energy dissipation

with supplementary notes.

3.3 Implementation of TX, Signal Generator

3.3.1 Base Design

The analysis held in the previous chapter suggests that it is sufficient to use three energy-storing tank capacitors for the stepwise charging and discharging scheme for the 400-kHz bandwidth TSP. An apparent multi-channel drive stimuli generator circuit with three energy-storing capacitors is shown in Fig. 3.14. Five switches are placed in each driver channel to generate the touch stimuli signal on the touch-screen panel with five levels of voltage steps by sequentially turning on Φ_0 to Φ_4. In each discharging step, the switches are turned on backward, and electrical energy is reused as the driving load is discharged. Ideally, voltage levels at capacitor would find its balance at $V_1=1/4V_{DD}$, $V_2=2/4V_{DD}$, and $V_3=3/4V_{DD}$, and $1/4CV_{DD}^2$ of energy would be dissipated while charging the load. The tank capacitors are shared for driving channels, providing stable voltage level as it is connected to the touch-screen panel.
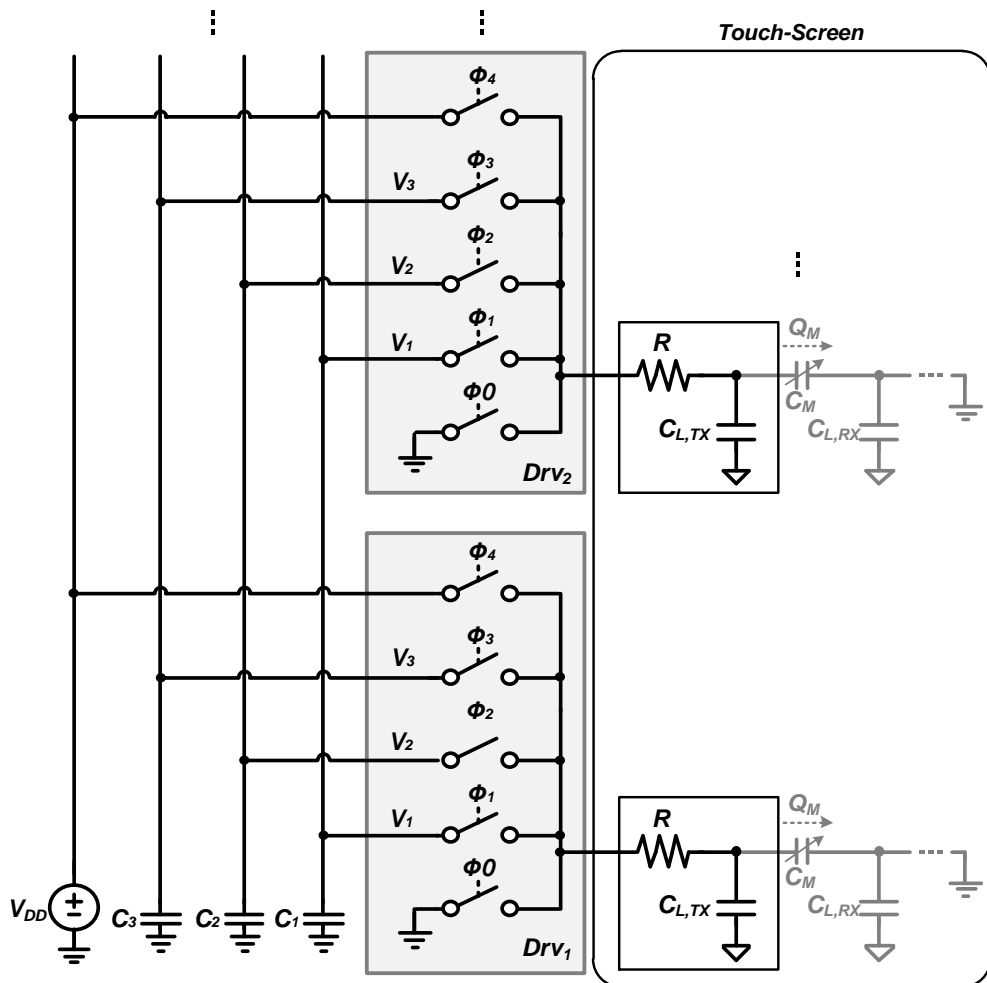
Fig. 3.14 Base design of stepwise, multi-channel drive signal generator.

3.3.2 Capacitor Usage Reduction Techniques

Although reduced energy dissipation can be achieved via stepwise charging and charge recycling, the signal generation scheme requires several capacitors to store voltage levels. In addition, at least 10-times capacitance (several nano-farads) is required for each energy-storing capacitor to prevent voltage fluctuation [3.22], and such a large capacitor is hard to integrate on chip. Smallest number of extra peripheral components is preferred in the touch controller modules because the touch controller is usually mounted on the display glass or a flexible connector module as shown in Fig. 3.15. Therefore, techniques of reducing the use of peripheral components should be considered.
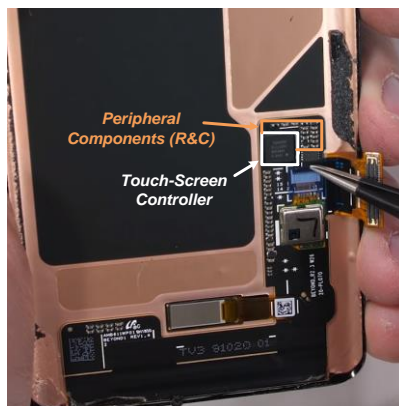
Fig. 3.15 Backplane of touch-integrated display.

* Captured from "Galaxy S10 Teardown" uploaded at YouTube

[**URL: https://www.youtube.com/watch?v=kHzmFPoZbCA**]

1) Alternating capacitor node

A stable voltage level is required while the corresponding switch is turned on during the signal generating operation. The voltage levels can be generated using the switched-capacitor scheme. Several voltage levels can be generated by connecting one of the capacitor nodes connecting to the ground level and the V_{DD} level alternately. Since $V_n + V_{N+1-n} = V_{DD}$ holds while generating the signal symmetrically, the voltage levels can be kept as V_n and V_{N+1-n} accordingly.

For the multi-channel driving scheme, the symmetry of the signal generation can be further exploited because both in-phase and out-phase signals are generated simultaneously. Consequently, when Φ_n switching signal is applied for the in-phase, Φ_{N+1-n} switch is turned on for the out-phase. At that time, the voltage across the energy-storing capacitor can be used for each signal phase as the energy-storing capacitor is treated equivalently as two capacitors in series with its middle node at the common-mode voltage level of $\frac{V_n+V_{N+1-n}}{2}$. During the signal generation, the charge recycling produces $\frac{V_n-V_{N+1-n}}{2}$ across each capacitor.
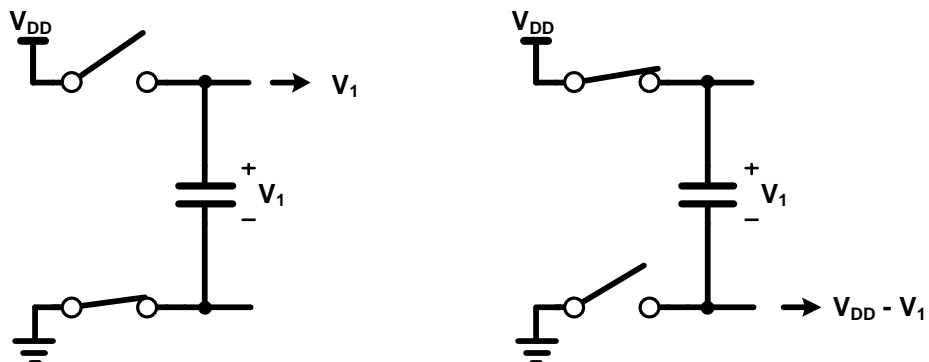
Fig. 3.16 Capacitor node alternation.

2) Charge sharing

With an odd number of energy-storing capacitor, the middle-node voltage level become $V_{DD}/2$. Moreover, when $\Phi_{N+1/2}$ is applied, in-phase and out-phase signals is connected to the same capacitor node with $V_{N+1/2}$. The level can be stored at the AC-ground node, hence the $V_{DD}/2$ level is implemented without the capacitor.

As the final design, a stepwise charging driver that uses three intermediate voltage levels ($N=3$) is incorporated with only one ceramic capacitor is used as the energy-storing device to provide the three voltage levels. The schematic diagram of the signal generator is shown in Fig. 3.17.
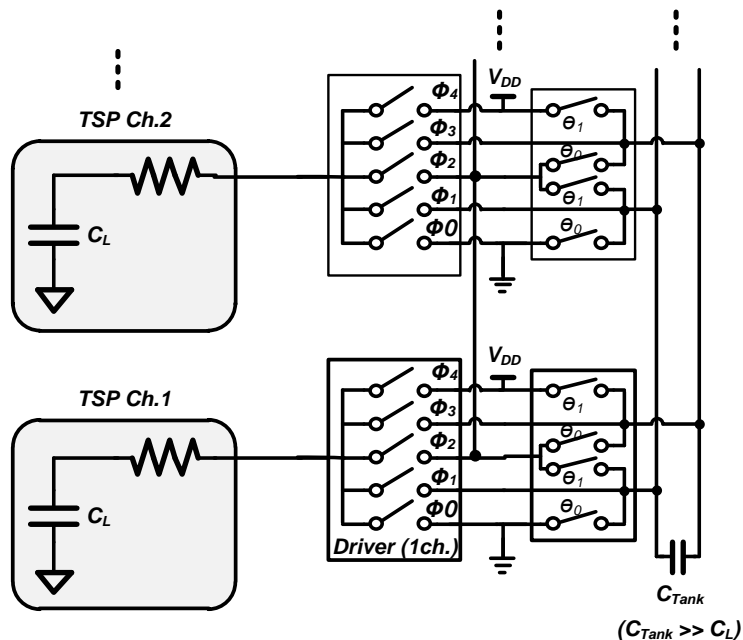
Fig. 3.17 Schematic diagram of the signal generator.

(a)

(b)
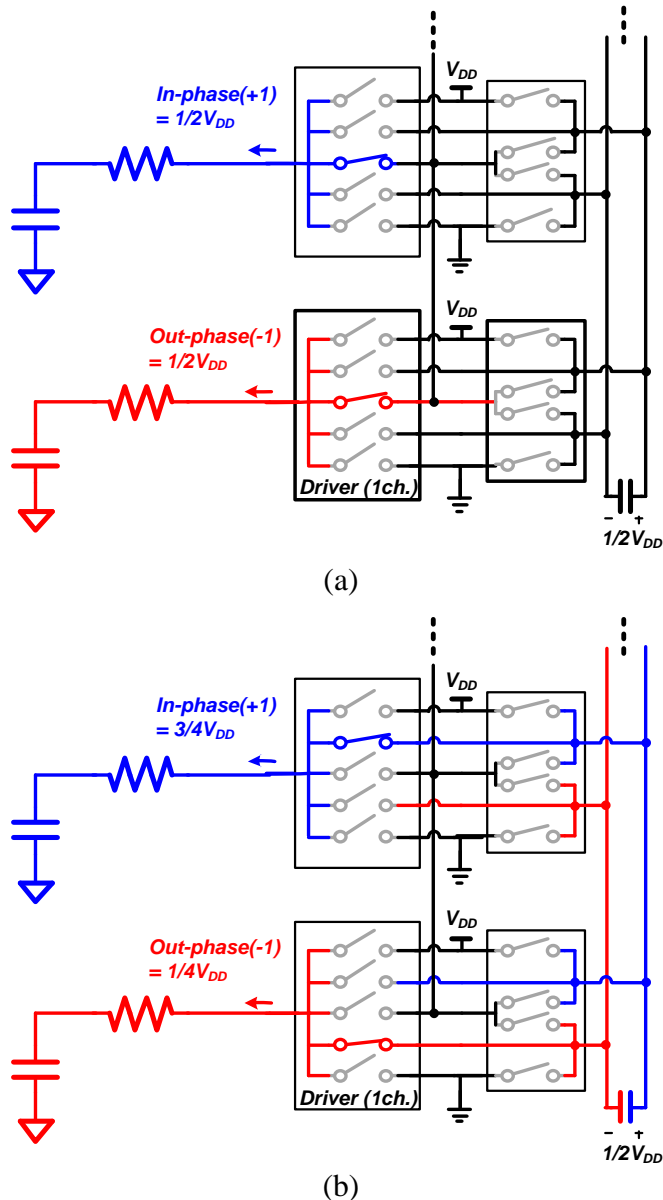
Fig. 3.18 Operation of the signal generator: Part 1.

(a) Φ_2 for both phases and (b) Φ_3 for in-phase and Φ_1 for out-phase.
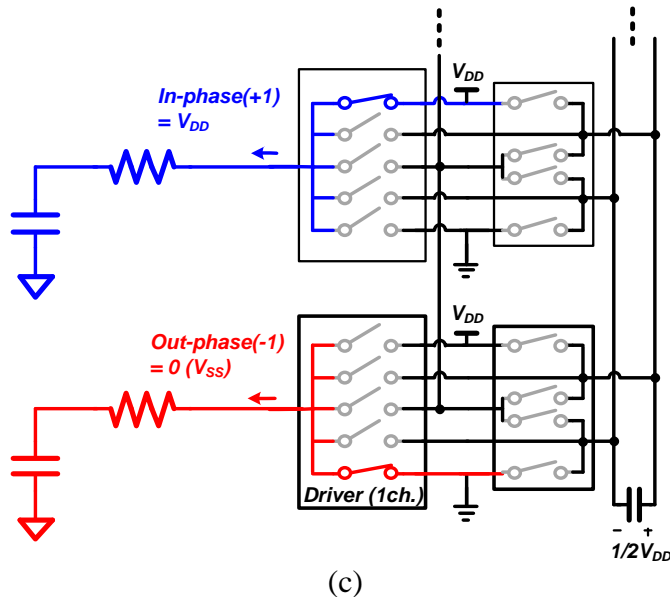
Fig. 3.18 Operation of the signal generator: Part 2.

(c) Φ_4 for in-phase and Φ_0 for out-phase.

In Fig. 3.18, the operation of the signal generation is represented step-by-step. For simplicity, in-phase signal and out-phase signal are lumped into one. The Φ_2 switches are turned on so that the TX channels are at the $V_2=1/2V_{DD}$ level for both in-phase and out-phase signals as shown in Fig. 3.18(a). Next, as represented in Fig. 3.18(b), the driver utilizes the energy-storing capacitor to develop V_3 and V_1 across the energy-storing capacitor as Φ_3 for the in-phase signal generation and Φ_1 for the out-phase signal. Since the capacitance tank capacitor (C_{Tank}) is much larger than the load capacitor (C_L), the voltage across the tank capacitor is not varied. The tank capacitor forces the voltage difference between the in-phase driven channel and the out-phase channel with its storing voltage. The average voltage of the in-phase and

out-phase channels are reserved during Φ_3 for the in-phase signal generation and Φ_1 for the out-phase signal.

The Φ_4 state for the in-phase signal and the Φ_0 state for the out-phase as shown in Fig. 3.18(c), the in-phase driven channels are connected to the V_{DD} supply to pull-up the channel lastly, and the power consumption from the supply happens here. The out-phase channels are connected to the ground to discharge. Then, Φ_3 applies for the in-phase signal generation and Φ_1 for the out-phase signal, in-phase driven channel and out-phase channel are connected as shown in Fig. 3.18(b). Again, the tank capacitor forces the voltage difference between the in-phase driven channel and the out-phase channel with its storing voltage. Afterward, both phases of signals are driven by Φ_2 switches and become both $1/2V_{DD}$ due to charge sharing. Operation represented through here, which can be represented with Fig. 3.18(a) → (b) → (c) → (b) → (a), is stimuli signal generation through a half of its period as represented highlighted region in Fig. 3.19. The operation principle is the same for the next half period.

Charge recycling occurs when the state of driver transits from Φ_1 /Φ_3 to Φ_2 because the voltage difference between the in-phase channel and the out-phase channel before the Φ_2 state was V_{DD} and now it is forced to become the stored voltage across the tank capacitor. On the contrary, while the state moves Φ_2 to Φ_1 /Φ_3, stored energy is consumed while developing voltage difference between two phases of stimuli. These charge recycling and energy consumption occur the same amount of times as the stimuli is generated, thus the stored voltage across the tank capacitor would become $V_{DD}/2$ in ideal.
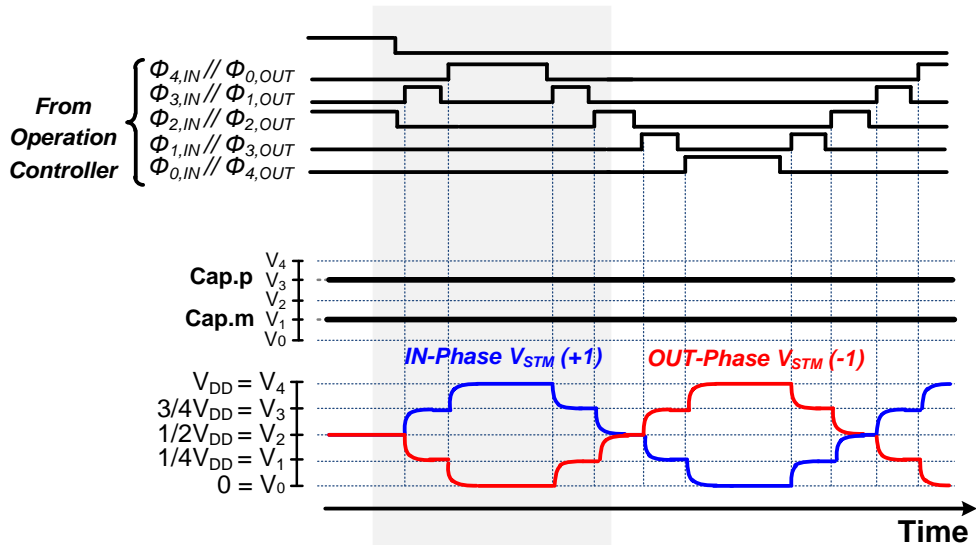
Fig. 3.19 Timing diagram of the signal generator.

To increase the signal amplitude, the stimulation generator typically uses a higher supply voltage than the rest of the AFE. Considering the touch sensor system is required to have good form-factor to be integrated with the display module, drawing an additional supply voltage line imposes a significant overhead. Optionally, with the same circuit, an voltage-boosting scheme is also integrated in the switched-capacitor based driver to generate the I/O voltage level-equivalent, higher voltage supply $V_{DD,H}$ from the core voltage level, $V_{DD,L}$. Fig. 3.20 shows the operation sequence of voltage-boosting signal generator, V_2 of the signal generation is replaced to $V_{DD,L}$. During Φ_2, the capacitor is charged since the tank capacitor is connected to $V_{DD,L}$

(a)

(b)
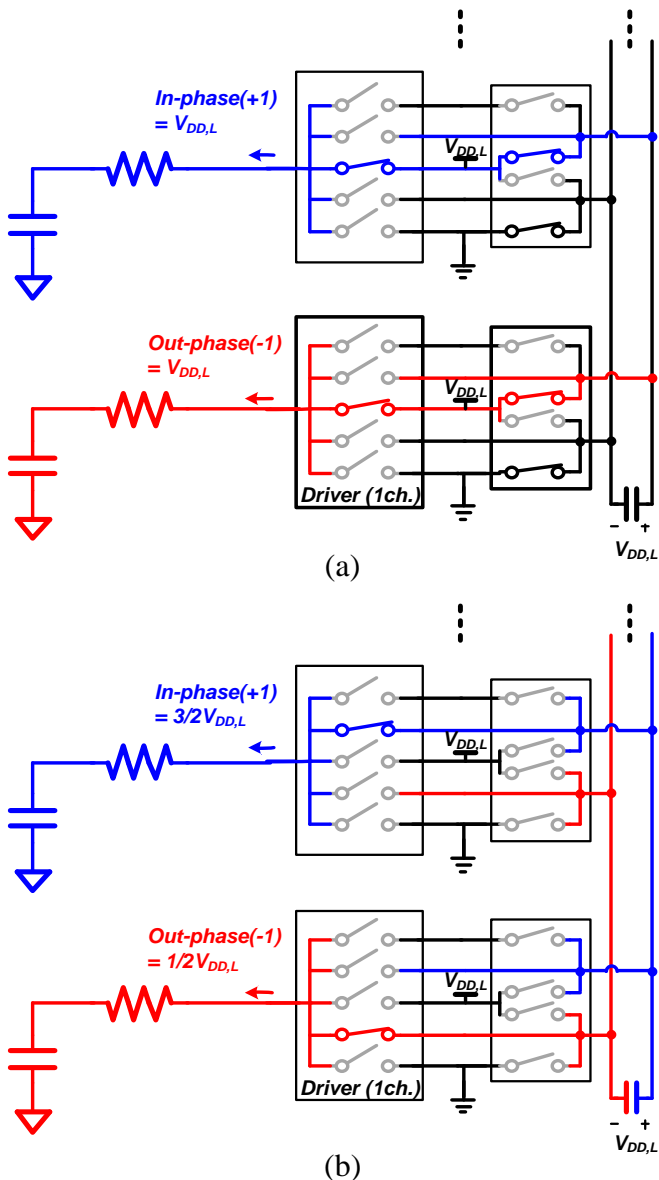
Fig. 3.20 Operation of the signal generator in voltage-boost mode: Part 1.

(a) Φ_2 for both phases and (b) Φ_3 for in-phase and Φ_1 for out-phase.
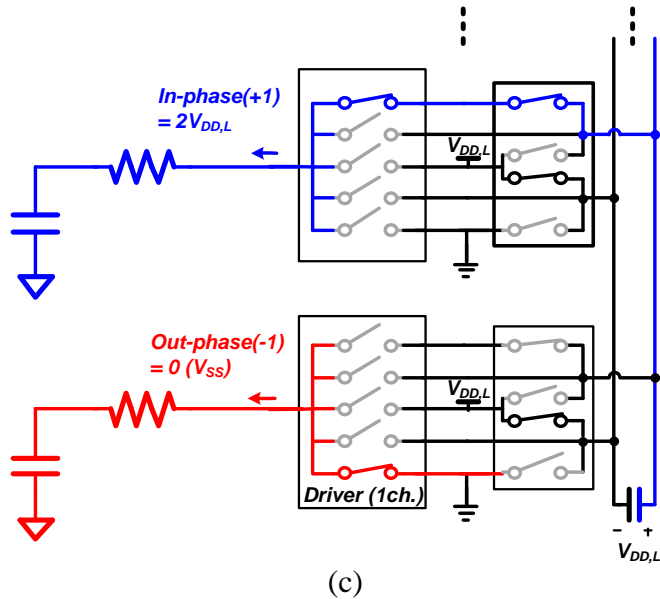
Fig. 3.20 Operation of the signal generator in voltage-boost mode: Part 2.

(c) Φ_4 for in-phase and Φ_0 for out-phase.

while the other node is connected to the ground. In Φ_3 and Φ_1, the tank capacitor forces the voltage difference $V_{DD,L}$ between the in-phase driven channel and the out-phase channel and results $3/2V_{DD,L}$ at the in-phase driven channel and $1/2V_{DD,L}$ at the out-phase channel. Then in Φ_4 and Φ_0, the capacitor node at the lower voltage level is connected to the $V_{DD,L}$ supply, pushing the higher voltage node to the voltage level worth $2V_{DD,L}$, and the in-phase or out-phase signals reaches V_4. The timing diagram of the signal generator with voltage-boosting scheme is shown in Fig. 3.21 which exhibit similar waveform to the normal operation which is shown in Fig. 3.19.
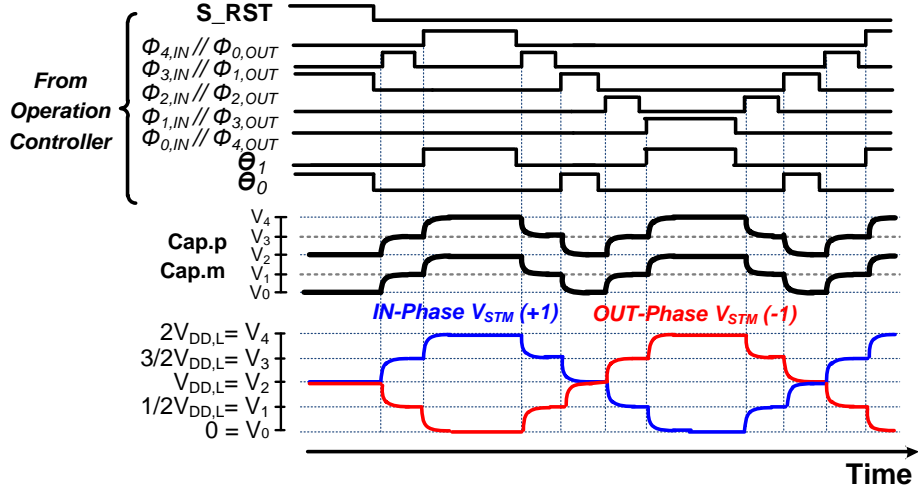
Fig. 3.21 Timing diagram of the signal generator in voltage-boost mode.

Schematic diagram of actual touch stimuli generator is shown in Fig. 3.22. Switches which operates only in the voltage-boosting mode is labelled as θ-switches as shown in Fig. 3.17 and 3.22. The θ-switches need not be operated separately according to the modulation code for different stimuli signal polarity, thus one set of θ-switches are implemented.
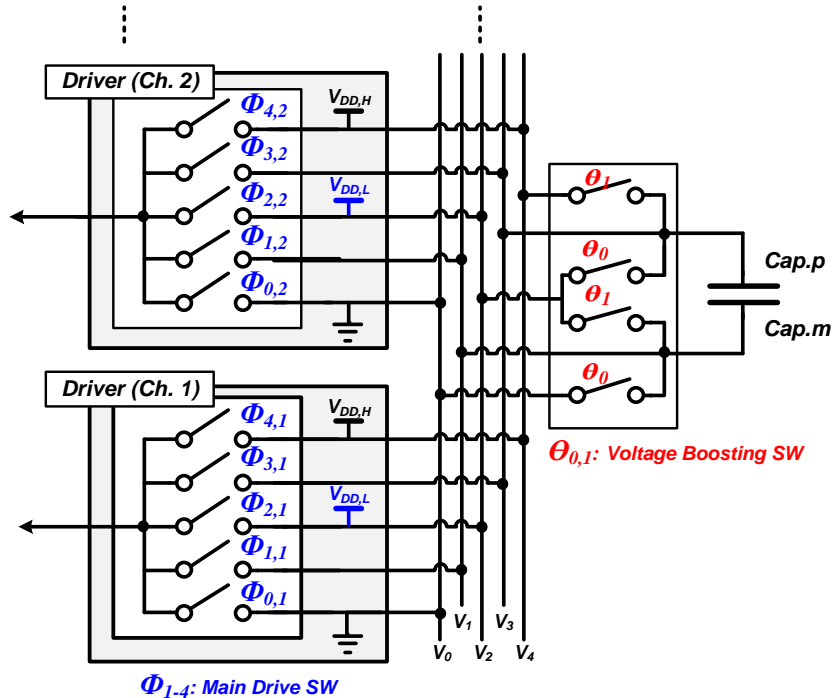
Fig. 3.22 Schematic diagram of the signal generator in actual.

3.3.3 Energy-Storing Capacitor Selection

Until here, the requirements of tank capacitor are not discussed other than its size. Since the signal generator utilize switched-capacitor techniques with the tank capacitor, parasitic component of the tank capacitor should be considered. Structure of a ceramic capacitor is shown in Fig. 3.23(a). Thin layers are piled forming capacitance between the internal electrodes, and the electrodes are connected to the relatively thicker foundation electrode and plate layer. The thicker layers enhance the Q-factor

of the capacitor as it reduces parasitic resistance, but the layers inevitably cause inductance as magnetic field is generated as current flows. Due to the inductance, the capacitor would not act as capacitor beyond the self-resonating frequency (SRF). The resulting frequency characteristic of the capacitor is shown in Fig. 3.24. The operation controller uses 20-MHz clock, and minimum switching pulse width is 5 µs, hence a 100-nF capacitor which has SRF higher than 20 MHz is chosen.

(a) (b)
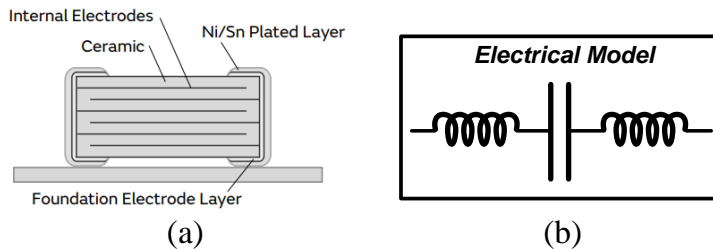
Fig. 3.23 (a) Structure of ceramic capacitor and (b) its equivalent model.

* Fig. 3.23(a): image acquired from muRata product specifications Sep. 2017, at 42 page.

[URL: https://www.murata.com/~/media/webrenewal/support/library/catalog/products/capacitor/mlcc/c02e.ashx])
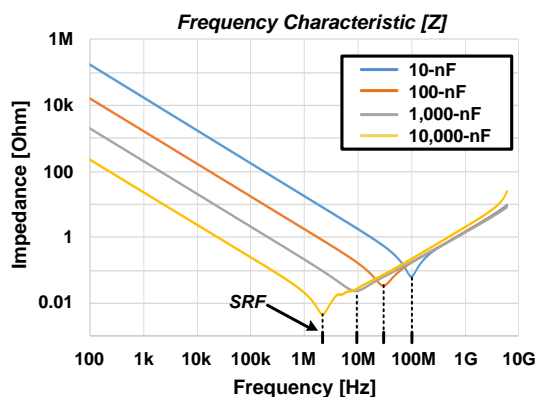
Fig. 3.24 Impedance profile across capacitor.

3.4 Implementation of RX, Signal Sensing Architecture

3.4.1 Design Considerations

Based on the stepwise charging and discharging method which is presented previously, the energy-efficient stimuli generation become possible. Therefore, the touch signal sensing is coherently targeted for energy-efficiency to accomplish the optimized signal sensing according to the power budget of touch sensing AFE as previously described. Besides, the display noise interference through the large parasitic capacitance needs to be cancelled, and a fully differential scheme is adopted because the interference occurs commonly across the sensing channels. The interference occurs all over the touch-screen, thus the AFE usually employs the differential sensing scheme to cancel out the interference. However, parasitic resistance offset occurs due to different location of touch channels, and the input common-mode rejection capability of the fully-differential sensing scheme is limited due to the offset. Since the interference from the display exhibits a much higher level than the touch signal itself, the interference is difficult to cancel out with the fully-differential sensing scheme. To reduce the effect of the residual interference, noise filtering stages are adopted to selectively recovers the mutual capacitance data modulated with the

frequency of stimuli signal. Against undesirable remain interferences, a system-level nullifying method based on the correlated sampling is applied to further reduce the display interference and flicker noise.

For the data conversion, the SAR ADC is adopted for its good energy efficiency. However, a conventional SAR ADC lacks detecting resolution. To overcome the tradeoff, the noise-shaping SAR ADC was proposed [3.3] which increases signal detecting resolution by re-evaluate the signal residue, and as a result, improved signal detecting resolution is achieved. In the proposed system, the noise-shaping is processed by a charge sharing which act as a 2nd-order passive-FIR filter.

The targeted touch-screen for mobile application has 16 TX channels, which is quite small in number of channels compared to [3.41], [3.44], and [3.54]. Therefore, scanning whole touch-screen does not need as many steps, and plenty of sensing time could be designated for each sample. Here, power-efficient touch sensing is achieved by applying multiplexing to the sensing module with reduced number of channels rather than sensing the signal in a long time less effectively.

3.4.2 Fully-Differential Noise Filtering Stages

As previously mentioned, there are many noise sources that disturb the detection of touch object. To cancel out the noise residue, several filtering stages are adopted. The touch sensing module recovers the mutual capacitance of the touch-screen. The schematic diagram of the sensing circuits is shown in Fig. 3.25. Each channel of the sensing module is connected to the corresponding RX channels of the touch-screen,

and the fully differential scheme is employed to cancel out the commonly coupled noise. The differential charge amplifier (DCA) senses difference of mutual capacitance between two adjacent sensing channels. The DCA also provides the 1st-order high pass filtering. The mixer provides down-conversion of the modulated capacitance signal, and the following the 2nd-order multi-feedback (MFB) low-pass filter (LPF) further attenuates out-of-band noise in the down-converted capacitance signal. The band-pass filter (BPF) in front of the mixer prevents out-of-band noise from being folded into the signal band during the down-conversion process. The MFB structures are adopted because higher order of noise filtering can be done. Around the center frequency, the MFB BPF attenuates lower frequency with one zero and higher frequency with three poles. The MFB LPF can incorporate two poles. Without further stages, the out-of-signal band noise can be suppressed intensively with the MFB filters, thus an energy-efficient sensing is achieved. After the analog noise filtering stages, the noise-shaping SAR converts the signal into digits, then a cascaded integrator-comb (CIC) based decimation filter is adopted to recover the over-sampled data. Here, the noise filtering stages in the signal sensing module is described in order.

Fig. 3.26 shows the half circuit of DCA and its transfer function. The half circuit of each noise filter is described for clear presentation. The stimuli signal is transmitted through the mutual capacitance of touch-screen C_M, and the transmitted charge signal is converted with voltage signal which is proportional to the feedback capacitor, C_{FB}. Moreover, the DCA performs high-pass filtering owing to the feedback resistor R_{FB} making a pole at $\omega_p = (R_{FB} \times C_{FB})^{-1}$.
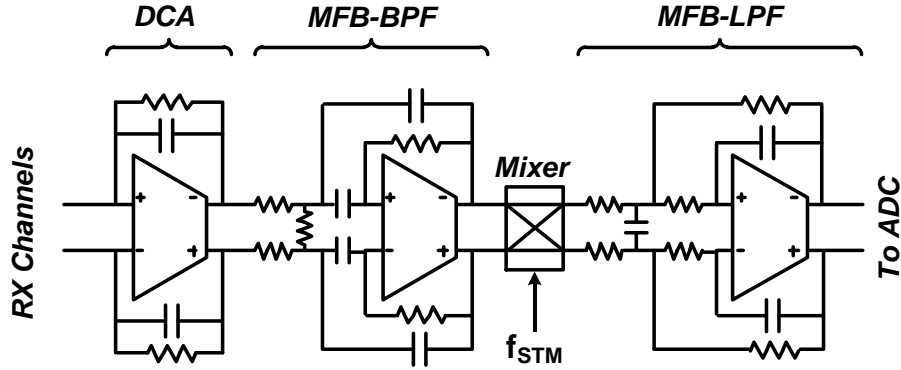
Fig. 3.25 Block diagrams of fully-differential sensing circuits at each RX channel.
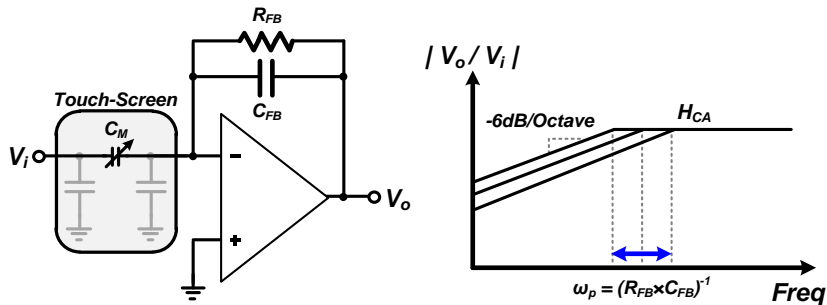
Fig. 3.26 Half-circuit of DCA and its transfer function.
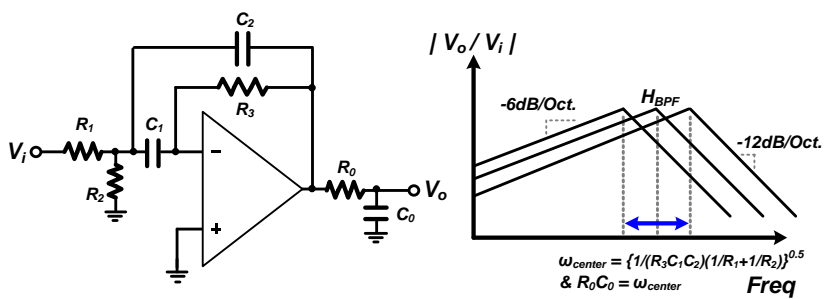
Fig. 3.28 Half-circuit of MFB-BPF and its transfer function.

Since the DCA locates at the very first of the sensing module, the DCA is required to have wide common-mode input range and the DCA becomes the dominant source of inner-circuit noise. Therefore, the operational transconductance amplifier (OTA) of DCA needs a careful design. Fig. 3.27 shows the schematic diagram of the OTA for DCA. A rail-to-rail stage is used for the input-stage of OTA, and it steers current according to the input voltage V_i with both NMOS and PMOS for the wide input common-mode range. Current difference which is eventually provided to the telescopic amplifying stage is only occurred due to different V_i in differential mode. Afterwards, the class-A amplifier is used for the output stage.
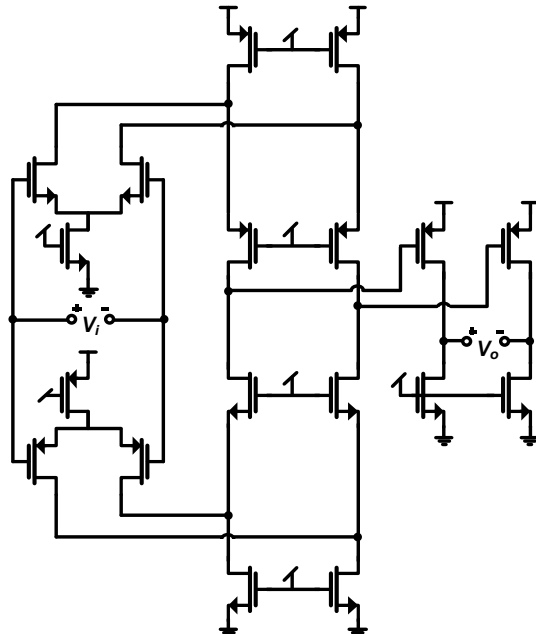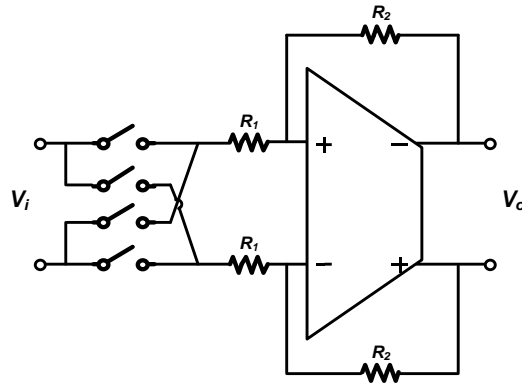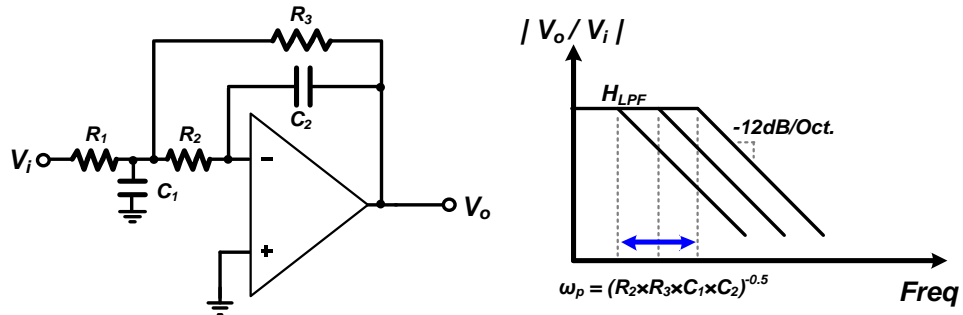
Fig. 3.27 Schematic diagram of differential amplifier for DCA.

Fig. 3.28 shows the half circuit of MFB BPF and its transfer function. Cascaded with the DCA, the DCA followed by MFB BPF stage offers -12dB/Octave attenuation of out-of-signal band for both lower and higher frequency. Several configurations for pass-band of the filters are needed in case of different frequency of stimuli being used. The center frequency of MFB BPF is given as follows:

$$\omega_{\text{center}} = \sqrt{\frac{1}{R_3 C_1 C_2}\left(\frac{1}{R_1} + \frac{1}{R_2}\right)} \qquad (3.11)$$

The mixer down-converts the mutual-capacitance modulated signal. Afterwards, the MFB LPF further attenuates the down-converted signal offering -12dB/Octave noise filtering. The attenuation of high frequency before and after the mixer is also important to prevent aliasing. Mixing of the signal is usually done with complementary switching which is equivalent to multiplication of a pulse. Hence, frequency components at not only the mixing frequency but also its harmonic frequency are down-converted to DC. Noise and interference in the harmonic frequency of touch stimuli signal would also be recovered without BPF or LPF, thus noise filtering before and after the mixer is crucial. Fig. 3.29 shows the block diagram of the mixer, and Fig. 3.30 shows the half circuit of MFB LPF and its transfer.

Fig. 3.29 Block diagram of mixer.

Fig. 3.30 Half-circuit of MFB-LPF and its transfer function.

3.4.3 ADC

After the noise filtering stages, the noise-shaping SAR ADC converts the touch signal into digit form. SAR ADC is adopted for its good energy efficiency, but a conventional SAR ADC is limited in detecting resolution with less than 10 bits. Therefore, a noise-shaping SAR ADC is adopted. The noise-shaping SAR increases signal detecting resolution by re-evaluate the signal residue. In the sensing module

of the TSC, the noise-shaping is processed by a charge sharing which act as a passive-FIR filter. Fig. 3.31(a) shows the schematic of the ADC and Fig. 3.31(b) shows its timing diagram. After the normal SAR operation, the noise-shaping switches are turned on in a row. At Φ_{NS1}, the signal residue at C_0 is delivered to C_1. At Φ_{NS2}, the signal residue is processed while charge sharing occurs, and the current residue is processed with former residue. At Φ_{NS3}, the passive-FIR further processed. The signal flow diagram of the noise-shaping SAR is shown in Fig. 3.31(c). Size of the capacitors are set as $C_0=C_2=C_3$, $C_0=C_1\times 3$, therefore the noise transfer function can be expressed as shown in the Fig. 3.31(c). As results, the quantization noise is shaped in 2nd-order in low-pass band, and since the ADC converts the signal at the DC, better capacitance resolution is achieved via noise shaping technique.

The oversampled data is decimated to represent the sample data at each sequence. The decimation filter with cascaded-integrator-comb (CIC) structure [3.31] is adopted. The signal flow diagram of the decimation filter is shown in Fig. 3.32(a), which is consisted of integrators, a down sampler, and differentiators. Integrators and differentiators are cascaded three times, representing the order of CIC filter. The magnitude response of the filter is shown in Fig. 3.32(b). To attenuate the high frequency component boosted in 2nd-order by the noise-shaping technique applied at the SAR ADC, more than 3rd-order of CIC is required. However, as the order of CIC filter increases, more latency occurs at the decimation, thus 3rd-order CIC filter is implemented.

(a)

(b)

$$D_{OUT} = In + (1-0.75z^{-1})^2 Q$$
$$(C_0=C_2=C_3, \ C_1=1/3C_0)$$

(c)
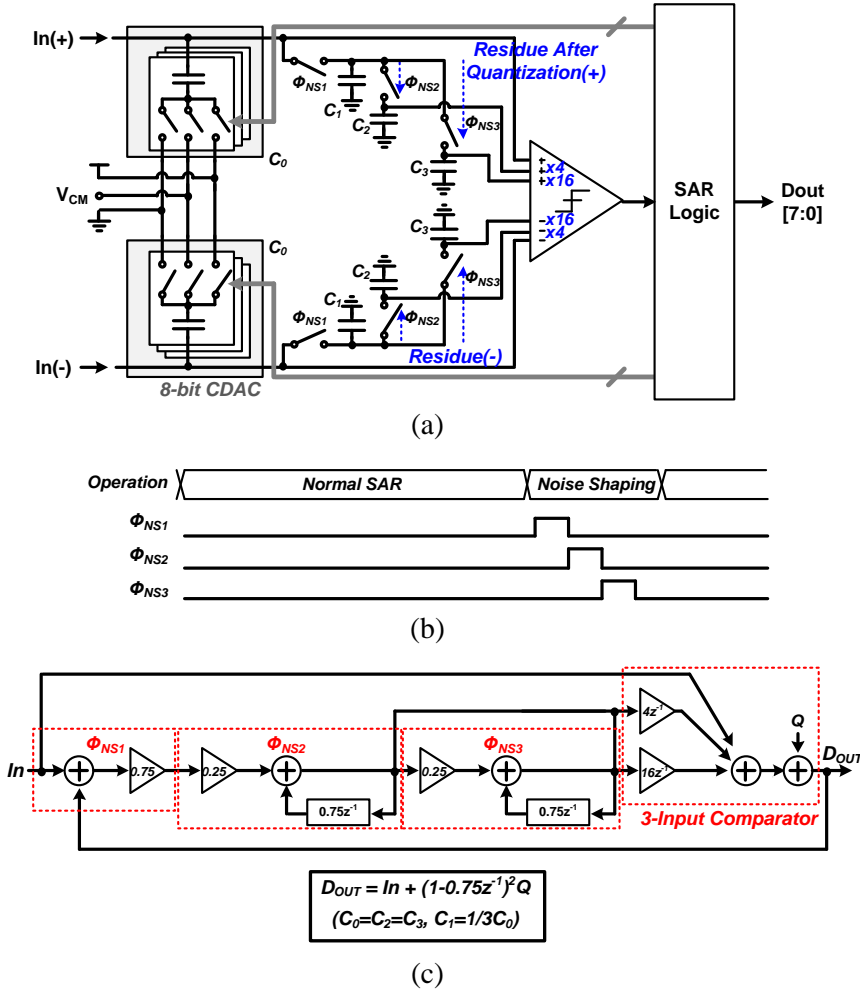
Fig. 3.31 (a) Schematic diagram, (b) timing diagram, and (c) signal flow diagram of the noise-shaping SAR and the resulting quantization noise transfer.

(a)

(b)

(c)
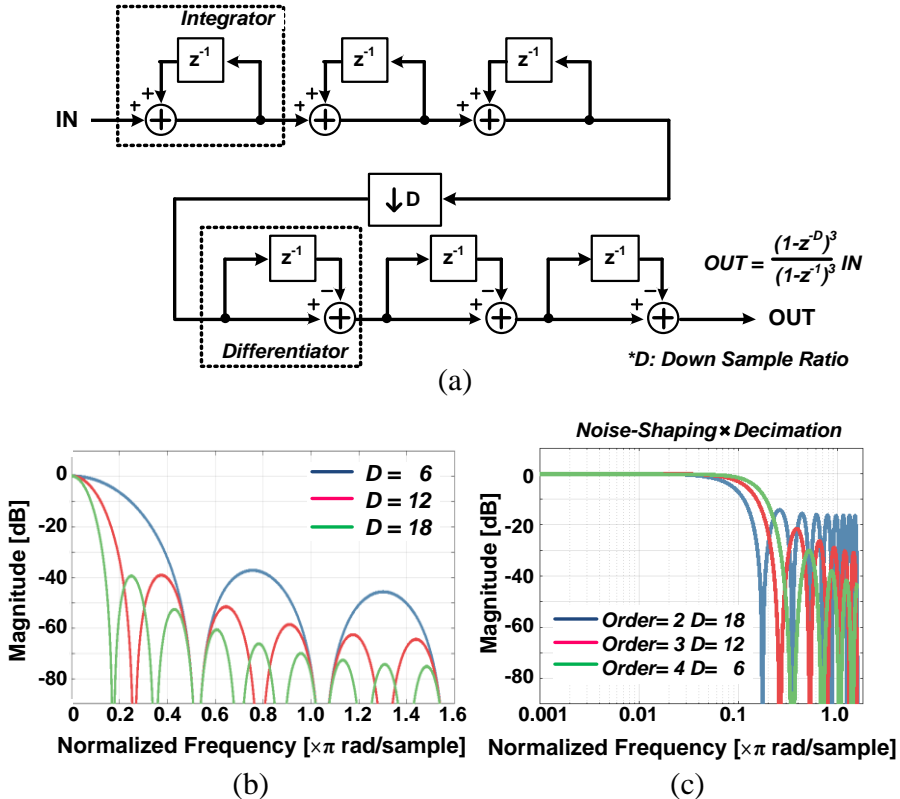
Fig. 3.32 (a) Signal flow diagram of 3rd-order CIC decimation filter,

(b) its magnitude response according to the down sample ratio,

and (c) magnitude response of noise shaping and decimation filter.

3.4.4 4-way Multiplexing on Sensing Module

There is another trade-off between the scan rate and resolution; Less resolution is achieved with higher scan rate in general. The out-of-band interferences are filtered

through the sensing module. The in-band interference remains along with the mutual-capacitance signal, and the residue is averaged during the oversampling. Touch signal and the resulting noise in frequency domain can be expressed as shown in Fig. 3.33. Here, -40 dB of signal is assumed to be transferred through the mutual-capacitance compared to the amplitude of stimuli signal generated from the charge recycling driver, and the magnitude of capacitance signal is determined according to the bandwidth of sensing module. The quantization of 8-bit SAR ADC is shaped and passes through the decimation filter. Therefore, the SNR is estimated as shown in Fig. 3.33. The *SNR × Sample rate* is maximized at 10-μs sample time as the improvement of SNR is saturated. Below the maximum sample rate, better sensing efficiency can be achieved with less number of sensing module by serializing the readout sequence further. On the contrary, much better resolution can be achieved with the longer sensing time beyond the maximum sample rate.

Generally, the frame rate requirement of the TSC is 120 Hz, hence near 83 samples can be taken within one frame of time with 10-μs sample time. The targeted TSP has 16 TX channels for mobile phone application. Without sensing module multiplexing, 16 sequences of readout take places with each signal readout sequence is performed in a long time and less effectively. Therefore, the sensing module is multiplexed in 4-way so that 64 sequences of readout completes the whole scan over the TSP, and power-efficient touch sensing is achieved in with the multiplexed sensing module. Fig. 3.34 shows 6:2 multiplexing scheme of the sensing channels. The 6:2 multiplexing scheme provides connectivity to the touch-screen panels by selecting adjacent channels for fully-differential sensing channel operation. The multiplexing scheme operates in four phases, the front multiplexor selects half of the

touch-screen, and the rear multiplexor provides the additional 3:2 multiplexing for

the fully differential sensing scheme.
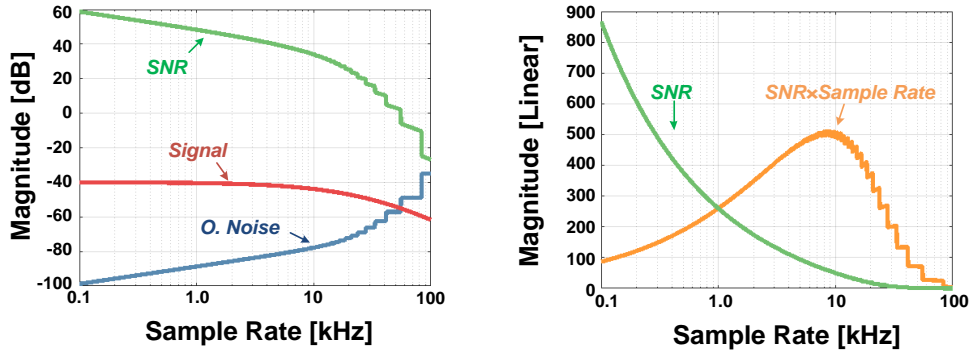
Fig. 3.33 Estimated SNR according to sensing rate.
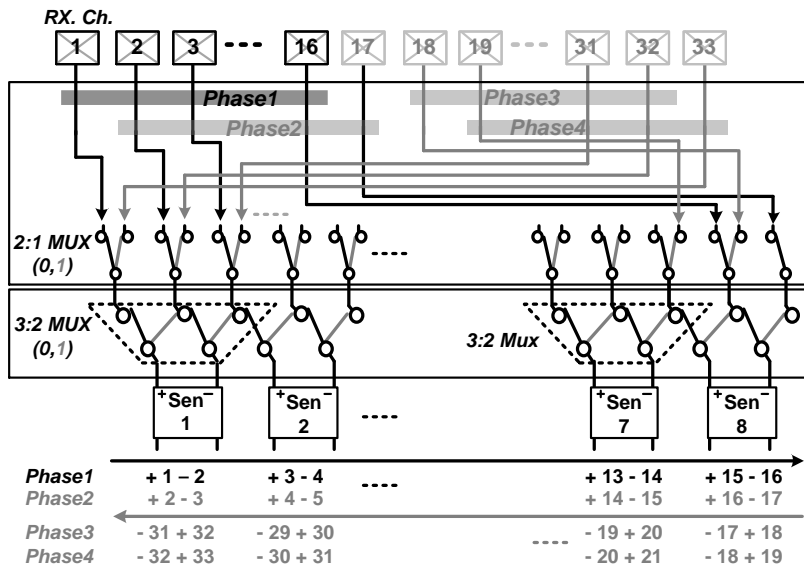
Fig. 3.34 Block diagram of 6:2 multiplexing.

3.5 Demodulation of Multi-Channel Driving and Noise Sampling

3.5.1 Multi-Channel Driving and its Demodulation

The demodulation of the multi-channel driving which is expressed as (2.11) is processed by performing a series of multiply-and-accumulate (MAC) operations using the sampled data and the multi-channel driving code during a frame. The MAC operation is performed in parallel according to the addresses of both TX and RX as illustrated in the block diagram of the demodulator shown in Fig. 3.35 and a selection of words replaces the -1 multiplication for each MAC cell.

Fig. 3.36 shows the block diagram and the timing diagram of the operation controller of the AFE. A phase-locked loop (PLL) is adopted to generate the system clock from the H-sync signal of the display driving IC. The *S_RST* is generated using a counter based clock divider, and the length of *S_RST* is configured for the synchronized operation. The *S_RST* is also utilized to distinguish each sample at both touch sensing module and the multi-channel driving demodulator. While *S_RST* is on, the fully differential stages and the ADC are reset to remove the sensed data before beginning the next driving sequence.
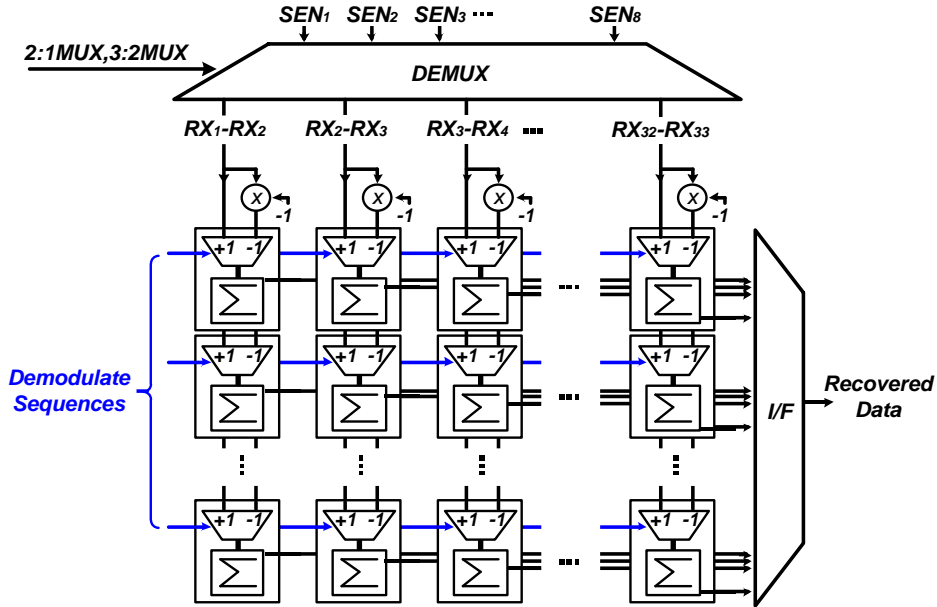
Fig. 3.35 Block diagram of the demodulator.

The address of the operation counter is increased at the rise edge of *S_RST* to generate each sequence of the multi-channel driving. The operation counter provides control signals for the multi-channel driving and the 6:2 multiplexing scheme in the sensing module. The multi-channel driving code is stored as a register file in the operation controller module, and one of the columns is used to encode the driving signals according to the control signals. The Φ-signals and θ-signals are generated and delivered to the stimuli generator according to the modulation code, and the polarity of the V_{STM} at Ch. 1 and 2 for an example are altered as a different address of the code is driven as shown in Fig. 3.36(b).

(a)

(b)
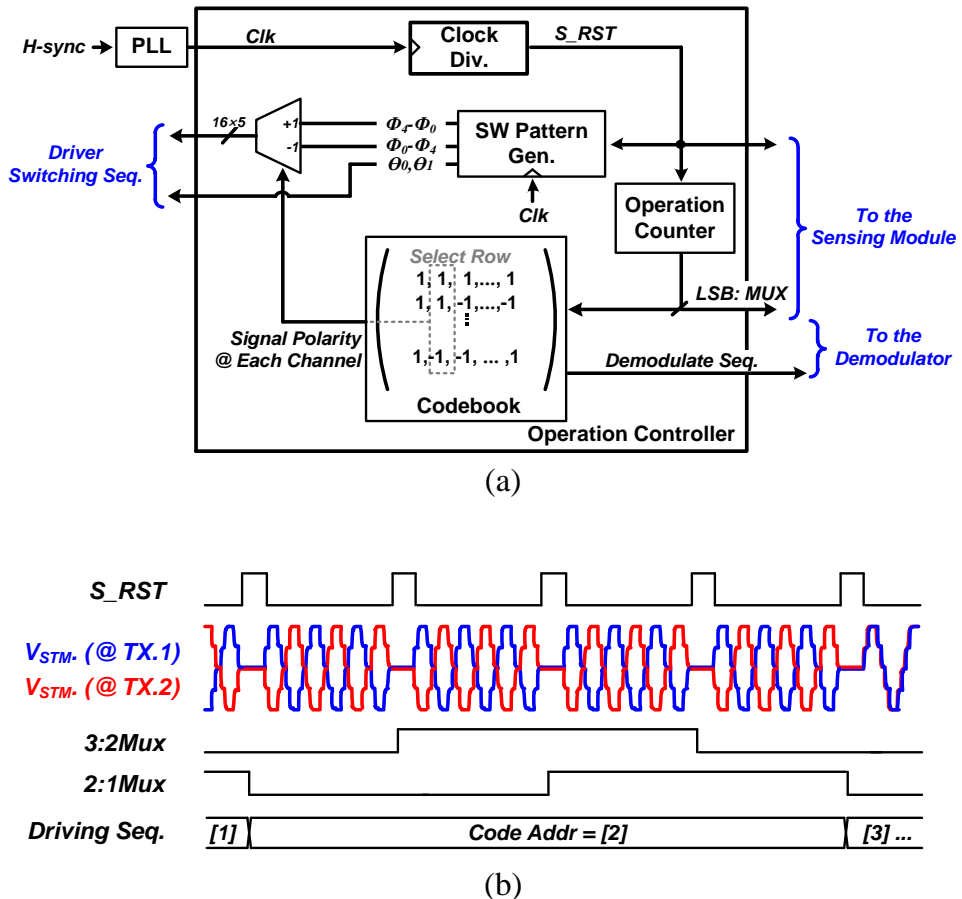
Fig. 3.36 (a) Block diagram of the operation controller and (b) its timing diagram.

3.5.2 Noise Sampling – Embedded

Multi-Channel Driving

Among the noise and interference sources, the mutual-capacitance data is mainly disturbed by the display operation. As mentioned in previous chapter, the display lines are driven row-by-row, thus the display interference is not random since several lines are required to indicate certain object. Moreover, the image which is displayed on the screen also is not randomly chosen. Therefore, the display driven interference is correlative, hence a noise sampling method [3.32] which is illustrated in Fig. 3.37 can reduce the interference. However, the need of extra sampling period of the correlated noise sampling technique makes less sample per time allocated.
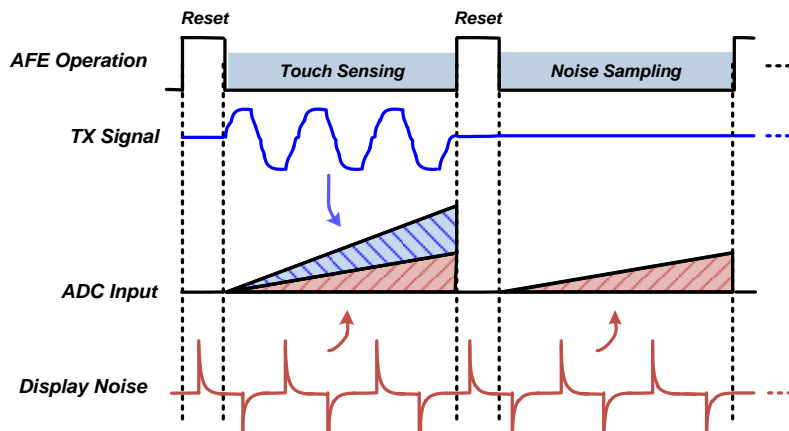
Fig. 3.37 Illustration of noise sampling method.

So far, the mutual capacitance on each node of touch-screen is modulated in an orthogonal code, and the demodulation is performed via the MAC of sensing data with the code. The demodulation of signal is expressed as (2.8) which includes the noise interference also processed with the MAC. The multi-channel driving and its demodulation with the correlated noise sampling technique is expressed as (2.6) and (2.8) with the modulation code embedding rows which indicate the noise sampling periods. The noise sampling rows are treated as zero-rows during the signal generation, and the rows are treated as -1 rows. As a result of noise sampling, the column-sum of the demodulation code becomes zero for every column. The MAC production is performed by column-by-column during the demodulation, hence noise interference is cancelled from the zero-average summation.

Moreover, the noise sampling need not be performed after every signal sampled to make zero column-average of the modulation code embedding noise sampling periods. Only $\sqrt{N}$ noise sampling periods is required for a $N \times N$ HM, since the column/row-average of a HM cannot be less than $\sqrt{N}$ for a $N \times N$ HM (See Appendix B.). In this design, 16×16 HM is used, hence four $(=\sqrt{16})$ noise sampling periods are taken. The implied code in the noise sampling period would be not only -1 but also -2, -4, and *etc.*, but only -1 noise sampling is applied here. During the noise sampling period, the signal generator stays at Φ_2 not generating stimuli and the corresponding MAC is performed treating the code of the noise sampling period as -1 to remove the row-average of the modulation code. This splits the multi-channel driving sequences and its demodulating codes into H^D and H^R respectively, and (2.6) and (2.8) are revised as (3.11) and (3.12).
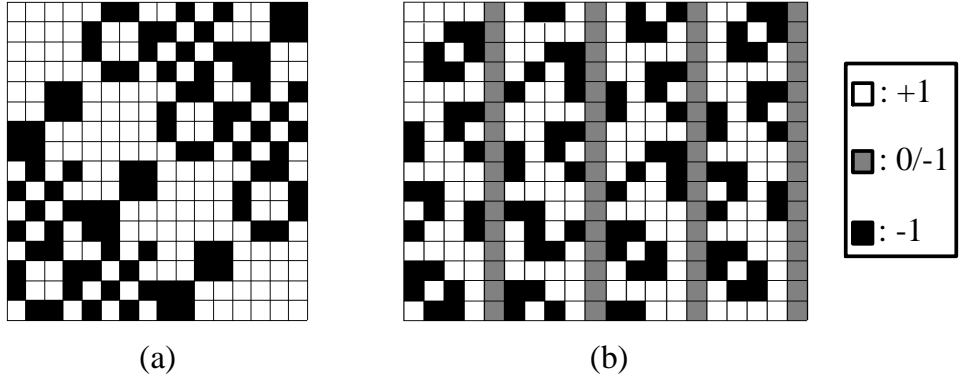
Fig. 3.38 Representation of multi-channel driving codes.

(a) 16×16 modified BH and (b) noise sampling embedded BH.

$$RX = V_{STM} \cdot \left((H^D)^T \times C \right) \quad (3.11)$$

$$D_{i,j} = \sum_{k=1}^{N_{TX}+\sqrt{N_{TX}}} (H^R)_{i,k} \times S_{k,j} = V_{STM} \cdot A \cdot N_{TX} \cdot C_{i,j} + \sum_{k=1}^{N_{TX}+\sqrt{N_{TX}}} (H^R)_{i,k} \cdot n_{k,j} \quad (3.12)$$

Fig. 3.38(b) shows the noise sampling periods embedded HM, the matrix includes noise sampling periods for its 5th, 10th, 15th, and 20th columns which are indicated as gray cells, and they are treated as 0 driver code, H^D and -1 for the receiver code, H^R. The noise sampling embedded HM is further modified for more being blended with +1 and -1 in H^R to improve the correlation between samples of display interference. The blended is H^R found through repetitive explorations of changing order of column-by-column and flipping polarity of one column. Each trial applied on the modulation code does not alter the orthogonality of the matrix. On top of the code rearrangement, the timing synchronization between the display driving and the touch readout is accomplished as shown in Fig. 3.39 by employing the PLL that generates the system clock from the display H-sync signal. Duration of reset periods between

each sample is set to match overall periods of each sequence to be multiples of the divider ratio of the PLL. Display driving operation is synchronized with the AFE operation, therefore the correlation of display interference is much increased.

Through the noise sampling, the signal flow diagram shown in Fig. 3.40 illustrates the overall operation of the TSC. The stimulation generator stays at the noise sampling periods, thus the mutual-capacitance of TSP is driven with the orthogonal driving code, H^D. The demodulation of the multi-channel driving is processed with the noise sampling embedded code, H^R, which is an unbiased, hence external interferences are cancelled out while the MAC is processed.
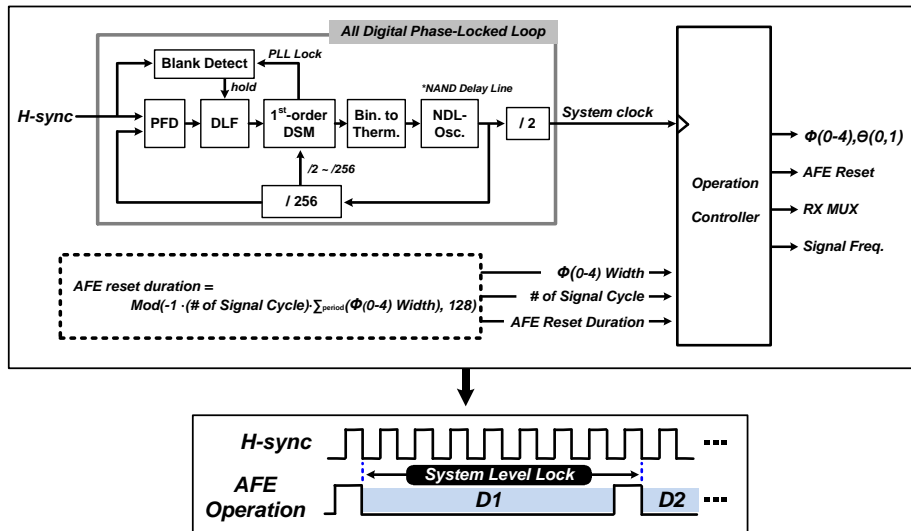
Fig. 3.39 Configurations on system level locking.
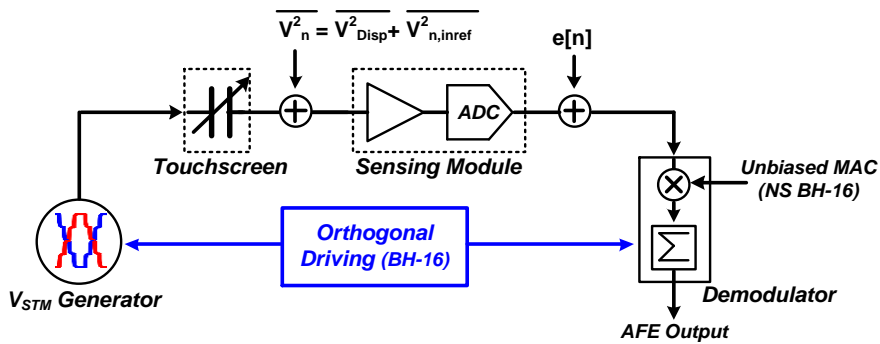
Fig. 3.40 Overall signal flow diagram.

3.6 Experimental Results

3.6.1 Measurement Environment

The AFE was tested with a commercial 5.8-inch WQHD+ (display resolution of 1440×2960 pixels) active-matrix OLED panel with a 16×33 on-cell touch-screen. The measurement environment is shown in Fig. 3.41; the evaluation board supports the display driver that generates the interference from the display panel while displaying test images on the screen. A single 100-nF capacitor was used as the energy-storing capacitor.
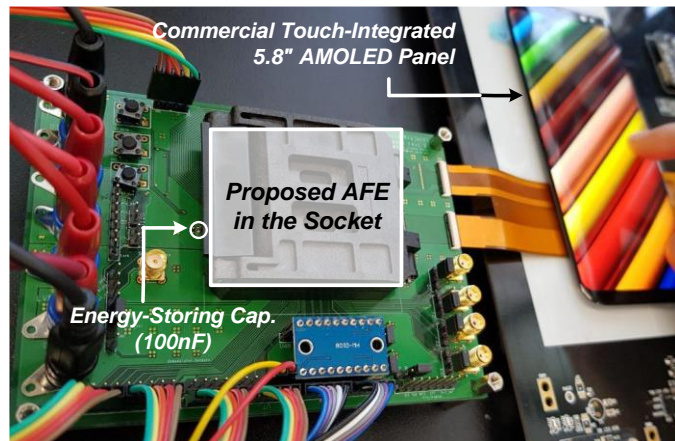
Fig. 3.41 Measurement environment.

3.6.2 Fabricated AFE

The AFE was fabricated in 180-nm CMOS process. The photomicrograph of the AFE is shown in Fig. 3.42. The area used for the mutual-capacitance detection are labelled accordingly and occupy an active area of 7.1 mm^2 in total. Each channel of the signal sensing module is further enlarged to highlight its structure and its area occupant of each block; the BPF and the LPF occupies large IC area among the signal sensing module. At the bottom domain, the digital modules such as PLL, I^{2}C, operation controller and multi-channel driving demodulator are implemented.
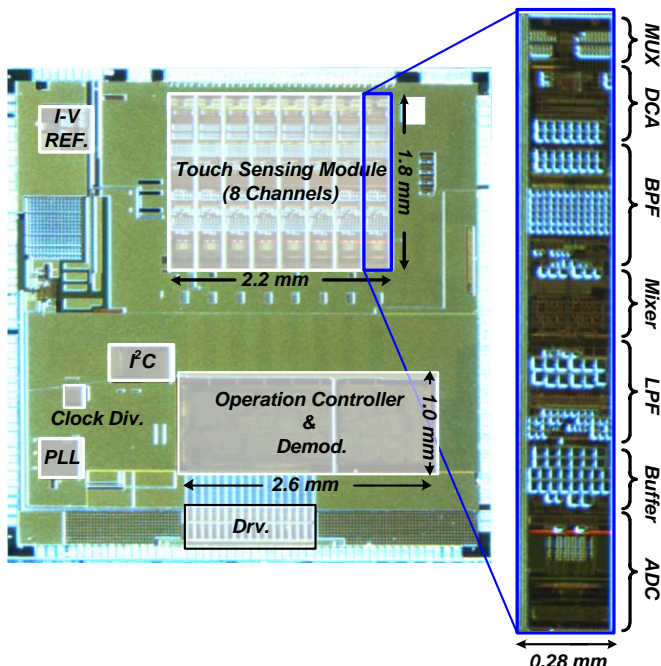
Fig. 3.42 Photomicrograph of the AFE.

3.6.3 Stimuli Generation

Fig. 3.43 shows the measured waveforms of the proposed stimuli generation. Fig. 3.43(a) shows initial voltage generation across the energy-storing capacitor. As the signal generator operates, energy is stored as the voltage across the plus node of capacitor (*Cap.p*) and the minus node (*Cap.m*) while the intermediate voltage levels of the stair-case waveform are generated. The voltage across the capacitor is fully generated within 200 ms. Fig. 3.43(b) shows the generated stimuli at two TX channels of the touch-screen. Each signal sample is distinguished by the AFE reset signal, and as the multi-driving is applied, the polarity of the signals is altered.
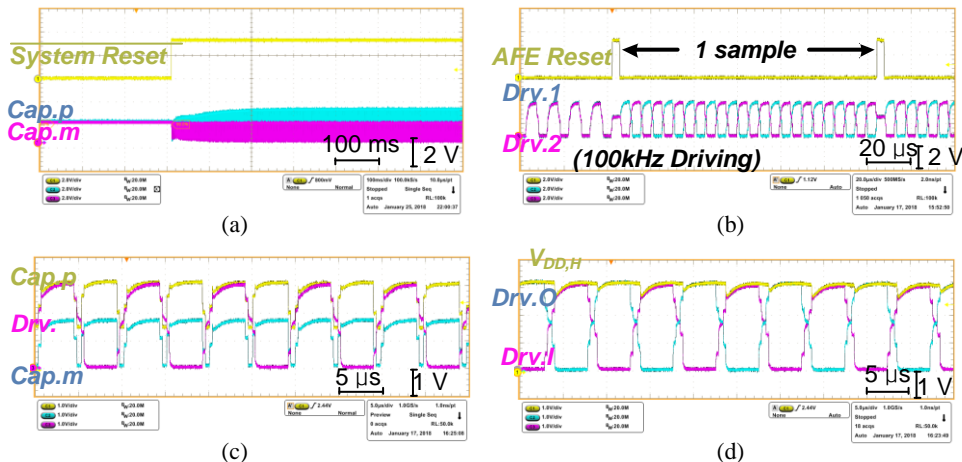
Fig. 3.43 Measured waveforms of stimuli signal.

Fig. 3.43(c) shows the enlarged stimuli signal along with the voltage levels of the energy-storing capacitor. Fig. 3.43(d) shows both in-phase and out-phase stimuli signal with the generated $V_{DD,H}$ level. Only the 1.8-V supply is connected to the Φ_2 switches, and the signal amplitude of approximately 3.3 V is obtained from the voltage converting scheme.

3.6.4 Capacitance Data

Signal samples are collected and recovered through the multi-channel driving demodulator, and the recovered mutual-capacitance image from the AFE is shown in Fig. 3.44. Three objects are placed while taking the mutual-capacitance image, hence the image demonstrates multi-touch and 1-mm diameter stylus detecting capability through the proposed signal generation scheme over the touch-integrated display module.
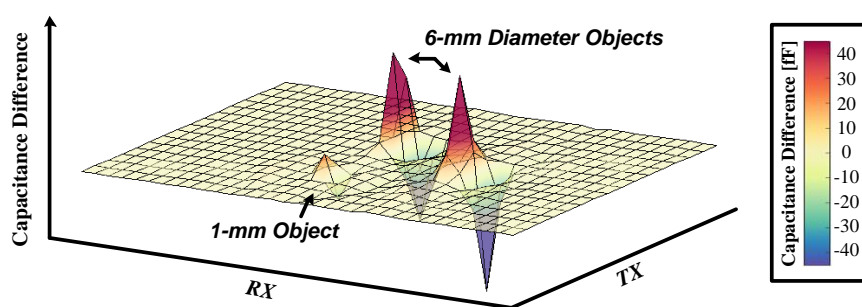
Fig. 3.44 Mutual-capacitance map.

3.6.5 Trade-Off between SNR and Power

The signal generator was tested with various configurations, and the trade-off between SNR and power consumption is summarized as presented in Fig. 3.45. Four stimuli generation modes are measured, for both 100-kHz and 200-kHz signal generation, and with the externally supplied $V_{DD,H}$ and internally generated $V_{DD,H}$ level. With externally supplied $V_{DD,H}$ level, SNR and the power consumption show trends as the intermediate switching time is increased. As analyzed, with the extended switching time, the more energy recycling can be performed, but less frequency component of the signal is acquired. Each point of the signal generation with external $V_{DD,H}$ supply was measured as extending intermediate switching time, and the graph shows sufficiently reduced energy compared to the pulse wave generation.
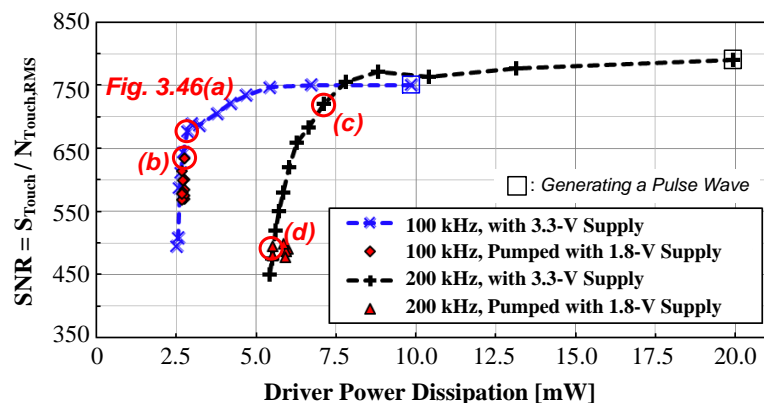
Fig. 3.45 SNR versus power dissipation on signal generator.

The most energy efficient configuration is highlighted in Fig. 3.45, and the actual

signal generation at the configuration is shown in Fig. 3.46. The dots in the Fig. 3.45

indicates the signal generation efficiency of the internally generated $V_{DD,H}$ mode.

The voltage pump scheme were adopted to generate 2-times higher voltage from the

voltage source, 1.8-V $V_{DD,L}$. However, the pumped voltage level could not reach to

the level as shown in Fig. 3.46(c) and (d) since the energy stored in the capacitor is

dissipated as the stair-case waveform being generated. The capacitor is not able to

hold voltage worth $V_{DD,L}$ across the nodes as it is charged with the $V_{DD,L}$-level sup-

ply. As shown in the timing diagram in Fig. 3.46(c), the capacitor is charged when

θ_0-switch are activated. As a result, more energy is stored in the capacitor with

longer Φ_2, thus, the higher amplitude of signal is achieved.
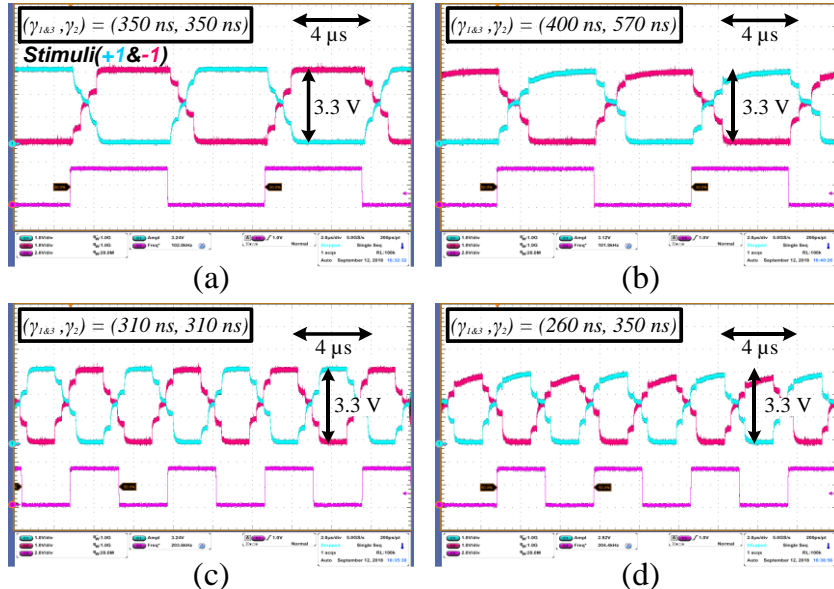
Fig. 3.46 Measured waveforms of optimal stimuli generation.
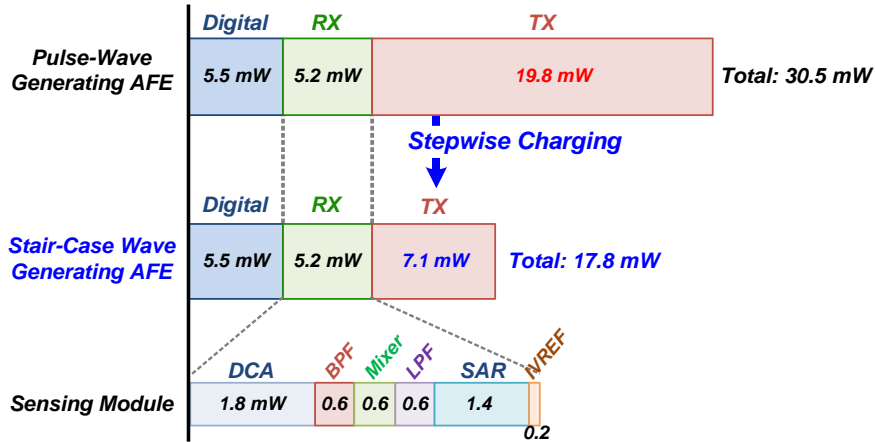
Fig. 3.47 Power breakdown of the AFE.

Power breakdown of the AFE is shown in Fig. 3.47. The whole touch sensing AFE dissipates 17.8 mW of power. Through the stepwise charging and discharging, the power dissipation on generating 200-kHz stimuli becomes 7.1 mW which would have been 19.8 mW alone for the signal generation. Digital modules such as PLL, I^{2}C, operation controller, and demodulator dissipates 5.5 mW in total, and the signal sensing module dissipates 5.2 mW. Further, power breakdown of the signal sensing module is presented, the DCA located at the front of the sensing module dissipate the most.

3.6.6 Trade-Off between SNR and Frame-Rate

The trade-off between the scan rate and capacitance resolution is verified with the measurement result shown in Fig. 3.48. The resulting capacitance resolution is measured with various sample time. Each sample time is represented as the over-sample ratio (OSR) of the ADC. At OSR of 51, 120-fps frame-rate and 66-aF capacitance resolution is achieved. However, near OSR of 30, the improvement of SNR is saturated with 210-fps frame rate.
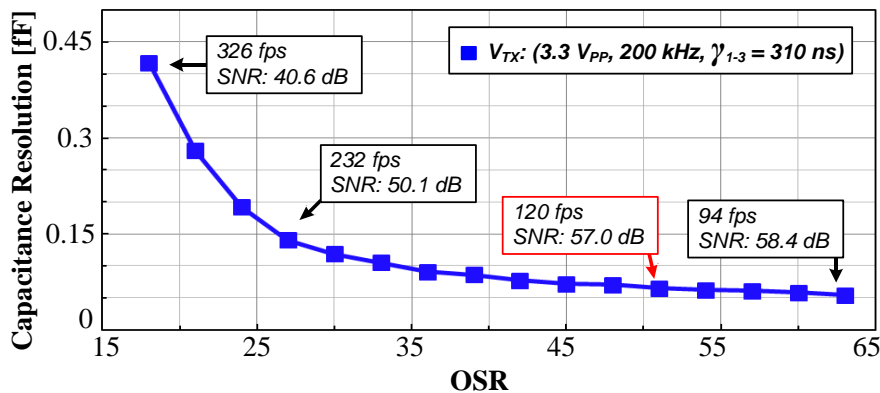
Fig. 3.48 Capacitance resolution versus frame-rate of AFE and OSR.

3.6.7 Effect of Noise Sampling

Measured nodal data under the worst-case interference of the display are listed in Fig. 3.49. The sensing module can be disturbed severely by the OLED, but the effect of the display interference has a specific frequency tone where the odd-harmonics of H-sync harmonic appears. The in-band noise is cancelled through the MAC process with zero-biased NS BH-16. Therefore, the correlated sampling method was able to reduce the interference by 12.0 dB.

Moreover, the PSD of the capacitance error through 2^{14} samples of data is shown in Fig. 3.50. The correlated noise sampling method decreases the capacitance error PSD in low frequency. The noise spectrum of 60 Hz was also removed as the same image were displayed during the measurement.
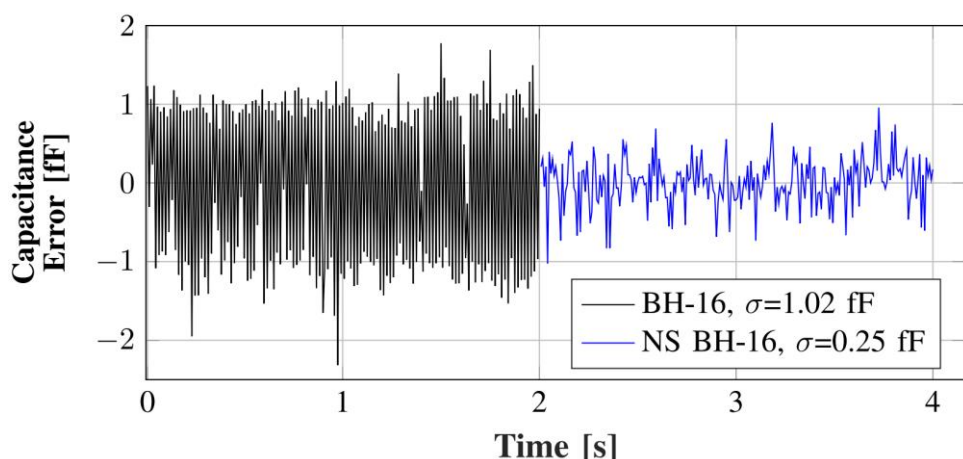
Fig. 3.49 Measured capacitance error under the worst-case display interference.
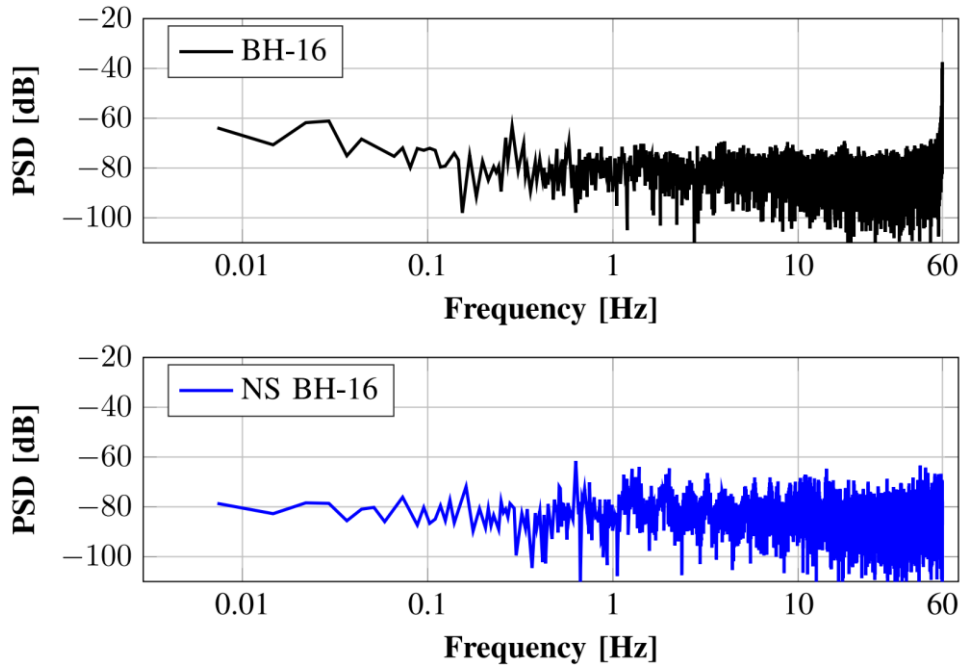
Fig. 3.50 PSD of the capacitance data while displaying the worst-case image.

3.6.8 Comparison with Other Works

The performance of the proposed AFE and the comparison with other capacitive touch sensor designs based on a mesh-metal-type TSP are shown in Table 3.1. The proposed AFE offers the lowest power consumption among the works. The AFE achieved the comparable energy-efficiency FOM of the touch sensors. Owing to the adiabatic signal generator, the increase of the power consumption will be smaller than other works even if the load capacitance of the TSP is increased to 1 nF per channel. Therefore, less degraded of FoM is expected.

Table 3.1 Performance Summary and Comparison with the other Works

		This Work	[3]	[12]	[6]	[20]	[21]
Application		**Mobile Phone**	Mobile Phone	Mobile Phone	TV	TV	TV
Touch Screen	Material	**Metal Mesh**					
	Number of Channels	**Tx: 16 Rx: 33**	Tx: 28 Rx: 16	Tx: 32 Rx: 18	Tx: 78 Rx: 138	Tx: 169 Rx: 97	Tx: 70 Rx: 120
Incorporated Display		**5.8-inch OLED** (1440×2960)	5-inch LCD (1080×1920)	5.7-inch OLED (1440×2560)	70-inch OLED (1080×1920)	65-inch LCD	46-inch
Process		**180-nm CMOS**	90-nm CMOS	180-nm CMOS	180-nm CMOS	350-nm BCD	350-nm BCD
SNR		**57.0 dB**	60 dB	51.5 dB	56.6 dB	43.5 dB	45.8 dB
Frame Rate		**120 Hz**	120 Hz	120 Hz	240 Hz	120 Hz	120 Hz
Supply		**TX: 1.8/3.3 V RX: 1.8 V**	TX: 12 V RX: 1.2, 3.3 V	TX: 3.3 V RX: 1.8 V	TX: 3.3 V RX: 1.8 V	TX: 12 V RX: 3.3 V	TX: 18 V RX: 3.3 V
Power Consumption		**17.8 mW (TX+RX+Dig= 7.1+5.2+5.5)**	24.6 mW (Analog+Dig= 10.2+14.4)	23.9 mW (TX+RX+Dig= 6.5+7.1+10.3)	559.9 mW	76 mW (TX+RX+etc.= 28.1+34.2+13.7)	180.5 mW
FoM [nJ/step]		**0.35**	0.23	0.79	0.39	0.26	1.12
FoM | C_L=0.01 nF [nJ/step]		**0.15**	0.23 [a]	0.49	0.39 [a]	0.15	1.12 [a]
FoM | C_L=1.0 nF [nJ/step]		**0.48**	0.88 [a]	1.93	0.54 [a]	0.73	4.15 [a]

$$\text{FoM} = \text{Power}_{TX,RX} / (2^{(SNR-1.76)/6.02} \cdot \text{\# of node} \cdot \text{frame rate})$$

a): Estimated (TX power portion is not shown in the paper).

Chapter 4

Calibration-Free, Low Power Self-Capacitance Readout Sensor

4.1 Overview

A touch-object such as a finger is electrically coupled to the TSP, and the TSC finds out the location of touch input by sensing either of self-or mutual-capacitance of the TSP. As previously described, the mutual-capacitance sensing method exhibits high precision on signal detection because the mutual-capacitance of TSP is amplitude-modulated with a dedicated TX frequency which can be chosen avoiding the significant environmental and touch-injection noise band. On the other hand, the self-capacitance readout can cover a wider part of TSP at once, hence requires fewer steps to scan the entire TSP. Moreover, since the transition of self-capacitance is generally larger mutual-capacitance transition of the bar-type TSP, the existence of touch-object can be detected with less sensitive sensing circuits. From these reasons,

the self-capacitance readout method is more capable of low power and coarse detecting mode of the TSC. Therefore, with the self-capacitance readout capability, the energy-efficiency of TSC can be much improved since the TSC does not need to sense mutual-capacitance of TSP when no touch-input is engaged.

The self-capacitance readout AFE detects additional capacitive coupling between the touch-object and the touch-screen channel. Fig. 4.1 shows the existing methods for sensing capacitance. Capacitance can be measured by detecting the voltage slope while continuously charging/discharging the capacitor node as shown in Fig. 4.1(a). Otherwise, the LC resonance phenomenon can be utilized to measure the capacitance; the resonance frequency differs as the capacitance varies as shown in Fig. 4.1(b). However, due to the much-increased self- capacitance of the touch-integrated TSP structures, the newly added capacitance to the touch-object occupies very small part (< 0.5 %) of overall capacitance, thus it is very hard to accurately detect the additional capacitance by measuring the entire self-capacitance of the TSP. Instead, the charge-sharing based method which detects the capacitance difference has been proposed [4.5] - [4.8]. Representatively, the charge-share based capacitance difference measurement is shown in Fig. 4.1(c). However, the capacitance offset between channels due to different route paths and circuit mismatches limit the dynamic range of the differential sensing scheme, thus a calibration step is necessary for precise touch object detection.
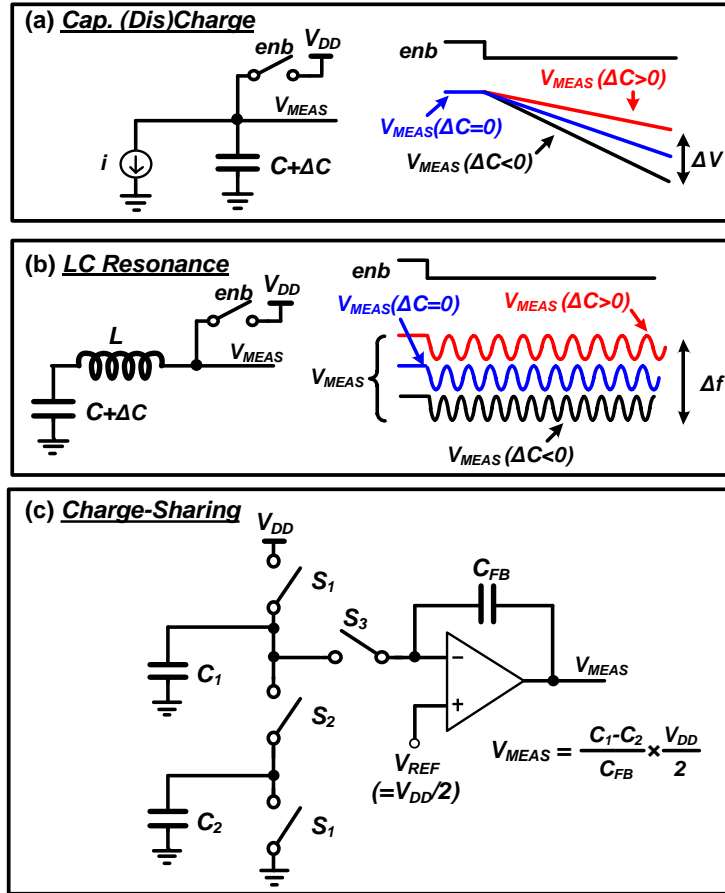
Fig. 4.1 Illustrations of existing capacitance readout methods.

(a) Constant-discharging method [4.1][4.2], (b) resonance based capacitance measurement [4.3][4.4], and (c) charge-sharing based readout [4.5] - [4.8].

4.2 Operation Principle

To address the problems, a low power self-capacitance sensing method is newly proposed which detect only the capacitance variance from the touch-input. By sensing the capacitance transition, the existence of touch-input and its location can be detected, so it can be utilized as an assistant operation mode of the touch sensing AFE.

The basic principle of the proposed sensing method is illustrated in Fig. 4.2. When a capacitance is newly added at a node while keeping its voltage level, a certain amount of electric charge is additionally required. The amount of charge is used for the detection. The proposed method utilizes the current mirror scheme while keeping the voltage level of the touch-screen channel at the reference voltage level (V_{REF}) while the current mirror (CM) circuit copies the amount of current which are used for the voltage regulation through the negative feedback. When the capacitance (ΔC) is newly added because of the touch object, electric charge of ($\Delta C \times V_{REF}$) need
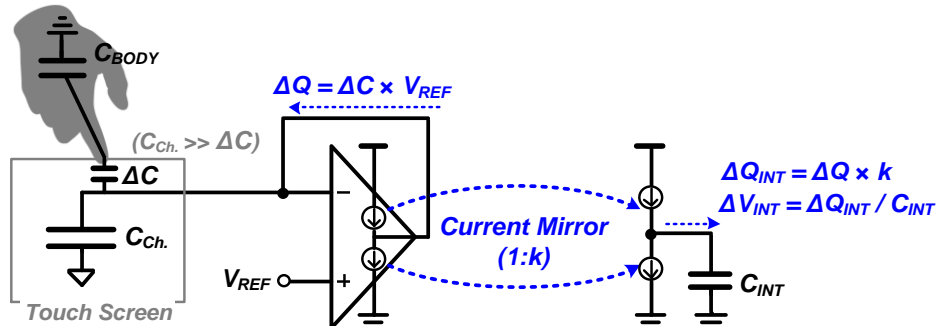
Fig. 4.2 Operation principle of the sensing method.

to be newly provided from the voltage-level regulation (VLR) circuit. The amount of newly supplied charge is current-mirrored and stored at the separated integration capacitor (C_{INT}).

The touch-screen channels are multiplexed so that only one current mirroring (CM)-VLR cell can scan the entire TSP. Therefore, a multiplexing on the touch-screen channels is applied. Self-capacitance readout at each channel consists of several steps. Among the steps, the essential parts of the sensing method are illustrated in Fig. 4.3 from the reset state to the acquisition of different voltage result according to the touch-object. Fig. 4.3(a) shows the reset-state of the AFE. As the beginning of each readout sequence, two adjacent touch-screen channels among the channels are

(a)   (b)
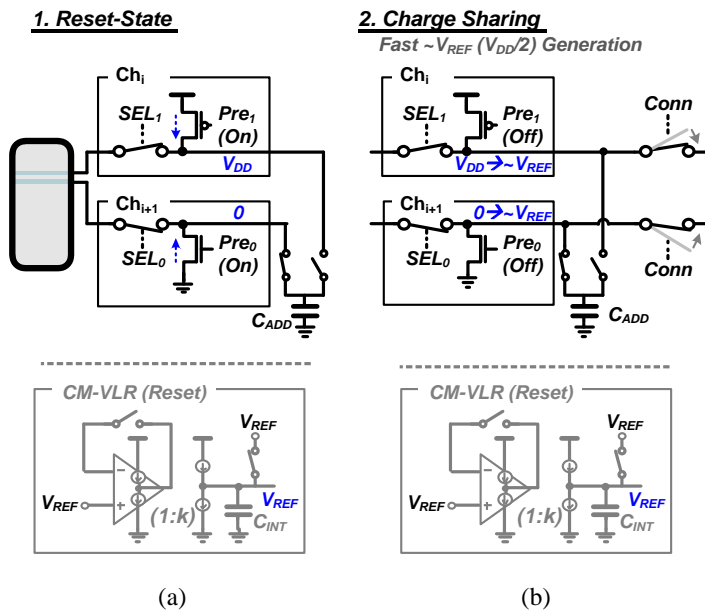
Fig. 4.3 Steps of the self-capacitance sensing method: Part 1. (a): Reset-state and (b): coarse generation of V_{REF} level to the selected touch-screen channels.
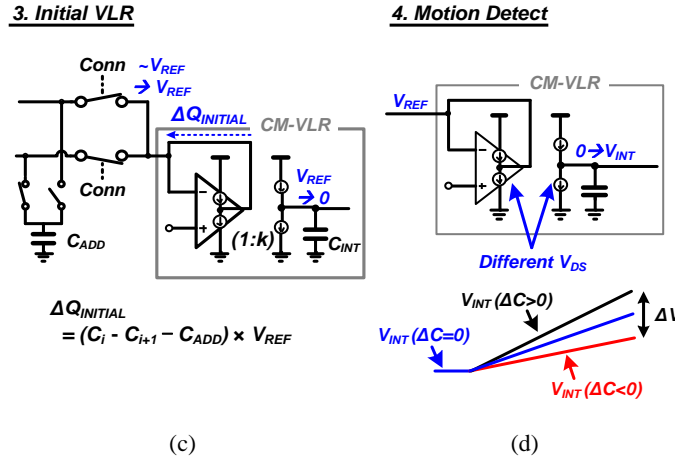
Fig. 4.3 Steps of the self-capacitance sensing method: Part 2. (c): Initial CM-VLR

operation and (d): generation of V_{INT} level according to varied capacitance.

selected and pre-charged/discharged respectively. The CM-VLR cell is reset as the

feedback loop is disconnected, and C_{INT}-node is reset to V_{REF}. After the reset state,

the pre-charged/discharged touch-screen channels are connected to each other so

that the near $1/2V_{DD} = V_{REF}$ voltage is fast generated. C_i and C_{i+1} are the self-capaci-

tance of the selected touch-screen channels, and the voltage discrepancy between in-

itially generated voltage and V_{REF} is expressed as (4.1) which is proportional to the

capacitance difference.

$$\Delta V_{Initial} = \frac{C_i - C_{i+1}}{C_i + C_{i+1}} \times V_{REF}$$

(4.1)

After the voltage-level at the touch-screen channels is coarsely generated, initial

CM-VLR operation is done as shown in Fig.4.3(c). In this step, the voltage discrep-

ancy is compensated from the CM-VLR cell. Amount of charge, $(C_i - C_{i+1}) \times V_{REF}$ is

required for the initial VLR operation, and it is copied to the C_{INT}-node. As a result,

the capacitance offset C_i - C_{i+1} remains in the V_{INT}-level and limits dynamic range of the detection.

To mitigate the effect of capacitance offset between touch-screen channels, the additional capacitor (C_{ADD}) is added to further diversify the capacitance difference. In the figure, C_{i+1} is assumed to be larger than C_i, and C_{ADD} is pre-discharged so that larger $\Delta V_{Initial}$ is generated owing to C_{ADD}. As a result, $C_{ADD} \times V_{REF}$ -amount of charge is more required for the initial VLR operation. Therefore, with a large-enough capacitor C_{ADD}, the current mirror stage becomes saturated since the VLR takes places regardless the state of the mirrored stage. For each scan, the initial voltage level is generated slightly higher or lower than the V_{REF} level, and the capacitance offset is neglected from the initial CM-VLR operation as V_{INT} is saturated regardless of the TSP capacitance offset. In this example, V_{INT} level is set to 0 in the initial CM-VLR operation, and the TSP capacitance offset (C_i - C_{i+1}) of the touch-screen channel is neglected. As shown in Fig. 4.3, C_{ADD} can be added either on the pre-charged channel or pre-discharged channel. In order to make the current mirror stage to become saturated from the initial VLR operation, the required capacitance value of C_{ADD} can be expressed to meet one of following conditions:

$$C_{ADD} > \frac{C_{INT}}{k} - \min_{i}(C_i - C_{i+1}), \quad \text{(4.2-1)}$$

$$C_{ADD} > \frac{C_{INT}}{k} - \min_{i}(C_{i+1} - C_i). \quad \text{(4.2-2)}$$

While the voltage level of the capacitive node of the touch-screen channels remains at V_{REF}, the V_{INT}-level is initially set to 0 (or V_{DD} according to the direction), so a different V_{DS} is occurred at the current mirror MOSFETs resulting a difference in

the mirrored current. As a result, the initial saturated state is slowly relaxed as illustrated as $V_{INT}(\Delta C=0)$ line in Fig. 4.3(d). As the capacitance coupling is newly engaged to the TSP and additional ΔC coupled to the channel, the amount of charge $\Delta C \times V_{REF}$ is additionally provided from the VLR operation and copied to V_{INT} node. Therefore, by measuring V_{INT}, the self-capacitance transition of TSP is detected. From the quick transition of self-capacitance, V_{INT} level is expected to be diversified in an instant according to the capacitance variance. However, in the real situation, such quick touch-input is not present, so that diversity of V_{INT} level is represented with different voltage slopes in Fig. 4.3(d). After the detection, the CM-VLR is reset and other touch-screen channels are selected in order to scan different location on the screen.

4.3 Circuit Implementation

4.3.1 Overall Architecture

The self-capacitance sensing circuit is utilized as the assistance operation for touch detection. Therefore, several modules described in Chapter 3 are reused. Fig. 4.4 represents the block diagram of AFE in self-capacitance sensing mode. Cells represented in gray is inactivated for the self-capacitance sensing mode. The pre-charging/discharging switches are placed at each channel. A pair of touch-screen channels are selected and connected to the CM-VLR cell after the charge redistribution. The touch signal is delivered to the noise filter stages which is also used for the mutual-
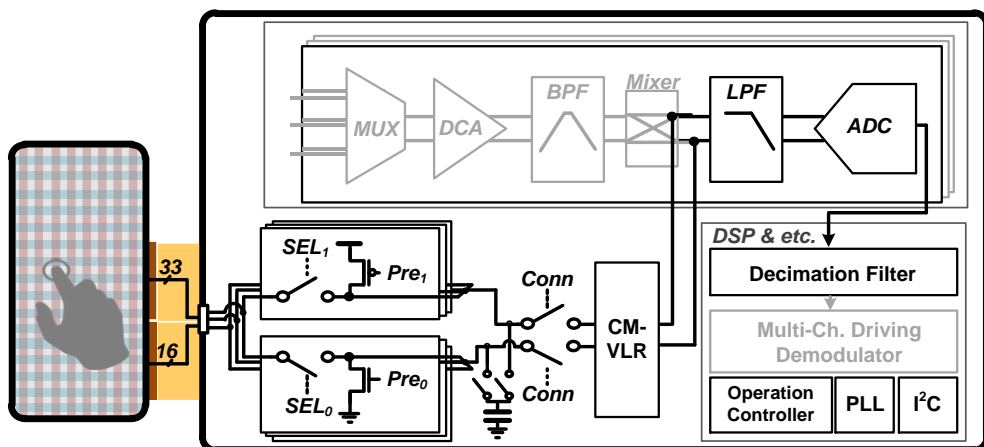
Fig. 4.4 System architecture of AFE in self-capacitance sensing mode.

capacitance readout. The clock signal is generated by the ring oscillator of the PLL which is not activated in the self-capacitance readout mode.

Fig. 4.5(a) shows the separated system architecture for the self-capacitance readout. The signal path after the CM-VLR is represented in Fig. 4.5(b). V_{INT} -V_{REF} is treated as the detected signal and passes through the single-to-differential (S2D) converter, V_{INT} is buffered along with V_{REF}, and V_{INT} -V_{REF} enters to the fully-differential LPF. Then the signal is converted into the digit signal. An oversampling ADC is adopted, but the ADC samples the signal slowly to reduce power consumption in the self-capacitance sensing mode. Finally, the CIC filter decimates the oversampled data, and the result becomes the output of the AFE.
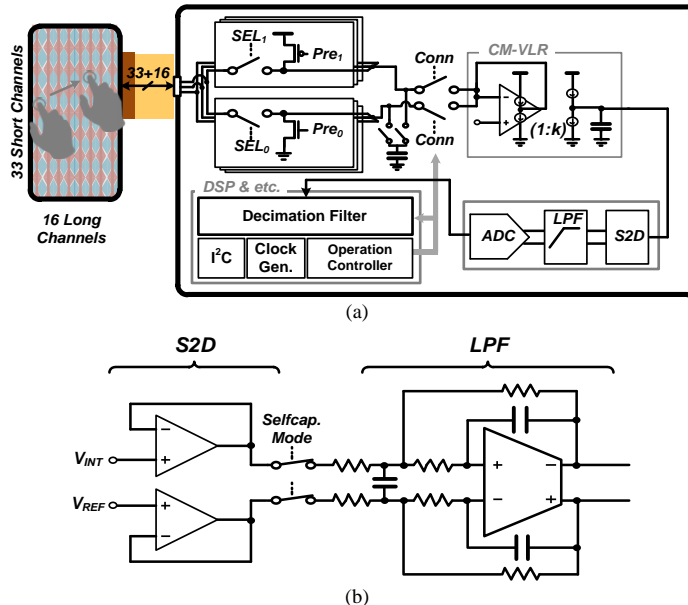
Fig. 4.5 (a): System architecture of self-capacitance readout AFE and

(b): signal path after the CM-VLR cell.

4.3.2 Current-Mirroring Voltage-Level Regulation

The circuit-level implementation of the CM-VLR cell is shown in Fig. 4.6. Basically, the circuit is a voltage regulator which keeps voltage-level of the sensing channel at V_{REF}, and the amount of current used to keep the voltage level is copied to C_{INT}. The CM-VLR cell operates in two phases, and the timing diagram of the CM-VLR is shown in Fig.4.7. The CM-VLR cell becomes the reset-state with $\Phi_1=1$ and $\Phi_2=0$. Selected touch-screen channels are pre- charged/discharged while the feedback loop of the VLR is opened, and C_{INT} is reset to V_{REF}. Through the Φ_1-switches,
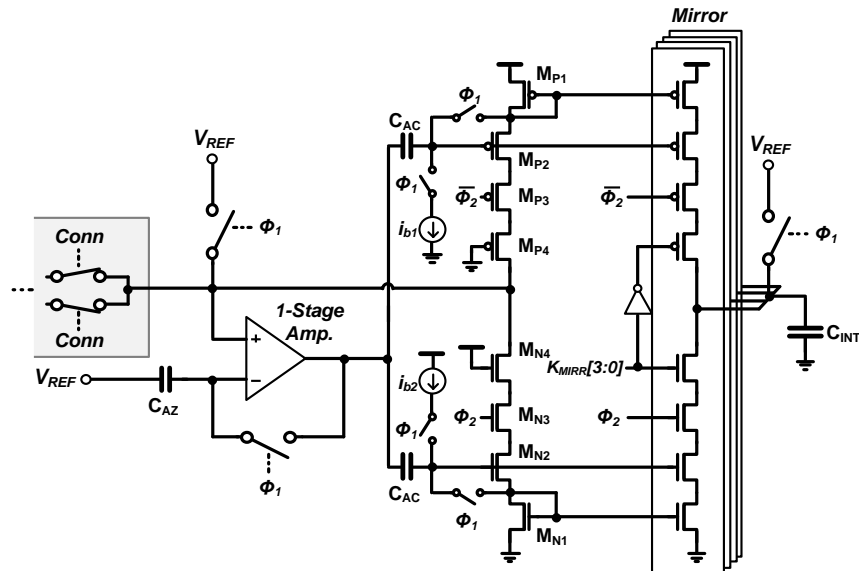
Fig. 4.6 Schematic diagram of the CM-VLR cell.
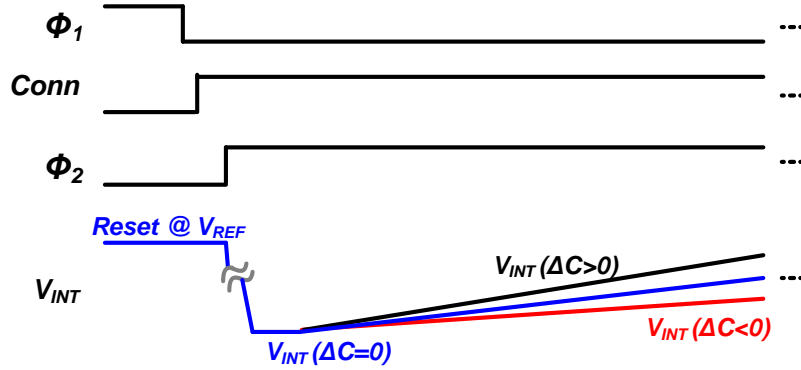
Fig. 4.7 Timing diagram of the CM-VLR cell.

current sources I_{b1} and I_{b2} are connected to M_{P1} and M_{N1} respectively, so voltage bias at the gate of M_{P2} and M_{N2} are set. I_{b1} and I_{b2} can be tuned for various VLR bandwidth and target report rate. The voltage error signal from the 1-stage amplifier is transmitted to M_{P2} and M_{N2} concurrently using the AC-coupling capacitors (C_{AC}). The voltage error signal transmission through C_{AC} allows more voltage headroom with separated bias points for the pull-up and pull-down devices. Voltage bias levels are kept by C_{AC} while the CM-VLR circuit is active. Moreover, auto-zeroing is applied to reduce the voltage discrepancy between the V_{REF} and the regulated sensing channel voltage due to the input-offset of the 1-stage amplifier. After the selected touch-screen channels and the CM-VLR circuit are reset, Φ_1 becomes 0 and the charge sharing connect signal (*Conn*) becomes 1. Initial V_{REF}-level at the selected touch-screen channels is coarsely generated from the charge sharing. Then, Φ_2 becomes 1 and the CM-VLR circuit is activated. The current mirror ratio (*k* in Fig. 4.3) is digitally controlled. M_{P4} and M_{N4} are placed for the matching.

4.4 Experimental Results

4.4.1 Fabricated AFE

The proposed AFE was fabricated in a 180-nm CMOS process. The AFE was tested with the 16×33 on-cell TSP which is also utilized for the mutual-capacitance sensing experiments. The photomicrograph of the AFE is shown in Fig. 4.8. The CM-VLR cell occupies 0.12-mm^2 of area. Blocks used for the mutual-capacitance readout are labelled as inactive in the photomicrograph.

Name	C_{AZ}	C_{AC}	C_{INT}	C_{ADD}
Size	1.8 pF	0.65 pF	3.1 pF	6.6 pF

<Capacitance Size>
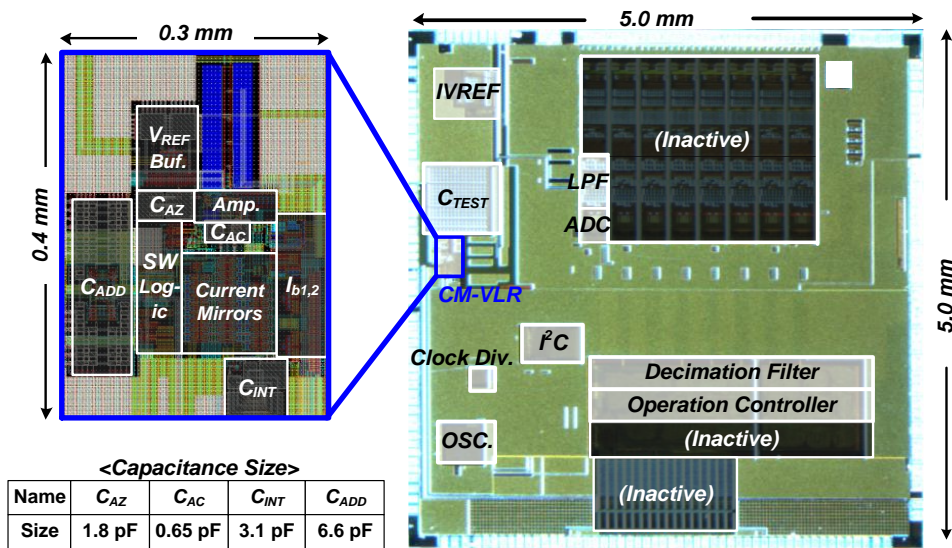
Fig. 4.8 Layout of the CM-VLR cell and photomicrograph of the proposed AFE.

4.4.2 Touch Object Detection

Target to the 16×33 TSP, the operation controller was designed to become able to specify 16 sensing locations. In self-capacitance sensing mode, the AFE can be configured to scan 3-different locations: 16 long channels, short channels (1 to 17), and (16 to 33). In this chapter, measurement results with 16 long channels are shown for intuitive interpretation of the result.

Fig. 4.9 shows measured $V_{INT, P}$ signal from the S2D without motion of the touch-object. Waveforms in Fig. 4.10 are measured with a touch-object being motionless on top of the TSP, and waveforms in Fig. 4.10 are also observed without a touch-object on the screen. The pulse-waves in blue indicates the frame rate of the readout.

Fig. 4.10 is measured while the touch-object is moving. The top-left figure shows the measured output while the object is moving to the left. $C_{Long,5,6}$ and $C_{Long6,7}$ are clearly detected increased as the object gets closer to the channel, and $C_{Long7,8}$, $C_{Long8,9}$, and $C_{Long9,10}$ are detected decreased. The top-right figure is measured while the touch-object is moving to the right, and the signal are measured in the opposite direction to the top-left figure. The bottom-left figure is measured while the touch-object is approaching the TSP. The increase of $C_{Long9,10}$, $C_{Long10,11}$, and $C_{Long11,12}$ is detected without other decreased capacitance detected. The bottom-right figure is measured while the touch-object is moving away from the TSP in the vertical direction, and the only decrease of capacitance is detected.
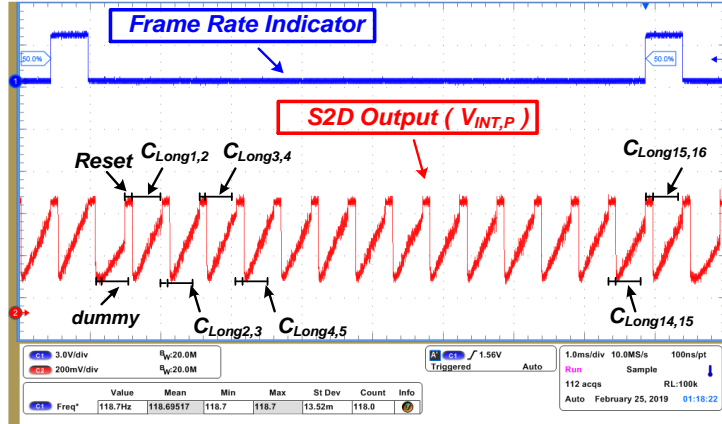
Fig. 4.9 Measured waveform of $V_{INT, P.}$
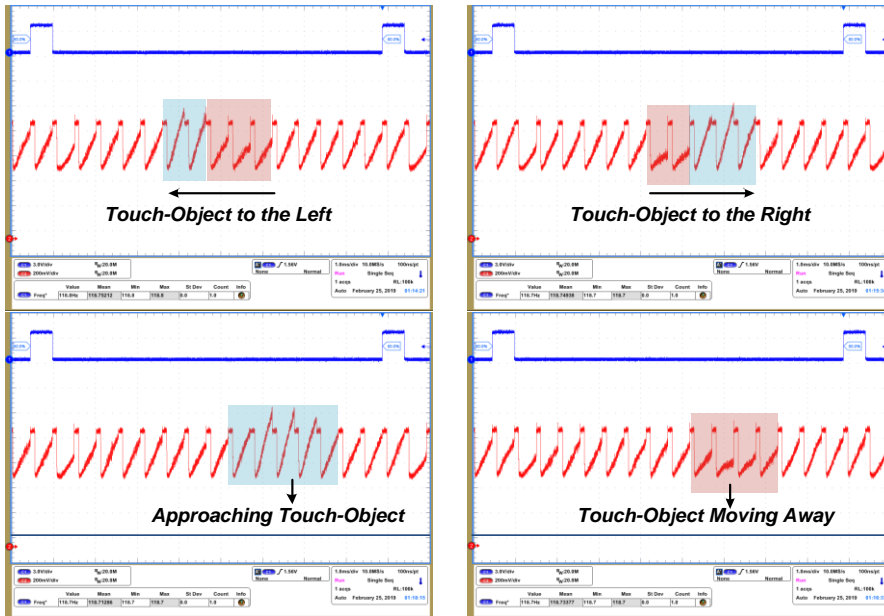
Fig. 4.10 Measured waveform of $V_{INT, P}$

with the touch-object moving toward various directions.

Fig. 4.11 shows the AFE output in several seconds with the touch-object motions in Fig. 4.10. Fig. 4.11(a) is measured while swiping the touch-object left-to-right, and Fig. 4.11(b) is measured while moving the object up-and-down. The touch-object is not moved between the movement. For the motion recognition, the SNR is defined as follows:

$$SNR = 20\log\frac{S_{INC.} - S_{DEC.}}{\sigma_{RMS}} = 20\log\frac{S_{INC.} - S_{DEC.}}{\sqrt{(S_{Normal} - S_{AVG})^2}} \qquad (4.3)$$

, where S_{Normal} and S_{AVG} are measured between the movement and the root-mean-square (RMS) error of the AFE output (σ_{RMS}) is measured as 22.3. The AFE achieves 32-dB SNR when the touch-object moves across the panel in approximately 0.7 second as in Fig. 4.11(a).
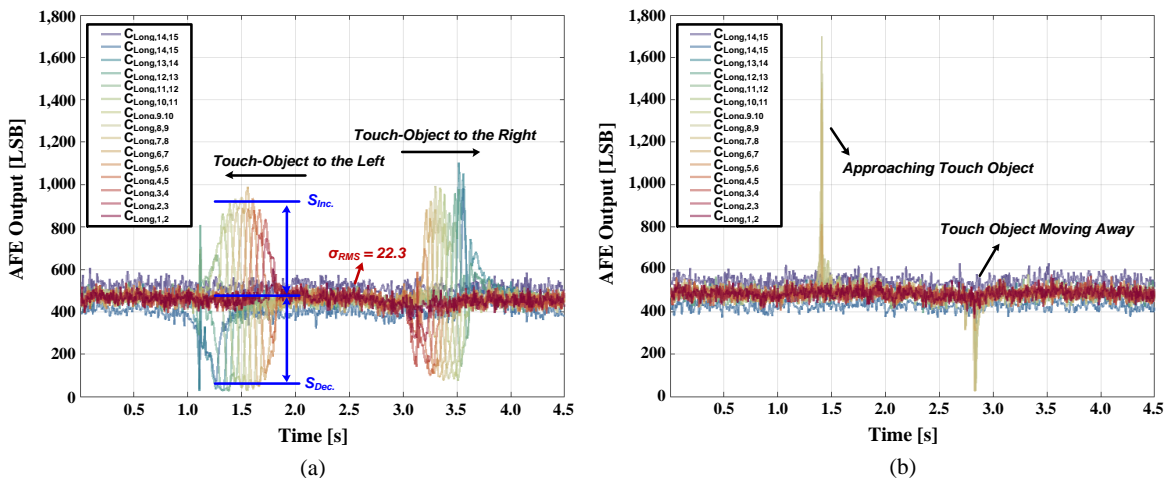
Fig. 4.11 Measured data from the self-capacitance sensing AFE while (a): swiping the touch object on the screen and (b): moving the object up-and-down.

Fig. 4.12 shows power dissipation sources of the AFE in self-capacitance detecting mode. The AFE dissipates 2.09-mW of power in total, and 0.54-mW of power is dissipated for the CM-VLR operation.
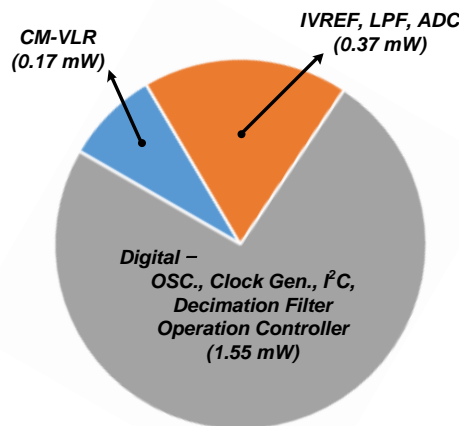
Fig. 4.12 Power breakdown of the AFE in self-capacitance sensing mode.

4.4.3 Comparison with Other Works

The performance of the proposed AFE and the comparison with other self-capacitance detecting methods in Table 4.1. The proposed AFE consumes the lowest power among the works. As the AFE can work with a single supply voltage, the proposed self-capacitance readout method can be easily added on the TSC for the low power and coarsely detect mode owing to not only the low power consumption but also the AFE does not require calibration steps for the sensing mode transposition.

Moreover, the CM-VLR cell requires neither a large IC area nor other external components to utilize.

Table 4.1 Performance Summary and Comparison

with the other self-capacitance sensors.

	This Work	ISSCC 2014 [4.3]	VLSI Symp. 2014 [4.7]	ISSCC 2015 [4.4]	VLSI Symp. 2017 [4.8]
Touch Screen Size [Channels]	**6.8 cm × 14.9 cm [16 (X) + 33 (Y)]**	40 cm × 40 cm [8 (X + Y)]	5-inch [16 (X) + 28 (Y)]	3.4-inch [16 (X) + 10 (Y)]	22 cm × 13.6 cm [55 (X) + 34 (Y)]
Process	**180-nm CMOS**	130-nm CMOS	90-nm CMOS	65-nm CMOS	180-nm BCD
SNR	**32 dB**	50 dB	53 dB	36 dB	39 dB
Frame Rate	**120 Hz**	240 Hz	120 Hz	120 Hz	240 Hz
Supply	**1.8 V**	1.2, 2.5 V	1.2, 3.3, 12 V	1 V	± 15 V
Power Consumption	**2.1 mW**	19 mW	24.6 mW	2.3 mW	16.3 mW
Required Area	**0.12 mm^2**	4.2 mm^2	N/A	2 mm^2	0.73 mm^2
Operation without External Component	**Yes**	No (Inductor)	Yes	Yes	Yes
Operation without Capacitance Calibration	**Yes**	No	No	No	No

Chapter 5

Conclusion

In this thesis, an energy-efficient touch sensing AFE for touch-screen integrated display panels is proposed. The adiabatic signal generation method is newly applied to generate a touch stimulating signal to reduce energy dissipation. Based on a charge recycling scheme implemented with switched-capacitor circuits, the stepwise charging method is analyzed to obtain the optimum design for generating the signal for the bandwidth-limited touch-screen panel. In addition, the overhead from the usage of external components is reduced via the proposed capacitor switching techniques, and multi-level voltages are implemented with only one capacitor. The touch sensing AFE employs fully differential noise filtering stages to reduce the highly coupled interference from the display, and the noise interference is further attenuated using the correlated sampling technique.

Moreover, the detection of touch-input with self-capacitance readout is proposed for the TSC as the low power operation mode. The existence of touch input is detected by sensing only the capacitance variation of TSP by the proposed CM-VLR method. The effect of capacitance offset is mitigated by the initial CM-VLR operation using an additional capacitor. Therefore, without calibration step, the AFE is

able to detects the existence and motions of touch-objects by sensing the transition self-capacitance. The proposed readout method can be easily added on the TSC for the low power and idle sensing mode owing to not only the low power consumption but also the AFE does not require calibration time for the sensing mode transposition. Moreover, the CM-VLR cell does not require a large IC area and other external components.

The proposed system was implemented in a 180-nm CMOS process. Tested with a commercial 5.8-inch WQHD+ active-matrix OLED panel with an integrated 16×33 touch-screen, the AFE achieves 57.0-dB SNR with 17.8 mW of power consumption in mutual-capacitance readout mode. Among the power dissipating sources, the signal generator dissipates 7.1 mW of power while a conventional signal generator would consume 19.8 mW. As coarse detection mode of the proposed AFE, the AFE achieves 32-dB SNR in 120-Hz report rate while dissipating 2.1 mW.

Appendix A

Performance of the Signal Generator

in General

This thesis mainly considered the touch-screen panel with bandwidth roughly around at 400 kHz. However, parasitic characteristics of touch-screen panel can be changed in either way with wider channel bandwidth owing to the improved connecting material between the touch-screen channels and IC, or less channel bandwidth due to more tightly placed integrated touch-screen channels and extremely narrow connection between the touch-screen channels and IC. Since the energy saving in the given time can be altered significantly as the bandwidth of the driving load is altered, an extra investigation on the performance of the stepwise charging and discharging scheme is performed. Moreover, a design method of the signal generator is proposed with the optimally placed switched capacitor.

In the thesis, an analysis on the attenuated charge recycling is described to estimate the energy reduction effect. In the consecutive switching, the parasitic resistance blocks the charge transactions and the voltage level cannot reach the final

voltage level within the limited switching time. The attenuated charge recycling occurs less with less parasitic resistor; hence more energy is recycled during the switching time, or less switching time is required to accomplish the same energy reduction. Therefore, more switching steps are available for the stepwise charging and discharging scheme with the touch-screen panel with smaller time-constant.

Energy efficiency on generating the stair-case waveform can be calculated from (3.7) and (3.8) in the same manner, and as an example, the signal generating efficiency with a 1-MHz bandwidth touch-screen is plotted in Fig. A.1. Compared to the graphs Fig. 3.11 or 3.12 which are drawn with the 400-kHz bandwidth touch-screen, the lines are located top and left and the energy-saving performance and the amount of frequency component tradeoff becomes much better for the low-power design. Therefore, higher $|f_{STM}|/E_{DRV}$ can be achieved and the desired operational scheme of signal generator is selected accordingly.
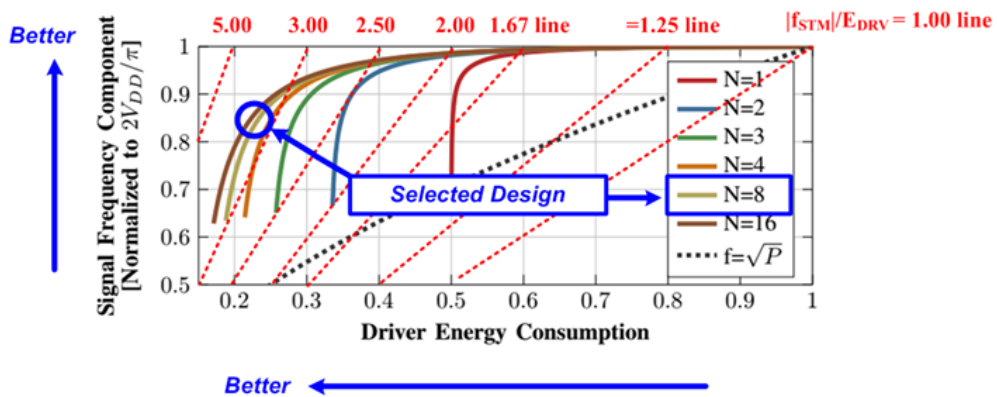
Fig. A.1 Effective signal amplitude versus the energy dissipation
with supplementary notes with 1-MHz bandwidth TSP.

However, the amount of capacitor is a crucial design factor considering the overall form-factor of the touch sensor system. This factor is not constrained by consideration on the circuit design but usually comes from other systems and fabrication cost. Therefore, the number of capacitor cannot be chosen as wanted. Similarly, the minimum switching time is usually limited, and the minimum switching time is externally constrained. In the proposed mutual-capacitance readout sensor, the switching pattern is provided from the operation controller. Each switching sequence is stored at the FSM-based operation controller and requires at least one clock cycle to become next state to turn on the next switch. However, a lower clock frequency on the digital modules is preferred since power dissipation of the digital modules including the operation controller is heavily related to the clock frequency. Alternatively, [3.22] proposed a delay line based switching time control, but generating several hundreds of nano-seconds of delay is not efficiently achieved. The delay line based time control is better suited for the higher frequency generation up to a few nano-seconds.

Therefore, the general energy-efficiency on signal generation should consider both the number of capacitor (the number of intermediate voltage levels) and the minimum switching time. Each point in Fig. 3.11, 3.12, and A.1 exhibits certain structure of the signal generator and switching time, hence the $|f_{STM}|/E_{DRV}$ is also drawn according to the variables. Fig. A.2 shows the energy-efficiency on the signal generation with touch-screen panel bandwidth from 100 kHz to 1,600 kHz.
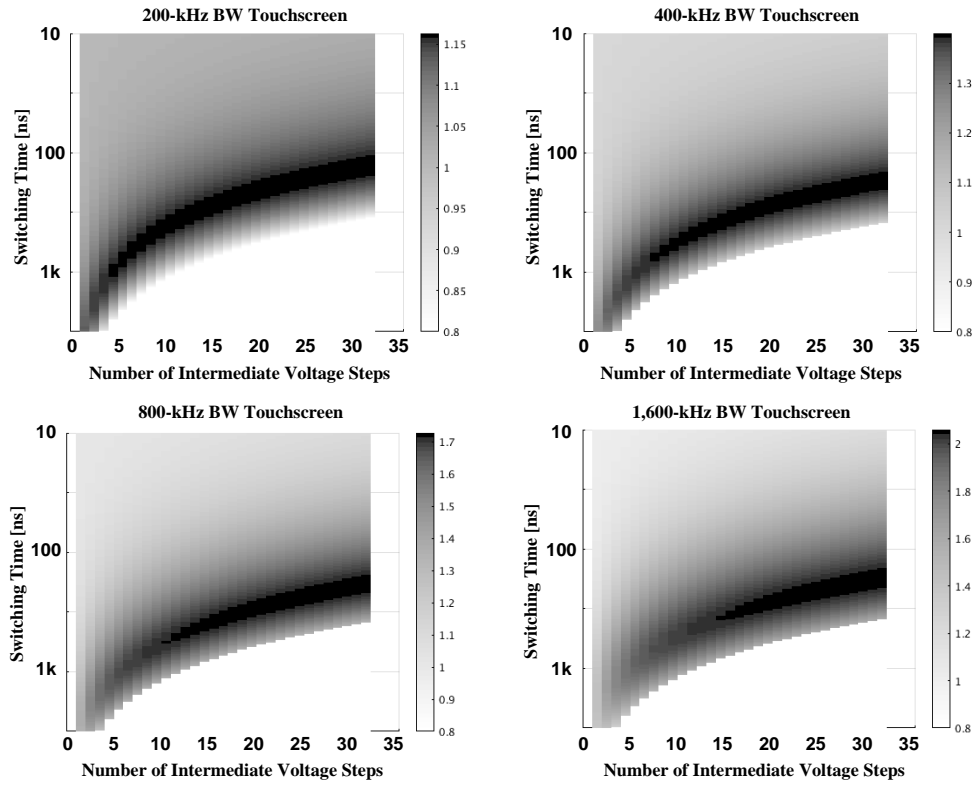
Fig. A.2 Performance of the signal generator with

200, 400, 800, and 1,600-kHz bandwidth TSP.

Appendix B

Column/Row Sum of an Orthogonal Matrix

In Chapter 3, an orthogonal matrix of driving sequence is utilized for the multi-channel driving and demodulation to recover the mutual-capacitance profile. Especially, a Hadamard matrix is utilized which is an $n \times n$ matrix whose entries ($H_{i,j}$) are either 1 or -1 and whose columns and rows are mutually orthogonal that $H \times H^T = nI$. The sum of the square of the column sums is expressed as

$$\sum_{i=1}^{n}\left(\sum_{k=1}^{n}H_{i,k}\right)^2 = \sum_{i=1}^{n}\left((\sum_{k=1}^{n}H_{i,k}^{2})\right) + \sum_{i=1}^{n}\left(2\cdot(\sum_{l\neq m}H_{i,l}\cdot H_{i,m})\right). \quad \text{(B.1)}$$

The first term becomes n^2, and the second term is zero because of the orthogonality. Therefore, if possible, the minimum column sum of a Hadamard matrix is $\sqrt{n}$ with equally distributed column sum. Same applies to (B.1) for row sum of the matrix.

Bibliography

[1.1]   S. Kim et al., "A Highly Sensitive Capacitive Touch Sensor Integrated on a Thin-Film-Encapsulated Active-Matrix OLED for Ultrathin Displays," IEEE Transactions on Electron Devices, vol. 58, no. 10, pp. 3609–3615, Oct. 2011.

[1.2]   Y.-H. Lin, M.-T. Lee, and A. T. Huang, "5-1: Invited Paper: Booming Flexible Applications Enabled by AMOLED Technologies," SID Symposium Digest of Technical Papers, vol. 48, no. 1, pp. 29–32, 2017.

[2.1]   "Windows 10 Guidelines - Touch Requirements," [Online]. Available: https://docs.microsoft.com/en-us/windows-hardware/design/component-guidelines/display. [Accessed: 09-May-2019].

[2.2]   "Touch Devices," *Android Open Source Project*. [Online]. Available: https://source.android.com/devices/input/touch-devices. [Accessed: 09-May-2019].

[2.3]   K. Lim, K. Jung, C. Jang, J. Baek, and I. Kang, "A Fast and Energy Efficient Single-Chip Touch Controller for Tablet Touch Applications," *Journal of Display Technology*, vol. 9, no. 7, pp. 520–526, Jul. 2013.

[2.4]   A. Yamada *et al.*, "A multi-core architecture of digital back-end for large mutual capacitance touch sensing systems," in *2015 IEEE International Symposium on Circuits and Systems (ISCAS)*, 2015, pp. 1382–1385.

[2.5]   F. Chang, C.-J. Chen, and C.-J. Lu, "A linear-time component-labeling algorithm using contour tracing technique," *Computer Vision and Image Understanding*, vol. 93, no. 2, pp.

206–220, Feb. 2004.

[2.6]   C. Lin, Y. Chang, C. Hung, C. Tu, and C. Chuang, "Position Estimation and Smooth Tracking With a Fuzzy-Logic-Based Adaptive Strong Tracking Kalman Filter for Capacitive Touch Panels," *IEEE Transactions on Industrial Electronics*, vol. 62, no. 8, pp. 5097–5108, Aug. 2015.

[2.7]   S. H. Bae and Y. S. Lee, "Highly parallel touch controller with high-speed weighted median noise reduction unit for on-cell type touch screen panel," in *2015 International SoC Design Conference (ISOCC)*, 2015, pp. 259–260.

[2.8]   B. Li, T. Wei, X. Wei, J. Wang, W. Liu, and R. Zheng, "A Touch Prediction and Window Sensing Strategy for Low-Power and Low-Cost Capacitive Multitouch Screen Systems," *Journal of Display Technology*, vol. 12, no. 6, pp. 646–657, Jun. 2016.

[2.9]   J. An, S. Hong, and O. Kwon, "A highly linear and accurate touch data extraction algorithm based on polar coordinates for large-sized capacitive touch screen panels," *IEEE Transactions on Consumer Electronics*, vol. 62, no. 4, pp. 341–348, Nov. 2016.

[2.10]   S. Gao, J. Lai, and A. Nathan, "Fast Readout and Low Power Consumption in Capacitive Touch Screen Panel by Downsampling," *Journal of Display Technology*, vol. 12, no. 11, pp. 1417–1422, Nov. 2016.

[2.11]   J.-E. Park, D. Lim, and D. Jeong, "A Reconfigurable 40-to-67 dB SNR, 50-to-6400 Hz Frame-Rate, Column-Parallel Readout IC for Capacitive Touch-Screen Panels," *IEEE Journal of Solid-State Circuits*, vol. 49, no. 10, pp. 2305–2318, Oct. 2014.

[2.12]   J. Bang *et al.*, "A Hybrid AMOLED Driver IC for Real-Time TFT Nonuniformity Compensation," *IEEE Journal of Solid-State Circuits*, vol. 51, no. 4, pp. 966–978, Apr. 2016.

[2.13]   H. Kim and D. Kim, "An Active-Matrix OLED Driver CMOS IC With Compensation of Non-Uniform Routing-Line Resistances in Ultra-Thin Panel Bezel," *IEEE Journal of Solid-State Circuits*, vol. 53, no. 2, pp. 484–500, Feb. 2018.

[2.14]   S. Ko *et al.*, "Low noise capacitive sensor for multi-touch mobile handset's applications," in *2010 IEEE Asian Solid-State Circuits Conference (A-SSCC)*, 2010, pp. 1–4.

[2.15]   H. Shin, S. Ko, H. Jang, I. Yun, and K. Lee, "A 55dB SNR with 240Hz frame scan rate mutual capacitor 30×24 touch-screen panel read-out IC using code-division multiple sensing technique," in *2013 IEEE International Solid-State Circuits Conference (ISSCC)*, 2013, pp. 388–389.

[2.16]   J. K. Park, C.-J. Lee, D. Kim, J. Chun, and J. T. Kim, "Application of weighing matrices to simultaneous driving technique for capacitive touch sensors," *IEEE Transactions on Consumer Electronics*, vol. 61, no. 2, pp. 261–269, May 2015.

[2.17]   J. K. Park, C.-J. Lee, and J. T. Kim, "Analysis of Multi-Level Simultaneous Driving Technique for Capacitive Touch Sensors," *Sensors (Basel)*, vol. 17, no. 9, Sep. 2017.

[3.1]   M. Miyamoto, M. Hamaguchi, and A. Nagao, "A 143x81 Mutual-Capacitance Touch-Sensing Analog Front-End With Parallel Drive and Differential Sensing Architecture," *IEEE Journal of Solid-State Circuits*, vol. 50, no. 1, pp. 335–343, Jan. 2015.

[3.2]   J.-H. Yang *et al.*, "A highly noise-immune touch controller using Filtered-Delta-Integration and a charge-interpolation technique for 10.1-inch capacitive touch-screen panels," in

2013 IEEE International Solid-State Circuits Conference (ISSCC), 2013, pp. 390–391.

[3.3]   J. A. Fredenburg and M. P. Flynn, "A 90-MS/s 11-MHz-Bandwidth 62-dB SNDR Noise-Shaping SAR ADC," *IEEE Journal of Solid-State Circuits*, vol. 47, no. 12, pp. 2898–2904, Dec. 2012.

[3.4]   Z. Chen, M. Miyahara, and A. Matsuzawa, "A 2ndorder fully-passive noise-shaping SAR ADC with embedded passive gain," in *2016 IEEE Asian Solid-State Circuits Conference (A-SSCC)*, 2016, pp. 309–312.

[3.5]   Y. Shu, L. Kuo, and T. Lo, "An Oversampling SAR ADC With DAC Mismatch Error Shaping Achieving 105 dB SFDR and 101 dB SNDR Over 1 kHz BW in 55 nm CMOS," *IEEE Journal of Solid-State Circuits*, vol. 51, no. 12, pp. 2928–2940, Dec. 2016.

[3.6]   C. Liu and M. Huang, "28.1 A 0.46mW 5MHz-BW 79.7dB-SNDR noise-shaping SAR ADC with dynamic-amplifier-based FIR-IIR filter," in *2017 IEEE International Solid-State Circuits Conference (ISSCC)*, 2017, pp. 466–467.

[3.7]   W. Guo, H. Zhuang, and N. Sun, "A 13b-ENOB 173dB-FoM 2nd-order NS SAR ADC with passive integrators," in *2017 Symposium on VLSI Circuits*, 2017, pp. C236–C237.

[3.8]   A. J. Drake, K. J. Nowka, T. Y. Nguyen, J. L. Burns, and R. B. Brown, "Resonant clocking using distributed parasitic capacitance," in *Proceedings of the IEEE 2003 Custom Integrated Circuits Conference, 2003.*, 2003, pp. 647–650.

[3.9]   I. Bezzam, C. Mathiazhagan, T. Raja, and S. Krishnan, "An Energy-Recovering Reconfigurable Series Resonant Clocking Scheme for Wide Frequency Operation," *IEEE Transactions on Circuits and Systems I: Regular Papers*, vol. 62, no. 7, pp. 1766–1775, Jul. 2015.

[3.10]   M. Lee and J. Kim, "Design of a 93% Energy-Efficient Buck-Type Capacitor Charger IC in 250-nm CMOS," *IEEE Transactions on Industry Applications*, vol. 52, no. 4, pp. 3203–3211, Jul. 2016.

[3.11]   F. U. Rahman and V. Sathe, "Quasi-Resonant Clocking: Continuous Voltage-Frequency Scalable Resonant Clocking System for Dynamic Voltage-Frequency Scaling Systems," *IEEE Journal of Solid-State Circuits*, vol. 53, no. 3, pp. 924–935, Mar. 2018.

[3.12]   J. G. Koller and W. C. Athas, "Adiabatic Switching, Low Energy Computing, And The Physics Of Storing And Erasing Information," in *Workshop on Physics and Computation*, Dallas, TX, 1992, pp. 267–270.

[3.13]   L. J. Svensson and J. G. Koller, "Driving a capacitive load without dissipating fCV^2," in *Proceedings of 1994 IEEE Symposium on Low Power Electronics*, 1994, pp. 100–101.

[3.14]   W. C. Athas, L. J. Svensson, J. G. Koller, N. Tzartzanis, and E. Y.-C. Chou, "Low-power digital systems based on adiabatic-switching principles," *IEEE Transactions on Very Large Scale Integration (VLSI) Systems*, vol. 2, no. 4, pp. 398–407, Dec. 1994.

[3.15]   S. Nakata, S. Mutoh, H. Makino, M. Miyama, and Y. Matsuda, "Stable adiabatic circuit using advanced series capacitors and time variation of energy dissipation," *IEICE Electron. Express*, vol. 7, no. 9, pp. 640–646, 2010.

[3.16]   C. L. Seitz *et al.*, "Hot Clock nMOS," 1985. [Online]. Available: http://resolver.caltech.edu/CaltechCSTR:1985.5177-tr-85. [Accessed: 09-May-2019].

[3.17]   A. G. Dickinson and J. S. Denker, "Adiabatic dynamic logic," *IEEE Journal of Solid-State Circuits*, vol. 30, no. 3, pp. 311–315, Mar. 1995.

[3.18]   J.-S. Kim, D.-K. Jeong, and G. Kim, "A multi-level multi-phase charge-recycling method for low-power AMLCD column drivers," *IEEE Journal of Solid-State Circuits*, vol. 35, no. 1, pp. 74–84, Jan. 2000.

[3.19]   M. Arsalan and M. Shams, "Charge-recovery power clock generators for adiabatic logic circuits," in *18th International Conference on VLSI Design held jointly with 4th International Conference on Embedded Systems Design*, 2005, pp. 171–174.

[3.20]   M. van Elzakker, E. van Tuijl, P. Geraedts, D. Schinkel, E. A. M. Klumperink, and B. Nauta, "A 10-bit Charge-Redistribution ADC Consuming 1.9μW at 1 MS/s," *IEEE Journal of Solid-State Circuits*, vol. 45, no. 5, pp. 1007–1015, May 2010.

[3.21]   W. Biederman *et al.*, "A 4.78 mm 2 Fully-Integrated Neuromodulation SoC Combining 64 Acquisition Channels With Digital Compression and Simultaneous Dual Stimulation," *IEEE Journal of Solid-State Circuits*, vol. 50, no. 4, pp. 1038–1047, Apr. 2015.

[3.22]   L. G. Salem and P. P. Mercier, "26.4 A 0.4-to-1V 1MHz-to-2GHz switched-capacitor adiabatic clock driver achieving 55.6% clock power reduction," in *2017 IEEE International Solid-State Circuits Conference (ISSCC)*, 2017, pp. 442–443.

[3.23]   A. Khorami and M. Sharifkhani, "An Efficient Fast Switching Procedure for Stepwise Capacitor Chargers," *IEEE Transactions on Very Large Scale Integration (VLSI) Systems*, vol. 25, no. 2, pp. 705–713, Feb. 2017.

[3.24]   W. F. Trench, "Properties of some generalizations of Kac-Murdock-Szegő matrices," in *Contemporary Mathematics*, vol. 281, V. Olshevsky, Ed. Providence, Rhode Island: American Mathematical Society, 2001, pp. 233–245.

[3.25]   O. Oliaei, "Noise analysis of correlated double sampling SC-integrators," in *2002 IEEE International Symposium on Circuits and Systems. Proceedings*, 2002, vol. 4, pp. 445–448.

[3.26]   M. Dow, "Explicit inverses of Toeplitz and associated matrices," *ANZIAM Journal*, vol. 44, no. 0, pp. 185–215, Jan. 2008.

[3.27]   M. D. Seeman and S. R. Sanders, "Analysis and Optimization of Switched-Capacitor DC–DC Converters," *IEEE Transactions on Power Electronics*, vol. 23, no. 2, pp. 841–851, Mar. 2008.

[3.28]   H. Le, S. R. Sanders, and E. Alon, "Design Techniques for Fully Integrated Switched-Capacitor DC-DC Converters," *IEEE Journal of Solid-State Circuits*, vol. 46, no. 9, pp. 2120–2131, Sep. 2011.

[3.29]   S. R. Sanders, E. Alon, H. Le, M. D. Seeman, M. John, and V. W. Ng, "The Road to Fully Integrated DC–DC Conversion via the Switched-Capacitor Approach," *IEEE Transactions on Power Electronics*, vol. 28, no. 9, pp. 4146–4155, Sep. 2013.

[3.30]   G. Fikioris, "Spectral properties of Kac–Murdock–Szegö matrices with a complex parameter," *Linear Algebra and its Applications*, vol. 553, pp. 182–210, Sep. 2018.

[3.31]   Donadio, M. P., "CIC Filter Introduction", available at www.dspguru.com/info/tutor, Jul. 2000.

[3.32]   C. C. Enz and G. C. Temes, "Circuit techniques for reducing the effects of op-amp imperfections: autozeroing, correlated double sampling, and chopper stabilization," *Proceedings of the IEEE*, vol. 84, no. 11, pp. 1584–1614, Nov. 1996.

[3.33] T. Hwang, W. Cui, I. Yang, and O. Kwon, "A highly area-efficient controller for capacitive touch screen panel systems," *IEEE Transactions on Consumer Electronics*, vol. 56, no. 2, pp. 1115–1122, May 2010.

[3.34] I. Yang and O. Kwon, "A touch controller using differential sensing method for on-cell capacitive touch screen panel systems," *IEEE Transactions on Consumer Electronics*, vol. 57, no. 3, pp. 1027–1032, Aug. 2011.

[3.35] M. Ozbas, I. Knausz, J. Lillie, C. Ludden, T. Mackin, and D. Gillespie, "An In-cell Capable Capacitive Touchscreen Controller With High SNR and Integrated Display Driver IC for WVGA LTPS Displays," *SID Symposium Digest of Technical Papers*, vol. 43, no. 1, pp. 485–488, 2012.

[3.36] K.-D. Kim *et al.*, "A capacitive touch controller robust to display noise for ultrathin touch screen displays," in *2012 IEEE International Solid-State Circuits Conference (ISSCC)*, 2012, pp. 116–117.

[3.37] S. Zhan, T. Wei, B. Li, W. Liu, and Q. Chen, "A Touch Sensor Controller IC Adopting Differential Measurement for Projected Capacitive Touch Panel Systems," in *2012 IEEE 12th International Conference on Computer and Information Technology*, 2012, pp. 477–481.

[3.38] K.-D. Kim *et al.*, "A Capacitive Touchscreen Controller IC with Noise-based Hybrid Sensing Scheme," *SID Symposium Digest of Technical Papers*, vol. 44, no. 1, pp. 626–629, 2013.

[3.39] H. Shin, S. Ko, H. Jang, I. Yun, and K. Lee, "A 55dB SNR with 240Hz frame scan rate mutual capacitor 30×24 touch-screen panel read-out IC using code-division multiple sensing technique," in *2013 IEEE International Solid-State Circuits Conference (ISSCC)*, 2013, pp.

388–389.

[3.40]   S. Ko, H. Shin, H. Jang, I. Yun, and K. Lee, "A 70dB SNR capacitive touch screen panel readout IC using capacitor-less trans-impedance amplifier and coded Orthogonal Frequency-Division Multiple Sensing scheme," in *2013 Symposium on VLSI Circuits*, 2013, pp. C216–C217.

[3.41]   J.-E. Park, D. Lim, and D. Jeong, "A 6.3 mW high-SNR frame-rate scalable touch screen panel readout IC with column-parallel Σ-Δ ADC structure for mobile devices," in *2013 IEEE Asian Solid-State Circuits Conference (A-SSCC)*, 2013, pp. 357–360.

[3.42]   H. Jang, H. Shin, S. Ko, I. Yun, and K. Lee, "12.5 2D Coded-aperture-based ultra-compact capacitive touch-screen controller with 40 reconfigurable channels," in *2014 IEEE International Solid-State Circuits Conference (ISSCC)*, 2014, pp. 218–219.

[3.43]   Y. Jang, Y. Ko, J. Choi, H. Oh, and S. Lee, "A 45-dB, 150-Hz, and 18-mW Touch Controller for On-Cell Capacitive TSP Systems," *IEEE Transactions on Circuits and Systems II: Express Briefs*, vol. 61, no. 10, pp. 748–752, Oct. 2014.

[3.44]   N. Miura *et al.*, "A 1 mm Pitch 80 x 80Channel 322 Hz Frame-Rate Multitouch Distribution Sensor With Two-Step Dual-Mode Capacitance Scan," *IEEE Journal of Solid-State Circuits*, vol. 50, no. 11, pp. 2741–2749, Nov. 2015.

[3.45]   C. Park *et al.*, "A Pen-Pressure-Sensitive Capacitive Touch System Using Electrically Coupled Resonance Pen," *IEEE Journal of Solid-State Circuits*, vol. 51, no. 1, pp. 168–176, Jan. 2016.

[3.46]   H. Kim and K. Han, "High-SNR Capacitive Multi-Touch Sensing Technique for

AMOLED Display Panels," *IEEE Sensors Journal*, vol. 16, no. 4, pp. 859–860, Feb. 2016.

[3.47]   S. Heo *et al.*, "72 dB SNR, 240 Hz Frame Rate Readout IC With Differential Continuous-Mode Parallel Architecture for Larger Touch-Screen Panel Applications," *IEEE Transactions on Circuits and Systems I: Regular Papers*, vol. 63, no. 7, pp. 960–971, Jul. 2016.

[3.48]   J. An, S. Jung, S. Hong, and O. Kwon, "A Highly Noise-Immune Capacitive Touch Sensing System Using an Adaptive Chopper Stabilization Method," *IEEE Sensors Journal*, vol. 17, no. 3, pp. 803–811, Feb. 2017.

[3.49]   S. Park, H. Kim, J. Bang, G. Cho, and G. Cho, "A 0.26-nJ/node, 400-kHz Tx Driving, Filtered Fully Differential Readout IC With Parasitic RC Time Delay Reduction Technique for 65-in 169×97 Capacitive-Type Touch Screen Panel," *IEEE Journal of Solid-State Circuits*, vol. 52, no. 2, pp. 528–542, Feb. 2017.

[3.50]   J. An *et al.*, "A 3.9-kHz Frame Rate and 61.0-dB SNR Analog Front-End IC With 6-bit Pressure and Tilt Angle Expressions of Active Stylus Using Multiple-Frequency Driving Method for Capacitive Touch Screen Panels," *IEEE Journal of Solid-State Circuits*, vol. 53, no. 1, pp. 187–203, Jan. 2018.

[3.51]   H. Hwang, H. Lee, M. Han, H. Kim, and Y. Chae, "A 1.8-V 6.9-mW 120-fps 50-Channel Capacitive Touch Readout With Current Conveyor AFE and Current-Driven $\sum \Delta$ ADC," *IEEE Journal of Solid-State Circuits*, vol. 53, no. 1, pp. 204–218, Jan. 2018.

[3.52]   J. Park, Y. Hwang, J. Oh, J.-E. Park, and D. Jeong, "Adiabatically driven touch controller analog front-end for ultra-thin displays," in *2018 IEEE Custom Integrated Circuits Conference (CICC)*, 2018, pp. 1–4.

[3.53]   E. Choi, S. Kim, K. Park, F. Bien, and H. Kim, "Improved SNR, On-Chip Differentially Modulated TISM Signaling in HV DMOS Process for Mutual Capacitance Fingerprint Sensor," in *2018 IEEE International Symposium on Circuits and Systems (ISCAS)*, 2018, pp. 1–4.

[3.54]   S. Kim *et al.*, "A 39.5-dB SNR, 300-Hz Frame-Rate, 56×70-Channel Read-Out IC for Electromagnetic Resonance Touch Panels," *IEEE Transactions on Industrial Electronics*, vol. 65, no. 6, pp. 5001–5011, Jun. 2018.

[3.55]   O. Kwon, J. An, and S. Hong, "Capacitive Touch Systems With Styli for Touch Sensors: A Review," *IEEE Sensors Journal*, vol. 18, no. 12, pp. 4832–4846, Jun. 2018.

[3.56]   S. Jeon, J. Lee, H. Hwang, W. Ryu, and Y. Chae, "A Parasitic Insensitive Catheter-Based Capacitive Force Sensor for Cardiovascular Diagnosis," *IEEE Transactions on Biomedical Circuits and Systems*, vol. 12, no. 4, pp. 812–823, Aug. 2018.

[3.57]   Y. Li, S. Wang, H. Sheng, C. P. Chng, and S. Lakshmikanthan, "Investigating CM Voltage and Its Measurement for AC/DC Power Adapters to Meet Touchscreen Immunity Requirement," *IEEE Transactions on Electromagnetic Compatibility*, vol. 60, no. 4, pp. 1102–1110, Aug. 2018.

[3.58]   H. Xing *et al.*, "High Sensitive Readout Circuit for Capacitance Touch Panel With Large Size," *IEEE Sensors Journal*, vol. 19, no. 4, pp. 1412–1415, Feb. 2019.

[3.59]   J.-E. Park, J. Park, Y.-H. Hwang, J. Oh, and D.-K. Jeong, "A Noise-Immunity-Enhanced Analog Front-End for 36×64 Touch-Screen Controllers With 20-V_{PP} Noise Tolerance at 100 kHz," *IEEE Journal of Solid-State Circuits*, vol. 54, no. 5, pp. 1497–1510, May 2019.

[3.60]   J. Park, Y. Hwang, J. Oh, Y. Song, J.-E. Park, and D. Jeong, "A Mutual Capacitance

Touch Readout IC With 64% Reduced-Power Adiabatic Driving Over Heavily Coupled Touch Screen," *IEEE Journal of Solid-State Circuits,* vol 54, no. 6, pp 1694–1704, Jun. 2019.

[4.1]   K. Lasanen and J. Kostamovaara, "A 1.2-V CMOS RC Oscillator for Capacitive and Resistive Sensor Applications," *IEEE Transactions on Instrumentation and Measurement*, vol. 57, no. 12, pp. 2792–2800, Dec. 2008.

[4.2]   S. Oh *et al.*, "A Dual-Slope Capacitance-to-Digital Converter Integrated in an Implantable Pressure-Sensing System," *IEEE Journal of Solid-State Circuits*, vol. 50, no. 7, pp. 1581–1591, Jul. 2015.

[4.3]   Y. Hu *et al.*, "12.2 3D gesture-sensing system for interactive displays based on extended-range capacitive sensing," in *2014 IEEE International Solid-State Circuits Conference (ISSCC)*, 2014, pp. 212–213.

[4.4]   L. Du *et al.*, "6.7 A 2.3mW 11cm-range bootstrapped and correlated-double-sampling (BCDS) 3D touch sensor for mobile devices," in *2015 IEEE International Solid-State Circuits Conference (ISSCC)*, 2015, pp. 122–123.

[4.5]   Y.-S. Jang, K.-U. Gwak, S.-S. Lee, S.-G. Lee, J.-H. Kim, and H.-S. Oh, "P-181: A Charge-Share-Based Relative Read-Out Circuit for Capacitance Sensing," *SID Symposium Digest of Technical Papers*, vol. 41, no. 1, pp. 1937–1939, 2010.

[4.6]   H. Ha, D. Sylvester, D. Blaauw, and J. Sim, "12.6 A 160nW 63.9fJ/conversion-step capacitance-to-digital converter for ultra-low-power wireless sensor nodes," in *2014 IEEE International Solid-State Circuits Conference (ISSCC)*, 2014, pp. 220–221.

[4.7]   K.-D. Kim *et al.*, "A fully-differential capacitive touch controller with input common-

mode feedback for symmetric display noise cancellation," in *2014 Symposium on VLSI Circuits Digest of Technical Papers*, 2014, pp. 1–2.

[4.8]   Y. Huh *et al.*, "A 10.1" 56-channel, 183 uW/electrode, 0.73 mm2/sensor high SNR 3D hover sensor based on enhanced signal refining and fine error calibrating techniques," in *2017 Symposium on VLSI Circuits*, 2017, pp. 308–309.

[4.9]   J.-W. Lee, D.-J. Min, J. Kim, and W. Kim, "A 600-dpi capacitive fingerprint sensor chip and image-synthesis technique," *IEEE Journal of Solid-State Circuits*, vol. 34, no. 4, pp. 469–475, Apr. 1999.

[4.10]   S.-M. Jung, J.-M. Nam, D.-H. Yang, and M.-K. Lee, "A CMOS integrated capacitive fingerprint sensor with 32-bit RISC microcontroller," *IEEE Journal of Solid-State Circuits*, vol. 40, no. 8, pp. 1745–1750, Aug. 2005.

[4.11]   Y. Yu and T. Sun, "A Pseudo-Differential Measuring Approach for Implementing Microcontroller-Based Capacitive Touch Sensing in Low-Power Quality Situation," *IEEE Sensors Journal*, vol. 16, no. 2, pp. 390–399, Jan. 2016.

[4.12]   J. Park, Y. Hwang, J. Oh, Y. Song, J.-E. Park, and D. Jeong, "A Compact Self-Capacitance Sensing Analog Front-End for a Touch Detection in Low Power Mode," to be published in *Proceedings of 2019 IEEE Symposium on Low Power Electronics and Design (ISLPED),* 2019.